Department of Precision and Microsystems Engineering

A miniature chemical actuator with a compliant expansion chamber, passive exhaust valve and electrowetting-based fuel injection

Guido Mous

Report no : 2020.050
Supervisor : Hans Goosen
Specialisation : Engineering mechanics
Type of report : Thesis
Date : November 2nd, 2020

CONTENTS

1

INTRODUCTION

1.1. BACKGROUND

In recent years, an increasing amount of research projects contributed to the development of small unmanned air vehicle (UAV) that can fly and perform hovering flight in confined spaces. This development is driven by numerous applications such as hazardous environment exploration, search and rescue, assisted agriculture and other monitoring tasks that are outside the range of conventional surveillance cameras [17][23]. As miniaturization of electronic components as microcontrollers, sensors and wireless communication units is made possible by innovations in the portable electronic industry, UAV are manufactured in even smaller sizes to decrease costs [23]. As size is reduced from macro-scale (>10 cm) towards meso-scale (1 mm to 10 cm) [10], researchers have become increasingly interested in flapping wing micro air vehicle (FWMAV) [22]. Flapping wing devices involve wings with multiple degrees of freedom, speed-varying flapping motion as well as the possibility to perform wing shape morphing. This leads to an increase in maneuverability that is impossible to achieve with fixed wing or rotary wing vehicles [25], which is especially important in confined-space applications. Moreover, at these scales, FWMAV can exploit "unsteady flow" effects to increase lift and aerodynamic efficiency, while these effects are problematic for fixed wing and rotary wing devices [20]. The interest for FWMAV is not only related to aforementioned direct applications. They could also be used as tools to develop control strategies for computation and sensor limited systems, study fluid-structure interactions and tackle other technological challenges that FWMAV projects entail [17]. However, due to the nature of scaling, FWMAVs suffer from very limited endurance which can be explained by the following reasons.

Firstly, the physics of scaling affects the aerodynamic performance. UAVs that have a smaller characteristic length typically induce flow of a lower Reynolds number. This implies more dominance of viscous forces and therefore lower lift-to-drag ratio. Although flapping wings of FWMAV exploit these viscous effects and slightly compensate for the loss of lift [20][17], an increased wing velocity is needed to maintain flight and more energy is lost to drag [22].
Secondly, actuator or engine performance does not scale down beneficially when the size of FWMAV is approached. Due to scaling laws, area dependent forces like sliding friction become more dominant [23]. Since a vast majority of all FWMAV use the combination of a rotary electric motor and relatively complex transmission mechanisms, the efficiency is often compromised due to the friction heat being produced in gearing and linkages [53]. Moreover, small-scale fabrication techniques have a negative influence on electric motor performance [41]. Next to electric actuators, chemical actuators also suffer the laws of scale. Loss mechanisms as heat loss, aerodynamic loss and quenching scale with area, whereas energy produced per combustion cycle scales with volume. Due to the increased area-to-volume ratio at small scales, these loss mechanisms will become dominant over energy generation. Moreover, leakage between piston and cylinder wall is found to become increasingly dominant at small-scales [2][59][1]. Aforementioned effects lead to the fact that specific power as well as actuator efficiency decreases significantly as actuators size is reduced to meso-scale.

The combination of the reduced aerodynamic efficiency and reduced actuator performance results in increased consumption of energy, increased actuator mass and increased energy storage mass, relative to the total mass of the vehicle. This increases the power required to sustain hovering flight even more, creating an exponential effect that has a very detrimental effect on system mass and thereby flight endurance. Clear evidence can be found for this in literature. A negative exponential relationship between aerial vehicle mass and flight time is observed [23], as is depicted in Figure 1.1. Analysing the design space of FWMAV in terms of flight time and mass, it becomes apparent that a gap in the state-of-the-art exists where vehicles should fly in excess of 10 minutes while having a mass lower than 10 grams, highlighted in blue in Figure 1.1.

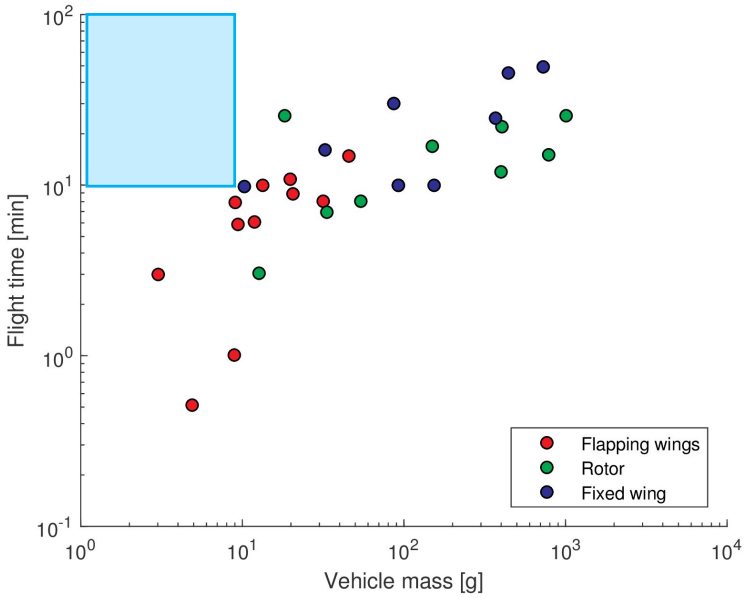

Figure 1.1: Flight time as a function of vehicle mass for several small scale UAV's, grouped per wing category [23]. State-of-the-art gap depicted with blue rectangle.

To benefit from aforementioned advantages and applications of FWMAV in this size range, it is chosen to focus on this design space. This study chooses to focus on actuator development, since significant improvements can be made in mass-reduction and actuator efficiency, which are highly decisive in the flight time of FWMAV [67].

1.2. AIM OF THE RESEARCH

The present study aims is to develop a low-mass actuator design for application FWMAV with high efficiency and high specific power such that a flight endurance in excess of 10 minutes is supported. Also, it aims to develop an experimental setup to provide a proof-of-concept as well as to experimentally characterize the performance. Lastly, it aims to construct and validate mathematical models to predict the performance of the actuator of current and future designs.

1.3. THESIS OUTLINE

The outline of this thesis is visualised in Figure 1.2, which is organised as follows: Firstly, in Chapter 2 the design process is described which includes the actuator requirements, state-of-the-art analysis, concept generation and selection, as well as a design proposal.
Secondly, in Chapter 3 an actuator model is developed to predict the actuator performance of a compliant expansion chamber and passive exhaust valve. Also, this chapter describes how the expansion chamber and passive exhaust valve are experimentally validated in a measurement setup.
Additionally, Chapter 4 highlights the design of an electrowetting-based fuel injection device, where a mathematical model is developed that predicts fuel transport. Also, it is tried to validate predicted fuel transport dynamics in an experimental setup.
In Chapter 5, an investigation is performed to identify if a practical design can achieve the research goal of 10 minutes of flight endurance.
Lastly, in Chapter 6, a conclusion and recommendations are given.

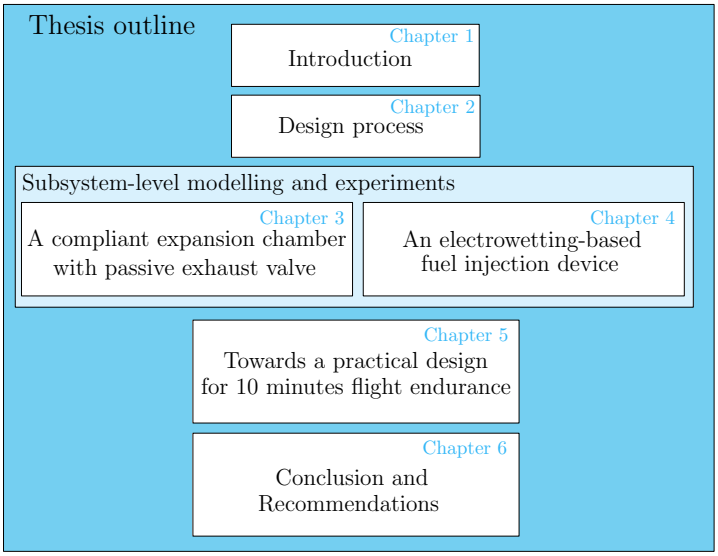

Figure 1.2: Thesis outline

2

DESIGN PROCESS

2.1. INTRODUCTION

To achieve the research goal, it is of importance to perform a design process where the whole design spectrum is reviewed in a thorough and systematic manner. To do so, this chapter outlines the design process of the actuator development. The independent steps that are undertaken in this design process and the organisation of the sections is given in Figure 2.1. First, actuator requirements are defined that the actuator has to comply with in order to achieve the research goal. Resulting from set actuator requirements, a convergence step is made by explaining why electrical energy carriers are eliminated from the design space. Subsequently, a system breakdown and functional analysis of the different subsystems are given for chemical actuators specifically. Additionally, state-of-the-art developments are discussed for each of the relevant subsystems. Then, partly based on state-of-the-art and partly based on own design, concepts are generated for each of the actuator subsystems. After a concept comparison and selection, a design is proposed and its functioning principle is given.

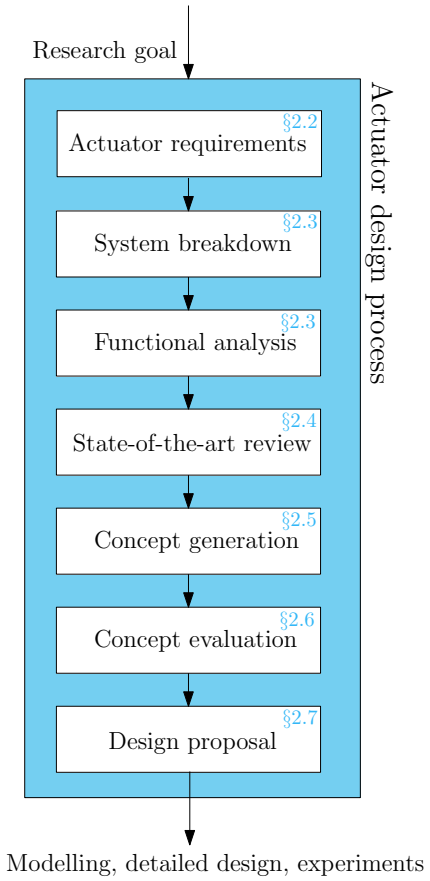

Figure 2.1: Visual representation of conceptual design process

2.2. ACTUATOR REQUIREMENTS AND RELATED CHOICES

As earlier stated in the introduction, the goal of this research is to develop an actuator for FWMAV depicted in the blue area of Figure 1.1. Assuming half of the total vehicle could be attributed to the actuator, the first requirement is defined by Equation 2.1.

If a flight endurance of 10 minutes should be achieved, power-to-weight and efficiency requirements on the actuator can be imposed. Appendix A.1 depicts a derivation for the minimum specific power of the actuator needed as a function of flight time, efficiency, body mass fraction and fuel type. Figure 2.2 shows the minimum specific power as a function of efficiency for 10 minutes of flight time for different fuel types. For chemical energy sources, it assumes that fuel is being consumed and therefore the required power reduces as vehicle mass reduces, which has a positive influence on the flight endurance. The power-to-weight and efficiency of state-of-the-art actuators, discussed later in this chapter, are also depicted in Figure 2.2 to visualise how well they perform against this power requirement.

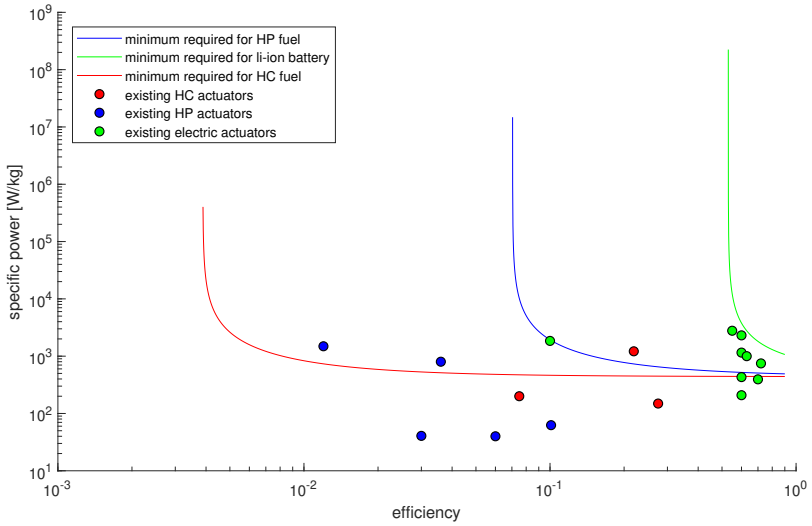

Figure 2.2: Actuator requirements to maintain 10 minutes of flight: specific power against efficiency for electric energy sources, hydrocarbon energy sources and hydrogen peroxide energy sources. Current state-of-the-art actuators specifications are denoted with circles.

The power-to-weight requirement, visualised in Figure 2.2 is also imposed on the actuator system of the current study, to give a bottom limit for the power-to-weight and efficiency of the actuator (Eq. 2.2). Here α describes an aerodynamic constant, Δt the flight time, η the actuator efficiency, e_f the specific energy of the energy carrier and $\frac{m_b}{m_i}$ the body mass fraction. The motivation for the choice of aerodynamic efficiency and body mass fraction is given in Appendix A.1. It is important to mention that aerodynamic efficiency is strongly dependent on flapping frequency. Literature suggests that an optimal flapping frequency is approximately 30 Hz for this size range, depending on the shape of the wing [68]. Therefore, the third requirement for the actuator system is defined as in Equation 2.3 to create an actuator that drives its wings in an aerodynamically optimal frequency.

$$m_{actuator} < 5\,\mathrm{g} \tag{2.1}$$

$$\frac{P_{avg}}{m_{actuator}} = \frac{\alpha}{e^{-\frac{\alpha \Delta t}{\eta e_f}} - \frac{m_b}{m_i}} \tag{2.2}$$

$$f = 30\,\mathrm{Hz} \tag{2.3}$$

2.2.1. ENERGY SOURCE SELECTION

Investigating Figure 2.2 more closely, it can be observed that using an electrical energy source imposes such stringent mass and efficiency requirements, that no state-of-the-art electric actuators are suitable for flight endurance in excess of 10 minutes in this size range. To give an additional insight into why state-of-the-art batteries are not suitable for long-endurance UAV, another flight time analysis is conducted. Now the energy-to-weight ratio as well as the power-to-weight ratio of the state-of-the-art batteries are inspected. When the vehicle is energy-limited, the battery size should be chosen to comply with the amount of energy required by its total flight cycle. On the other hand, the energy storage could also be power limited (dictated by the maximum current that can be drawn from the battery), which is the case for various electric PAVs and MAVs [79]. If the system is power limited, the specific power of the energy carrier is the parameter that becomes decisive for battery selection as well as decisive in the battery weight. Figure 2.3 depicts the flight time as a function of specific energy and specific power of the battery with contour lines. The calculation for this analysis can be found in Appendix A.2. It also highlights different battery data, to visualize how the different state-of-the-art batteries would perform in terms of flight time. The red line indicates the separation between the region where batteries with associated specific power will be power limited and the region where this battery would be energy limited. If the specific power of the energy source is below a certain value, it will not even be possible to perform lift-off. This limit line is located just below the power-limit line, resulting in the fact that most battery types do not deliver enough power to perform lift-off in the first place.

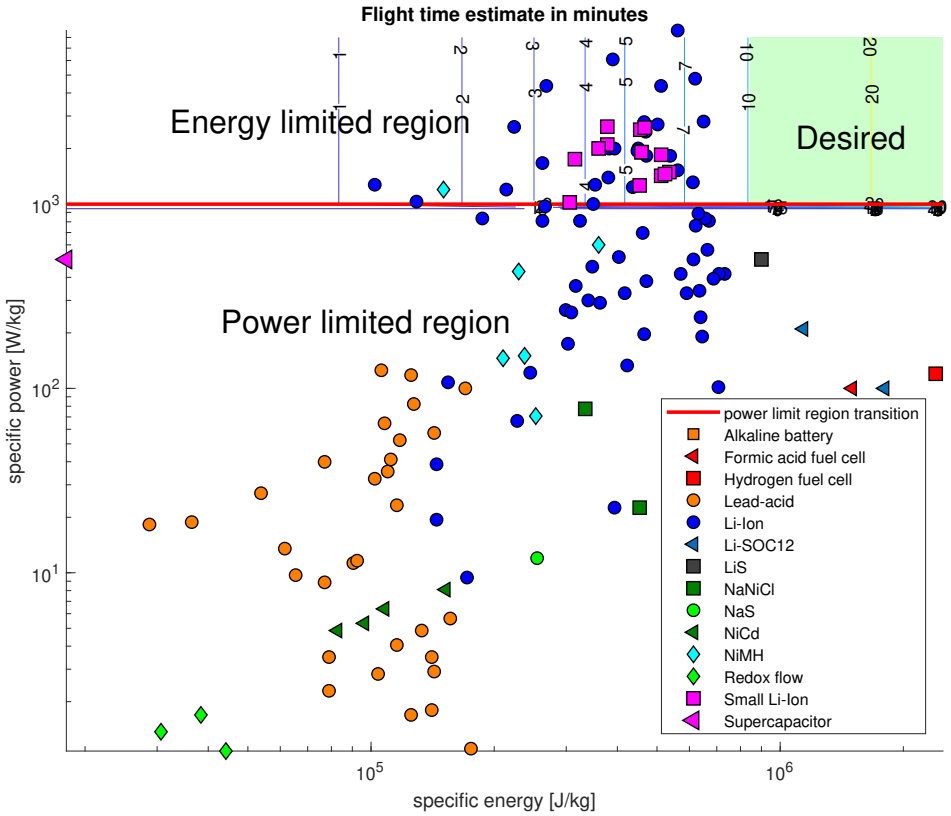

Figure 2.3: Specific energy against the specific power of several electrochemical energy carriers. The contour lines indicate an estimate for the flight endurance given the actuator and body specifications of the nano Hummingbird [37].

It can be observed that no state-of-the art batteries lie in the green area, which is required to achieve the design goal of 10 minutes hovering flight. Chemical energy carriers are usually not power limited, since the fuel supply or injection system is easily scalable. Moreover, their specific energy is superior (more than ten-fold increase). Therefore, it is chosen to focus on chemical actuators only, and eliminate the electrical energy systems from the possible design space.

2.3. SYSTEM BREAKDOWN AND FUNCTIONAL ANALYSIS

Now the energy carrier is known, the system breakdown can be performed with more focus towards chemical actuators. The objective of the system breakdown is to divide the full actuator system into several subsystems. Suitable working principles or concepts can be generated separately for every subsystem, reducing the overall complexity of the problem. Table 2.1 lists the different subsystems in the first column. Additionally, a functional analysis is conducted to define which functions the specific subsystem has to fulfill.

Subsystem	Function
Transmission	Convert output motion of actuator to reciprocating angular motion of flapping wings
Expansion chamber	Transfer force of expanding gas into a moving output component
Fuel storage	Store fuel
Fuel delivery	Transfer fuel from fuel storage to expansion chamber
Fuel exhaust	Transfer combustion products from expansion chamber to environment
Ignition mechanism	Initiate conversion of fuel into pressurized gas in expansion chamber
Control system	Control startup, timing and shutdown of active components in system

Table 2.1: System breakdown and functional analysis of the actuator subsystems

Although the subsystems transmission, fuel storage and control system have an essential role in the functioning of the actuator, the necessity for improvement is regarded to be less than the subsystems expansion chamber, fuel delivery, fuel exhaust and ignition system. Also, they can be designed relatively independently. Therefore, they are regarded outside the scope of this research and not treated further.

2.4. STATE-OF-THE-ART CONCEPTS

For each of the subsystems inside the scope of the research, an overview of the current developments and state-of-the-art is given.

2.4.1. EXPANSION CHAMBER

PISTON-CYLINDER EXPANSION CHAMBER

Until nowadays piston engines, a version of the internal combustion engine, are the most commonly used engine type in all motorised vehicles. The working principle behind piston engines is the occurrence of a periodically changing working chamber as a result of the piston that slides back and forth through a cylinder. Miniaturisation is possible, significant developments are made in several research projects [1, 2, 65]. A traditional crankshaft mechanism is often omitted in a miniaturized design. These free-piston engines are mechanically more simple and lightweight but have a lower thermal efficiency [11, 48]. An example of a small piston-cylinder using hydrocarbon fuels is depicted in Figure 2.4 [2]. Another significant mass-reduction step is done by developing a piston-cylinder type chemical actuator using a catalyst reaction, performed by van den Heuvel [65], depicted in Figure 2.5.

Due to the high surface-to-volume ratio at small scale engines, friction between the sealing rings and cylinder walls becomes very dominant [59]. This is why practically no sealing rings are installed in miniature engines [59][2]. As a consequence, a clearance gap exists between the piston and cylinder walls which makes it possible for charge to leak out of the cylinder what becomes very detrimental for actuator efficiency [1, 2, 59, 65].

SWING ENGINE AS EXPANSION CHAMBER

Over the last 20 years, significant progress is made in the development of swing engines, which are rotationally oscillating free-piston engines, depicted in Figure 2.6. The swing engine comprises four combustion chambers separated by a rotating swing arm, that divides the volume of the base cavity over the four chambers [18]. It promises to have more efficient use of chamber space and engine volume than linear free-piston engines, leading to higher specific power [60].

COMPLIANT EXPANSION CHAMBER

To address the problem of leakage between cylinder and piston, the compliant cylinder concept has been proposed [10, 54–56]. In this free-piston engine, the traditional piston-cylinder combination is replaced by a compliant cavity with the piston attached at one end of the cavity [11]. Leakage losses are fully eliminated with this concept and friction losses are significantly reduced to under 5% [55]. Burugupally et al. developed

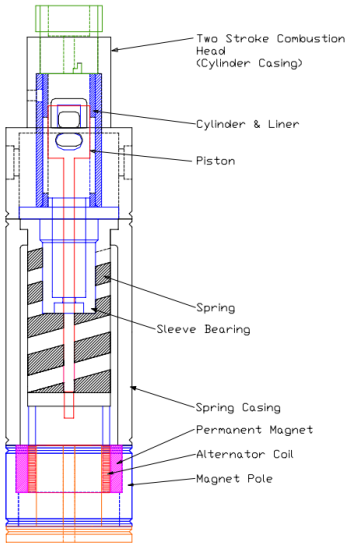

Figure 2.4: Linearly-oscillating miniature internal combustion engine (MICE) featuring a linear alternator for energy harvesting, a spring as rebound device and a combustion chamber based on two-stroke operation [2].

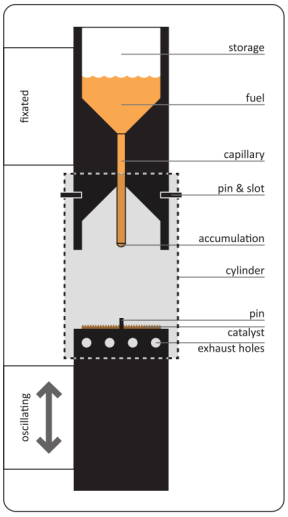

Figure 2.5: Schematic illustration of a free piston device [65].

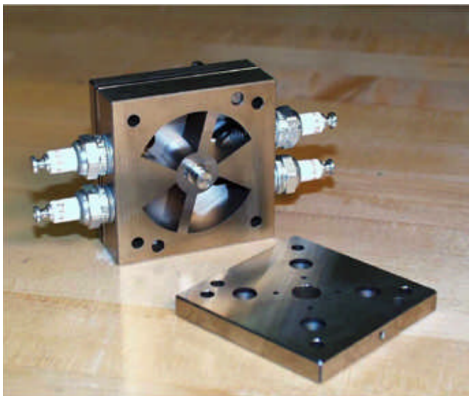

Figure 2.6: Picture of swing engine developed by Dahm et al.

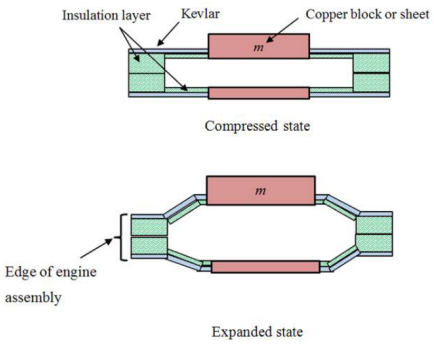

Figure 2.7: Cross-sectional view of compliant cylinder design comprising of two sandwich-structured diaphragms [10].

a small scale compliant cylinder engine for micro and mesoscale applications [10]. A design for a 1cc four-stroke compliant engine was proposed, depicted in Figure 2.7.

2.4.2. FUEL EXHAUST AND FUEL DELIVERY

The combustion products of a chemical actuator should be transported out of the reaction chamber by a certain exhaust mechanism. A fuel mixture or pressurized gas should be transported into the expansion chamber by means of the fuel delivery mechanism. Since both mechanisms often take the form of a valve, they are treated together. Passive valves will be categorized by their mechanical layout. Active valves will be categorized by actuation type: electromagnetic, electrostatic, piezoelectric or thermal expansion.

PASSIVE VALVES

Passive valves are well suited for miniature engines since they do not need a power source, cabling or micro-controllers to be operated, which can be dominant in the total mass budget. The first type of passive valves investigated is the pressure-actuated passive valve. The reciprocal motion of a piston in a typical two-stroke engine creates a variable pressure profile in the expansion chamber that can be passively exploited for fuel delivery. When the piston moves towards bottom dead center, the negative pressure difference arisen is able to suck fuel inside the reaction chamber. A version of this passive pressure-actuated valve is the reed valve

which is widely implemented in two-stroke engines [30]. Also, previously, the piston-controlled port was state-of-the-art in carburetor engines, where a port in cylinder wall was exposed or closed by piston position [30]. Mechanical layouts of passive valves that could be used in micro-scale are depicted in Figure 2.8 [27].

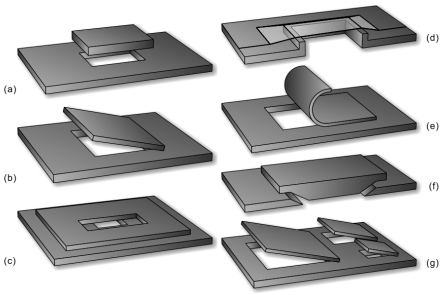

Figure 2.8: Schematic drawings of several microvalve design concepts. (a) Vertically translating plate; (b) Tilting plate; (c) Horizontally translating (sliding) plate; (d) Vertically translating membrane (cross-section); (e) Bending plate; (f) Needle (cross-section); (g) Scaling valve array [27]

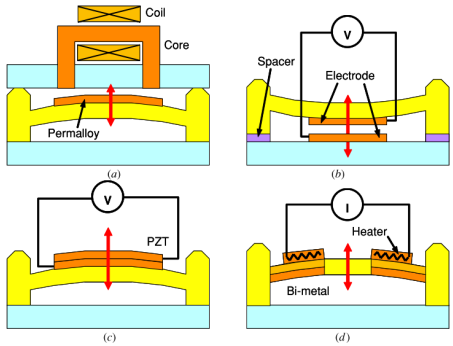

Figure 2.9: chematic overview of active valve actuation concepts: electromagnetic (a), electrostatic (b), piezoelectric (c), thermal (d) [52].

ACTIVE VALVES

An overview of the active valve concepts found in literature is depicted in Figure 2.9. An electromagnetic valve relies on the electromagnetic attraction of a conducting coil and another form of a magnet. Microfabrication techniques allow a coil to be integrated on a membrane making very compact design possible [45][52]. Nonetheless, electromagnetic actuators suffer from low actuation forces and high power consumption compared to electrostatic valves[27].

Electrostatic valves use an actuator that generates force when voltage is applied between two conducting electrodes. Electrostatic actuators are easy to implement in small-scale valve designs since microfabrication processes offer conductive structural materials like silicon [35]. A benefit of electrostatic valves is that they have very low actuation times and favourable force scaling [35]. A disadvantage of electrostatic actuation is that, identically to piezoelectric elements, they require relatively large operation voltages to obtain generate sufficient force. In microvalves, electrostatic actuators are generally integrated on rigid silicon membranes [66][78] or flexible membranes [36][52].

Piezoelectric valve use actuators that provide useful work by the induced strain in piezoelectric materials when submitted to an electric field [27]. The piezoelectric elements have very high actuation speeds and benefit from very high theoretical work density [27]. However the strain is limited (to less than 0.1%), so motion-amplification mechanisms as bimorphs [71] or piezostacks [12] are needed if significant stroke is necessary [52].

Thermal expansion valves are valves that exploit the thermal expansion of materials to move valve mechanisms. They often have slow actuation time and high power consumption. Typical examples of the thermal actuators used are bimetallic and thermopneumatic actuators [5, 52, 76].

INJECTORS

The last category of this section is the injector category. Injectors manipulate fluid properties as pressure or contact angle to expel fuel to an ignition area. A conventional combustion engine injector uses a nozzle with single, hole, multi-hole or pintle type orifice [30]. Formerly, pressurization was often performed by electromagnetically driven plungers. Current state-of-the-art relies almost solely on piezoelectric actuation. A passive injector concept is proposed by van den Heuvel where a capillary tube is penetrated by a pin and subsequently causes a fuel spray over a catalyst surface [65], depicted in Figure 2.5. Developments in the printing industry contributed significantly to droplet-on-demand technology. Individual droplets can be expelled from a nozzle after a pressure pulse supplied by a piezoelectric, electrostatic or thermal heater element [26]. Another relevant concept to mention is droplet manipulation using electrowetting in digital microfluidics, where the contact angle of droplets is controlled by varying electric field across a dielectric [51]. With this technique, a single droplet can be dispensed from a reservoir and transported over an electrode pattern, which is visualised in by an example Figure 2.10 [40]. Lastly, capillary auto-ejection could be a promising in-

jection concept [46] which uses capillary force to drive a liquid column through a nozzle with sufficient speed for droplet generation.

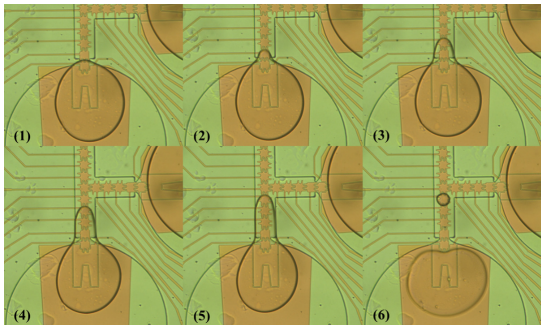

Figure 2.10: Example of droplet splitting and subsequent droplet acceleration over an electrode array [40].

2.4.3. IGNITION MECHANISM

Several concepts exist to bring a fuel mixture to combustion temperature. The spark plug, which is probably most widely known, is a system where a spark between two electrodes is produced to ignite the air-fuel mixture in the combustion chamber of an engine [28]. Although spark plugs are common in normal-sized conventional engines, they are scarce in the field of miniature engines. Dahm et al proposed a design for a micro-igniter consisting of a 790μm thick ceramic insulator rod and two electrodes in the form of 125μm tungsten filaments [18].

A second ignition concept is a glow plug. They are essentially resistive elements heated up by an electrical current driving through. They are widely used in conventional engines featuring compression ignition [28]. In the last decade, significant developments are made in miniaturization of glow plugs. A typical on-chip glow plug ignitor comprises a film of conductive material that is positioned at the inner wall of the reaction chamber [81]. An example of a glow plug ignitor is given in Figure 2.11 [39].

Combustion that is driven by flame front propagation, such as in spark-plug or glow-plug engines, suffers from thermal quenching. There exists a minimum distance from the wall of a combustion chamber where combustion occurs and this is determined by the ratio between heat generation and heat loss to the walls. The rest of the volume, the quenching volume, is an unburned layer close to the engine walls [62]. As size is reduced in miniature engines, the quenching volume becomes dominant over combustion volume, which has a detrimental effect on power produced [58].

Studies by Sher et al. and Aichlmayr et al. investigated the use of homogeneous charge compression ignition (HCCI) in miniature engines and found that HCCI leads to significantly reduced quenching [1, 59], although significant pressure buildup is necessary to initiate combustion. No igniter component is needed during operation, however another device should be present to initiate the startup cycle.

Lastly, a promising passive ignition concept is a catalyst in combination with hydrogen peroxide fuel. Hydrogen peroxide coming in contact leads to rapid decomposition (not actual combustion) of hydrogen peroxide, which happens without any active igniter. This mitigates the quenching issue completely. Lightweight implementation (« 1g) is possible in the form of a thin catalyst layer [65].

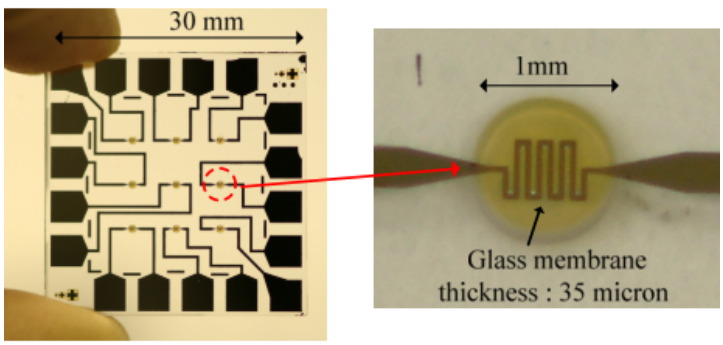

Figure 2.11: Photo of an fabricated array of micro-igniters [39].

2.5. CONCEPT GENERATION

Based partly on state-of-the-art technology and partly on own design, a design option tree is generated for each subsystem, depicted in Appendix B.1. The goal of a design option tree is to divide the different concept solutions for each subsystem into categories. This assists in covering the whole design space and prevents leaving concept solutions unnoticed. Before a more exhaustive concept comparison, a prior investigation is done to eliminate unfeasible concept solutions. This convergence step reduces the amount of solutions to three to five feasible concept solutions per subsystem. Appendix B.2 describes this initial selection and includes the reasoning for concept elimination. The remaining concepts are depicted schematically in Figure 2.12. Concepts that are fully based on own design and not seen in literature, are highlighted in purple.

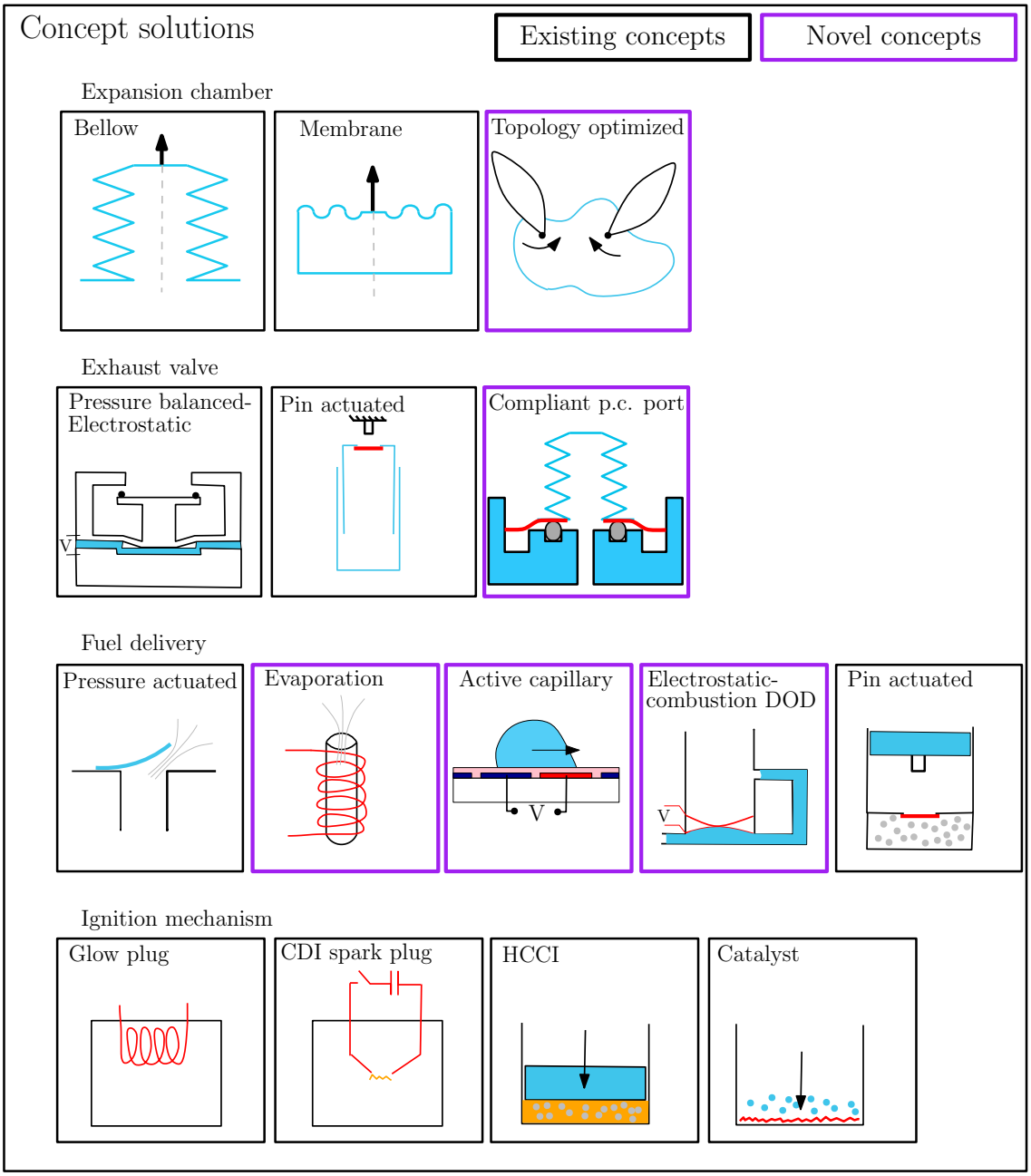

Figure 2.12: Schematic representation of the concept solutions per subsystem. Novel concepts are highlighted in purple

2.6. CONCEPT EVALUATION

This section describes the evaluation and selection of the generated concept solutions for every subsystem. Table 2.2 depicts the qualitative evaluation of the concept solutions of the expansion chamber, fuel exhaust, fuel delivery and ignition system respectively. Each concept solution is qualitatively criticized with regard to the following criteria. Although academic relevance is not a performance criterion, it was added to create an extra incentive for relevant academic contribution.

1. Mass
2. Efficiency
3. Reliability
4. Manufacturability
5. Complexity
6. Academic relevance

The following performance scores are assigned: excellent (++), good (+), average (o), poor (-), very poor (- -). A table with explanation for every criteria score is given in appendix B.3.

Concept description	Mass	Efficiency	Reliability	Manufacturability	Complexity	Academic relevance
Expansion chamber						
Bellow	+	++	+	+	o	o
Membrane	+	+	+	+	+	o
Topology optimized	++	++	-	- -	- -	++
Exhaust valve						
Pressure balanced electrostatic actuation	-	o	- -	-	- -	++
Pin actuated	+	++	+	++	+	+
Compliant piston-controlled port	+	++	++	+	+	++
Fuel delivery						
Pressure actuated valve	++	++	+	+	++	- -
Cyclic fuel evaporation by heating	-	- -	o	o	o	+
Active capillary droplet delivery	++	++	+	- -	-	++
Electrostatic-combustion pressurized DOD	o	o	- -	- -	- -	++
Pin-actuated	+	+	o	o	-	o
Ignition mechanism						
Glow plug heated by Joule heating	+	- -	+	o	-	o
Homogeneous charge compression ignition	+	-	+	o	-	o
HCCI	o	++	o	+	o	+
Catalytic droplet decomposition	+	++	++	+	++	++

Table 2.2: Concept comparison with criteria scores of the different subsystems. Scores: excellent (++), good (+), average (o), poor (-), very poor (- -). Active capillary fuel delivery is not new in microfluidic applications, but has not been used for fuel delivery yet.

2.7. DESIGN PROPOSAL

Taking aforementioned concept evaluation into consideration it is chosen to proceed with further development of a compliant piston-controlled port as exhaust valve concept in combination with a bellow as expansion chamber. A passive exhaust valve that is being opened by the deformation of a compliant expansion chamber is not earlier designed or demonstrated. As fuel delivery and ignition concept, it is chosen to use an active capillary injection device that transports droplets of hydrogen peroxide against a passive catalyst surface. The schematic design and working principle of the exhaust valve and expansion chamber are briefly

explained in 2.7.1. The schematic design and working principle of the injection mechanism are briefly explained in 2.7.2.

2.7.1. EXPANSION CHAMBER AND EXHAUST VALVE

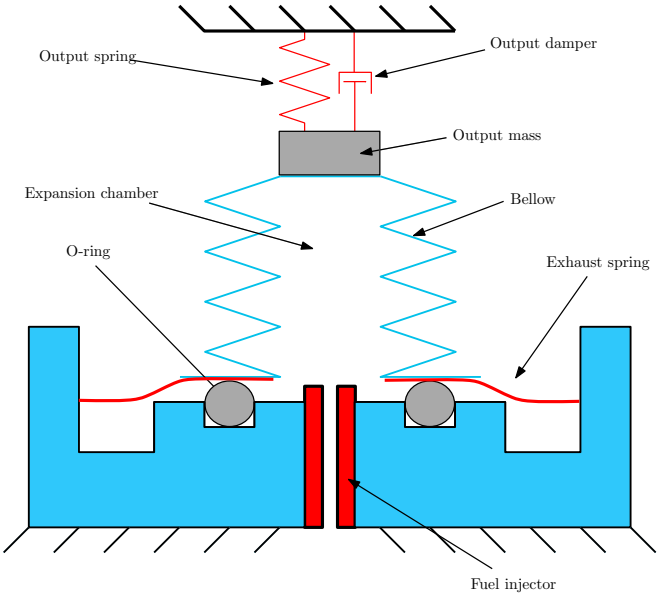

Figure 2.13: Schematic of the bellow

Figure 2.13 visualizes the main parts of the expansion chamber assembly: a bellow connected to an exhaust spring, an expansion chamber, fuel injector, O-ring as well as an output mass, spring and damper. After the pressurization event, pressure is increased in the expansion chamber. This event is visible in Figure 2.14. The piston mass will move upward, simultaneously putting the bellow under tension. Eventually, the bellow tension force overcomes the pretension force of the exhaust spring and a gap will be introduced between the bottom surface of the bellow and the O-ring. Through this gap the pressurized gas will flow outwards of the expansion chamber, escaping upwards through the leafs of the circular exhaust spring (visualised in Figure 2.15). Subsequently, after the piston reaches maximum stroke, the piston will move downward and bellow tension will decrease until the exhaust spring touches the O-ring again and reseals the chamber. After the piston reaches bottom position, the pressurization event occurs again and the two-stroke cycle repeats.

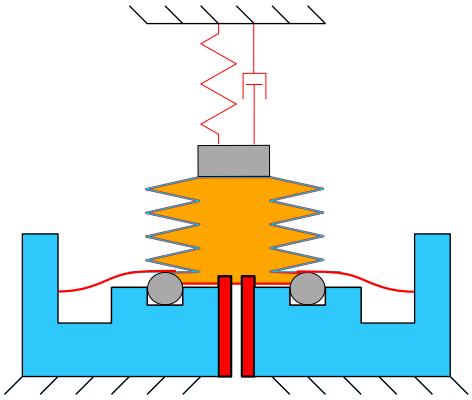

Figure 2.14: Pressurization event where pressure increases and piston begins to accelerate upwards

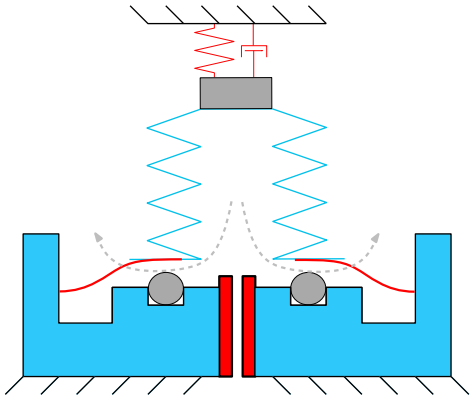

Figure 2.15: Piston reaches top position and internal bellow force forces pulls exhaust spring in open position which leads to exhaust event

This system relies on a complex interplay between pressure forces and elastic forces of the exhaust spring and bellow. Actuator variables as stiffnesses, pretension distances, chamber volumes as well as flow resistances should be chosen correctly to guarantee successful timing and functioning of the device.

2.7.2. INJECTION MECHANISM

The aforementioned expansion chamber will be pressurized by the catalysis reaction of hydrogen peroxide. If liquid hydrogen peroxide comes into contact with a catalyst Manganese(II) acetate, the liquid will decompose into oxygen gas and water, while additionally releasing heat due to the exothermic nature of the reaction [47]. The gas and heat generation will pressurize the expansion chamber. The catalyst reaction does not have to be initiated by active components as is the case with other fuels. It also mitigates the quenching problem in miniature actuators completely.

To move a droplet from the fuel reservoir onto the catalyst, the fuel will be subjected to a splitting event and an accelerating event using electrowetting-on-dielectric (EWOD). EWOD allows control of individually addressable droplets on an array of electrodes using electrostatic forces [24]. EWOD has strong advantages over other fuel delivery methods as it has a high switching response, no joule heating, no need for moving parts like pumps and valves, and very low power requirements [50].

The injection module is integrated into the compliant expansion chamber as is visualised in Figure 2.16. The reservoir is mounted inside the expansion chamber in a floating configuration, in order to equalize all pressures around the fuel body. The core part of the fuel delivery system is the droplet injection module, which is located on the disk-shaped substrate visualised in purple. Multiple droplet injection modules can be positioned on this substrate, pointing radially outwards to the catalyst ring (depicted in green).

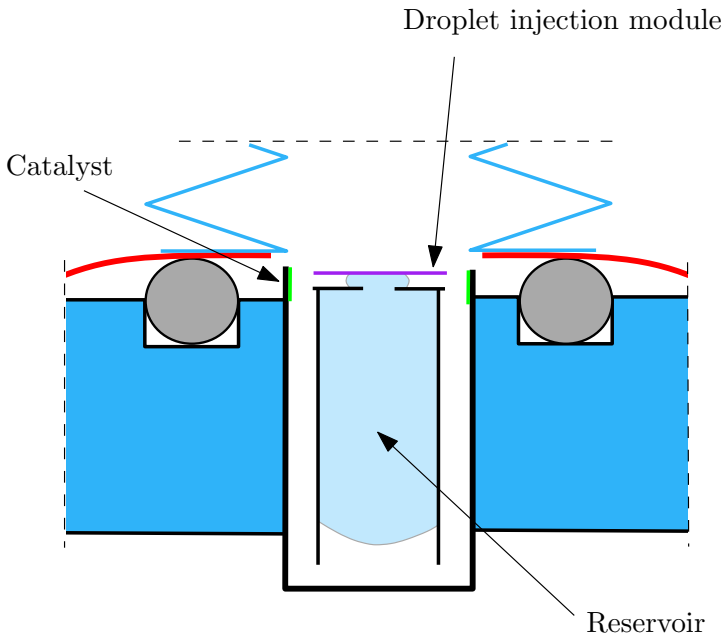

Figure 2.16: Schematic of a single injection module

The general architecture of the electrode array on this substrate is depicted in Figure 2.17. By actuating the electrodes in the splitting section, a droplet can be dispensed from the reservoir. Subsequently, the electrodes in the acceleration section will be sequentially switched to accelerate the droplet towards the catalyst surface.

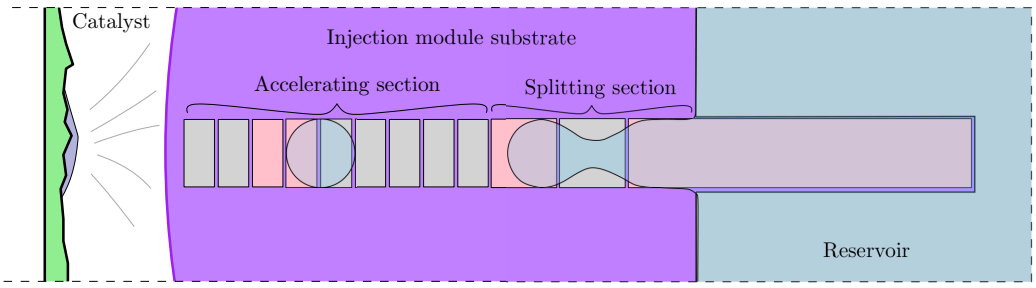

Figure 2.17: Schematic of a single injection module. Actuated electrodes are visualised in pink.

3

COMPLIANT EXPANSION CHAMBER WITH INTEGRATED PASSIVE EXHAUST VALVE

3.1. INTRODUCTION

In this chapter, a mathematical model is constructed to predict actuator performance of the expansion chamber and exhaust valve. Also, a measurement setup is developed to characterize the system behaviour of the harmonic expanding motion of the bellow and opening movement of the exhaust valve. The goal of the measurement setup is not to deliver optimum power output to reach the research goal, but it will serve both as a proof-of-concept as well as a measurement setup to validate the developed mathematical models for future designs. The organisation of the chapter is visualised in Figure 3.1.

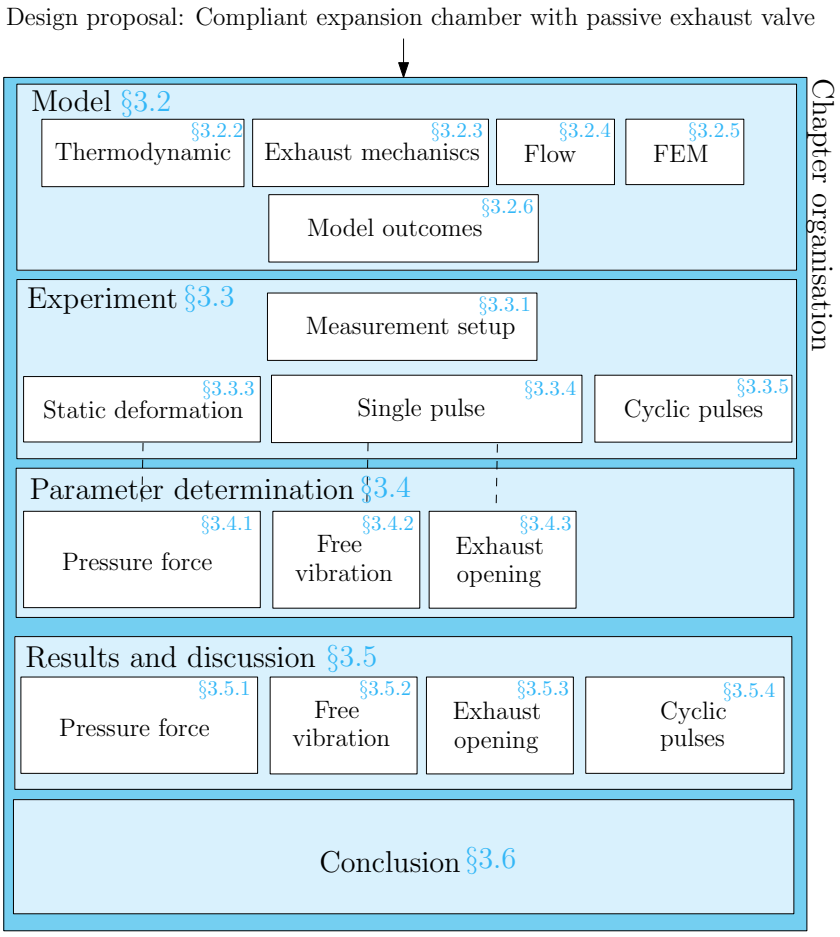

Figure 3.1: Chapter organisation

3.2. MODEL

3.2.1. ACTUATOR MODEL

To predict the actuator dynamics and actuator performance, and to be able to make choices for the geometry of the experimental setup, an actuator model is constructed. Figure 3.2 gives a schematic of the workflow of the different submodels within this master model, including arrows representing the variables that are communicated between/to the specific models. Figure 3.5 depicts the design variables of the expansion chamber and exhaust valve.

1. Thermodynamic model: analytic model that predicts piston dynamics, temperature and pressure of a control volume in the chamber
2. Exhaust mechanics model: analytic model that predicts exhaust spring opening movement
3. FEM: Finite element model to predict nonlinear force-displacement curve of exhaust spring and load spring based on geometry and topology.
4. Flow model: analytic model that predicts inlet and outlet mass flow functions.

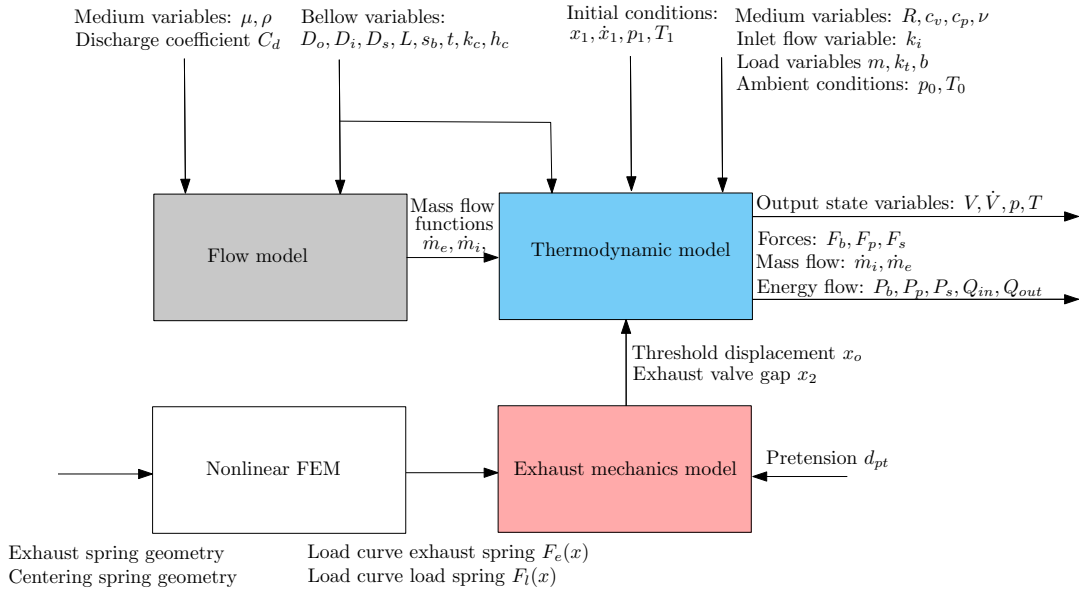

Figure 3.2: Model workflow

During model development, a parallel process occurs where the design variables are chosen and updated to ensure proper exhaust functioning or guarantee stable operation within the bellow limits. This iterative process requires constant iteration of model variables and checking of model assumptions. As a first step, an initial set of design variables of the bellow and O-ring is chosen as a starting point, summarized in Figure 3.4. This bellow choice is based on off-the-shelf bellow availability. This bellow size is sufficiently small such that experimental conclusions and fabrication methods could be used in a final design of comparable size. Figure 3.3 visualises the specific bellow chosen, including a euro coin for size comparison.

Figure 3.3: Bellow next to a one euro coin

Design variable	Value
Bellow outer diameter D_o	10.1 mm
Bellow inner diameter D_i	5.08 mm
Bellow length L	4.32 mm
Maximum bellow stroke Δx	1.78 mm
O-ring sealing diameter D_s	5.46 mm
Bellow stiffness s_b	5920 N/m

Figure 3.4: Bellow and O-ring parameters

3.2.2. THERMODYNAMIC MODEL

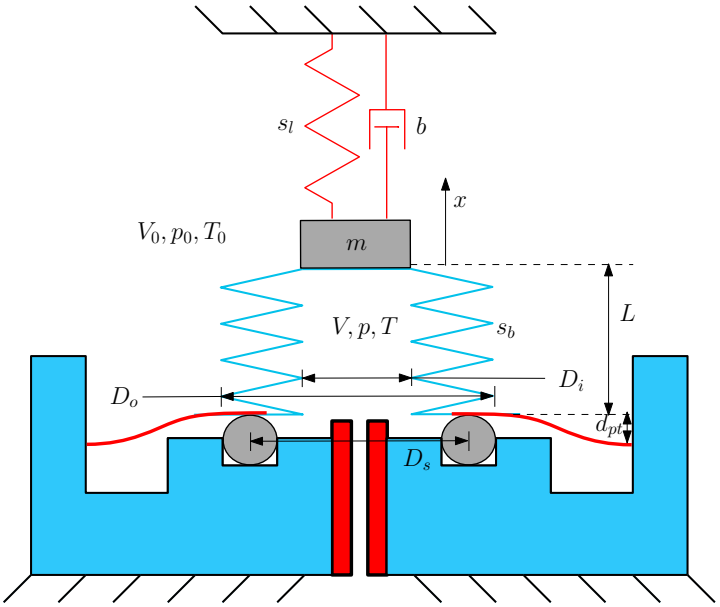

Figure 3.5: Model parameters of the expansion chamber with integrated exhaust valve

The mathematical model to analyse the dynamic behaviour of the schematic from Figure 3.5 is constructed by applying the following physical laws [54]. First, Newton's second law is applied to a lumped piston mass m(Eq.3.1). In this equation x represents the piston displacement measured from the undeformed state of the bellow, p the chamber pressure, p_0 the ambient pressure and A the effective thrust area. The summed stiffness s represents the stiffness of the bellow s_b and load spring s_l, mounted in parallel, and b represents the damping coefficient of the load. In equation 3.2, conservation of energy is applied to the control volume of the bellow cavity, where c_v represents the volumetric heat capacity, ρ the air density, V the bellow cavity volume, T the control volume temperature, T_0 the ambient temperature and h the equivalent heat transfer coefficient. The inlet flow energy, outlet flow energy and combustion heat generation are represented by $\dot{m}_i E_i$, $\dot{m}_e E_e$ and $\dot{Q}$ respectively. Conservation of mass and the ideal gas law are also applied to the control volume, as represented in equation 3.3 and 3.4 respectively, where R represents the gas constant. Earlier research by Preetham et al. used the same modelling assumptions and underlying physical laws, however they used discrete impulse cooling and heating steps to model exhaust and combustion processes without mass inflow or outflow [54]. The current model uses continuous exhaust and inlet mass flow functions to model the transient behaviour of the gas inflow and outflow.

$$m\ddot{x} = (p - p_0)A - b\dot{x} - sx - mg \tag{3.1}$$

$$\frac{d}{dt}[c_v \rho V T] = -h(T - T_0) - p\dot{V} + \dot{m}_i E_i - \dot{m}_e E_e + \dot{Q} \tag{3.2}$$

$$\dot{m}_i - \dot{m}_e = \frac{d}{dt}[\rho V] \tag{3.3}$$

$$\rho = \frac{p}{RT} \tag{3.4}$$

Volume difference ΔV, pressure difference Δp and temperature difference ΔT are defined in Equations 3.5, 3.6 and 3.7 respectively. Inlet and exhaust energy flows are described in Equation 3.9 and 3.10 respectively, with c_p being the specific heat capacity of the gas.

$$V = V_0 + \Delta V \tag{3.5}$$

$$\Delta p = p - p_0 \tag{3.6}$$

$$\Delta T = T - T_0 \tag{3.7}$$

$$\Delta V = xA \tag{3.8}$$

$$E_i = c_p T_0 \tag{3.9}$$

$$E_o = c_p T \tag{3.10}$$

Equations 3.5 until 3.10 are substituted back into 3.1,3.2,3.3 and 3.4. Subsequent application of the chain rule and rearranging terms leads to the following set of differential equations in state-space form with state variables $\Delta V, \dot{V}, \Delta T, \Delta p$.

$$\Delta \ddot{V} = \frac{1}{m}[A^2 \Delta p - b\dot{V} - s\Delta V - mgA] \tag{3.11}$$

$$\Delta \dot{p} = \frac{R}{c_v(V_0 + \Delta V)}\left[-\Delta \dot{V}(p_0 + \Delta p)(1 + \frac{c_v}{R}) - h\Delta T + \dot{m}_i c_p T_i - \dot{m}_e c_p (T_0 + \Delta T)\right] \tag{3.12}$$

$$\Delta \dot{T} = \frac{\Delta \dot{p}(T_0 + \Delta T)}{p_0 + \Delta p} + \frac{\Delta \dot{V}(T_0 + \Delta T)}{V_0 + \Delta V} + \frac{R(\dot{m}_e - \dot{m}_i)(T_0 + \Delta T)^2}{(p_0 + \Delta p)(V_0 + \Delta V)} \tag{3.13}$$

This system of equations can be numerically solved after obtaining mass flow functions $\dot{m}_i$ and $\dot{m}_e$, and exhaust opening gap x_2 from the models described in 3.2.4 and 3.2.3 respectively. The variables A, V_0, s can be determined by Equation 3.14, 3.15, 3.16 respectively. Although it seems logical to assume the effective thrust area A to be $\frac{\pi}{4}D_i^2$, the air between the bellow corrugations also provides elongation forces, increasing the effective thrust area. A derivation of the effective thrust area A is given in Appendix A.3. The dead volume V_{dead} describes the volume of the inlet canals under the bellow.

$$A = \frac{\pi}{8}(D_o^2 + D_i^2) \tag{3.14}$$

$$V_0 = V_{dead} + AL \tag{3.15}$$

$$s = s_b + s_l \tag{3.16}$$

The average output power can be calculated by averaging the power dissipated in the damper, as in Equation 3.17. This power is directly related to the lift production of the FWMAV as described in Appendix A.1.

$$P_{out} = \frac{\int_0^{t_1} b\dot{x}^2 dt}{t_1} \tag{3.17}$$

3.2.3. EXHAUST MECHANICS

The force interplay between the bellow corrugations, exhaust spring and cavity pressure will determine how much and at which time the exhaust gap will be opened. In this section, the exhaust opening distance x_2 is related to the relevant design variables. If inertial forces are neglected, the quasi-static equilibrium of the bottom bellow endplate, where the exhaust spring is connected to, can be described by Equation 3.18.

$$-\Delta p A_e + s_b x - F_e(d_{pt} + x_2) + F_N = 0 \tag{3.18}$$

where $F_e(d_{pt} + x_2)$ is the nonlinear force-displacement function of the exhaust spring, x_2 the exhaust opening distance, F_N the normal force exerted by the o-ring and A_e the effective exhaust pressure area can be described by equation 3.19. Note that a positive A_e will mean that pressure will exert a closing force on the exhaust mechanism. A_e is relatively uncertain and will be experimentally identified.

$$A_e = \frac{\pi}{4}(D_o^2 - D_s^2) \tag{3.19}$$

The opening threshold distance x_o, the distance at which the exhaust opening event will start to occur, can be described by Equation 3.20 after setting F_n and x_2 to zero. Equation 3.20 will be designated as the exhaust opening criterion from now on.

$$x_o = \frac{F_e(d_{pt}) + \Delta p A_e}{s_b} \tag{3.20}$$

The exhaust opening gap x_2 can be described by the following continuous function, which includes a logistic sigmoid function with steepness g_1 to capture the discrete nature of the opening event in a continuous function.

$$x_2 = \left[F_e^{-1}(s_b x - \Delta p A_e) - d_{pt}\right] \frac{1}{1 + e^{-g_1(x - x_o)}} \tag{3.21}$$

Although the exhaust spring stiffness does not influence the effective bellow stiffness while the exhaust is closed, it is presumed that the exhausts spring, mounted in series with the bellow, changes the stiffness s_b while the exhaust is opened. This effect can be implemented by making the stiffness s_b displacement dependent. Note that $s_{b,i}$ is the initial bellow stiffness and $s_{e,lin}$ is a the stiffness of the exhaust spring, obtained from Figure 3.11. $s_\infty = 10^5 N/m$ is a superior stiffness to eliminate the effect of $s_{e,lin}$ before x_o is reached.

$$s_b = \left[\frac{1}{s_{b,i}} + \frac{1}{s_{e,lin} + \frac{s_\infty}{1+e^{g_1(x-x_o)}}}\right]^{-1} \tag{3.22}$$

However, for the initial model evaluations, it assumed that bellow stiffness s_b stays constant and is not altered during opening, since the opening event should be very short favourably and will only change the stiffness for a fraction of the time. The effect will be discussed later.

3.2.4. FLOW MODEL

To determine if this time-varying exhaust gap is large enough to relieve sufficient pressure in the available time, the exhaust mass flow function was constructed in this section. Also, it describes the inlet mass flow function. Several flow modelling assumptions are compared by conducting an analysis of a simplified version of the expansion chamber. In this simplified version, we examine the emptying of a reservoir with constant volume V_t, pressure p_t, temperature T_t and gas density ρ_t. The air inside this tank is discharged radially through a ring-shaped slot with length l_t, height h_t and flow area $A_{flow} = \pi D h_t$, depicted in Figure 3.7. This simplified control volume will correspond to the bellow geometry depicted in Figure 3.6 by the purple dashed line. Important to note here is that the simplified geometry will lead to an overestimation of the viscous losses due to the longer and (on average) thinner slot. Furthermore, the control volume is considered to be adiabatic and the radial slot is considered to be the only restrictive flow element. Also, the curvature of the gap is considered to be negligible.

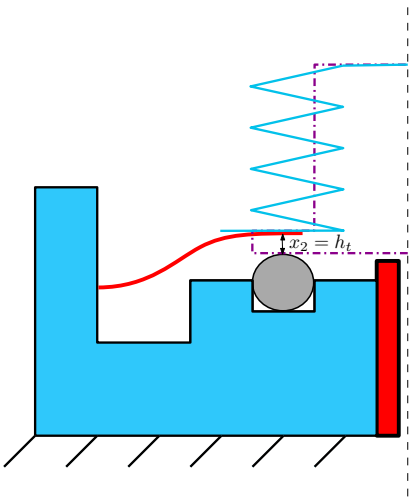

Figure 3.6: Control volume of simplified tank compared with bellow dimensions

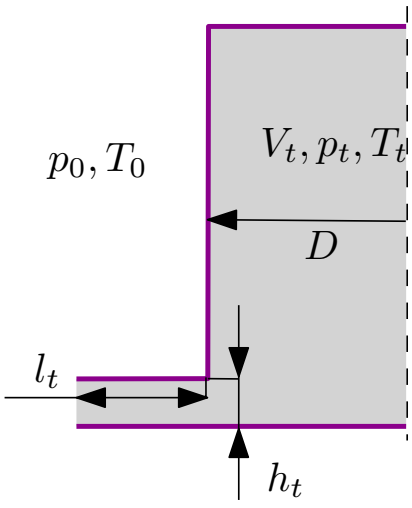

Figure 3.7: Schematic of simplified tank

To enforce conservation of energy, conservation of mass and the ideal gas law, equations 3.23, 3.24 and 3.25 are applied respectively to the control volume of air inside the tank.

$$\frac{d}{dt}[c_v \rho_t V_t T_t] = -\dot{m}_{e,t} c_p T_t \tag{3.23}$$

$$\frac{d}{dt}[\rho_t V_t] = -\dot{m}_{e,t} \tag{3.24}$$

$$\rho_t = \frac{p_t}{R T_t} \tag{3.25}$$

Equations 3.23, 3.24 and 3.25 are reduced to equation 3.26 and 3.27 and solved numerically once the mass flow rate is obtained.

$$\dot{p}_t = \frac{-\dot{m}_{e,t} c_p T_t R}{c_v V_t} \tag{3.26}$$

$$\dot{T}_t = \frac{T_t \dot{p}_t V_t + \dot{m_{e,t}} T_t^2 R}{p_t V_t} \tag{3.27}$$

Subsequently, an analytic expression for the mass flow rate is sought as a function of the time-varying gap geometry h_t, which represents the real exhaust opening gap x_2. The time-varying exhaust gap h_t is determined from x_2 in Equation 3.21, assuming A_e is zero and a bellow displacement function as described by Equation 3.28.

$$x = \frac{\Delta x}{2} \sin(2\pi f t) \tag{3.28}$$

Determining the mass flow rate is less straightforward and requires careful inspection of the consequence of different flow assumptions. Although it is desirable to determine the mass flow rate as accurately as possible, it is even more essential to give a bottom-limit estimate for the mass flow. In this way, it is guaranteed that the exhaust valve will expel enough air during each stroke. Table 3.1 gives an overview of the different modelling options for the mass flow.

Now the mass flow rate can be obtained from different models, the pressure profile and temperature can be determined by solving equations 3.26 and 3.27 numerically. The gap height h_t will be considered time-varying and thus set equal to x_2. Figure 3.8 depicts the displacement x and h_t as a function of time. Pressure profile p_t and temperature profile T_t of the air in the tank for different modelling methods are also depicted in the middle and bottom of the figure.

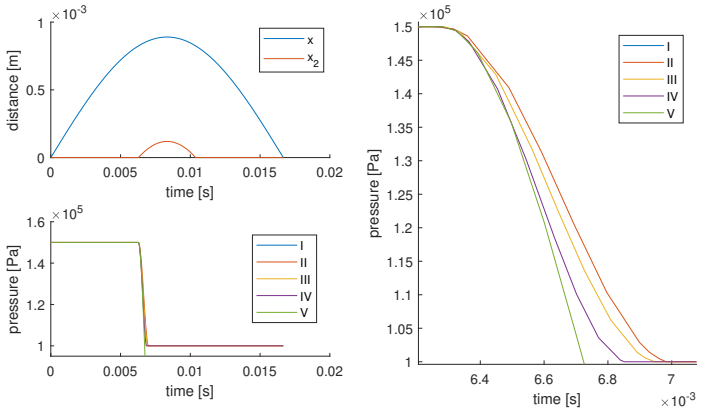

Figure 3.8: Top left: exhaust opening displacement x_2 and piston displacement x. Bottom left: Tank pressure p_t. Right: Tank pressure p_t just after opening. Input parameters: $p_t(t=0) = 1.5bar, T_t(t=0) = 293K, p_0 = 1bar, T_0 = 293K, \mu = 18 * 10^{-6} Pa * s, D = 5.46mm, V_t = 4.4 * 10^{-5} m^3, f = 30Hz, s_b = 5920N/m, F_e$ extracted from 3.2.5

Index	Assumptions	Mass flow	Source
I	- Incompressible flow - Inertial effects are significant - Viscous effects are significant - Gap flow has ambient air density ρ_0 - Subsonic	$\dot{m} = \left[\frac{A_{flow}^2 C_d^2}{\rho_0}\right]\left[\frac{-12\mu l_t}{\pi D h_t^3} + \sqrt{\left(\frac{12\mu l_t}{\pi D h_t^3}\right)^2 + \frac{2\Delta p \rho_0}{A_{flow}^2 C_d^2}}\right]$	[19, 31]
II	- Incompressible - Inertial effects are significant - Viscous effects are negligible - Gap flow has ambient air density ρ_0 - Subsonic	$\dot{m} = C_d A_{flow}\sqrt{\Delta p \rho_0}$	[19, 70]
III	- Incompressible - Inertial effects are significant - Viscous effects are negligible - Gap flow has tank air density ρ_t - Subsonic	$\dot{m} = C_d A_{flow}\sqrt{\Delta p \rho}$	[19, 70]
IV	- Compressible - Inertial effects are significant - Viscous effects are negligible - Flow accelerates isentropically to ρ_{gap} - Subsonic	$\dot{m} = \frac{p A_{flow}}{\sqrt{RT}}(\frac{p}{p_0})^{-1/\gamma}\sqrt{\frac{2\gamma}{\gamma-1}\left[(\frac{p}{p_0})^{\frac{\gamma-1}{\gamma}} - 1\right]}$	[63**?**]
V	- Compressible - Intertial effects are significant - Viscous effects are negligible - Flow accelerates isentropically to ρ_{gap} - Choked	$\dot{m} = \frac{p A_{flow}}{\sqrt{RT}}\sqrt{\gamma}\left[\frac{\gamma+1}{2}\right]^{\frac{\gamma+1}{2(1-\gamma)}}$	[63]

Table 3.1: Different methods to model the mass flow through the exhaust valve. The assumptions, the mass flow rate equation and source are stated for each method.

From the pressure and temperature profile in Figure 3.8 it can be noted that for the first four flow models, the pressure equilibrates with ambient pressure within a fraction of the total exhaust opening time. Although model V, which assumes choked flow, is not applicable for this pressure ratio $\frac{p}{p_0}$, it is chosen to be included since critical pressure ratios may be reached in the inlet process. Subsequently, a correct mass flow model is chosen to be incorporated in the thermodynamic model for the exhaust valve and inlet. If one inspects Figure 3.8 further, it can be noted that the influence of viscous losses is negligible, since there is no apparent difference between p_t from model I and model II. In terms of pressure relief performance (of the applicable models I until IV), model II gives the most conservative estimate whereas model IV gives the most optimistic estimate. Also, model II offers reduced computing time compared to the other models. Therefore, it is chosen to incorporate model II in the thermodynamic model to guarantee sufficient pressure relief of the exhaust valve. Thus, the resulting exhaust mass flow will be determined by Equation 3.29 .

$$\dot{m}_e = C_d(x_2 \pi D_s)\sqrt{\Delta p \rho_0} \tag{3.29}$$

For the inlet mass flow function, it is chosen to assume model III, where density ρ_t is assumed. After a simplification using the ideal gas law (Eq. 3.4), the inlet mass flow function can be further reduced to Equation 3.30

$$\dot{m}_i = k_i(p_i - \Delta p) \tag{3.30}$$

where inlet flow constant k_i is dependent on the boolean inlet valve state as well as on the series flow resistance of all the inlet canals.

3.2.5. FEM ANALYSIS

At this point executing the thermodynamic model is possible, although a certain constant exhaust spring stiffness $s_{e,lin}$, pretension distance d_{pt} and load spring stiffness $s_{l,lin}$ have to be chosen. After iterating on these values, a combination was found which will lead to sufficient pressure relief in the exhaust opening stroke. Based on this notion, a circular flat exhaust spring geometry was sought with the following requirements. The maximum displacement δ_{max} is chosen such to allow more pretension distance d_{pt} than necessary, to allow mechanical tuning of the assembly in a later stage. The values of these requirements are depicted in Table 3.2.

$$\sigma_{VM}(\delta = \delta_{max}) < \frac{\sigma_{yield}}{SF_1}, \text{ where } \delta_{max} = SF_2(d_{pt} + x_{2,max}) \tag{3.31}$$

$$F_e(d_{pt}) = s_{e,lin} d_{pt} \tag{3.32}$$

Variable	Magnitude
σ_{yield}	1500 MPa
SF_1	1.2
SF_2	1.25
$x_{2,max}$	0.4 mm
$s_{e,lin}$	2600 N/m
d_{pt}	1.2 mm

Table 3.2: Exhaust spring requirements and design variables

In COMSOL, a finite element analysis was performed. The flat geometry was modelled with quadratic triangular shell elements and geometric nonlinearity was assumed. Figure 3.9 illustrates the modelled domain and the mesh distribution. A fixed constraint was applied at the outer edge of the circular spring domain at the location of the external clamping. A sandwich of exhaust spring sheet, bonding material and bellow endplate will be located inwards of the inner edge of the domain. Due to the superior bending stiffness of this ring-shaped sandwich, bending deformations are considered negligible inwards of the inner edge. Therefore a no-rotation (XY) constraint was applied to the inner edge. The load F_e was applied in Z-direction on this inner edge.

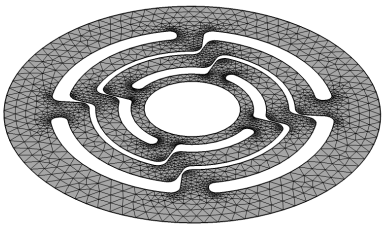

Figure 3.9: Mesh distribution: triangular elements with decreased element size near stress concentrations

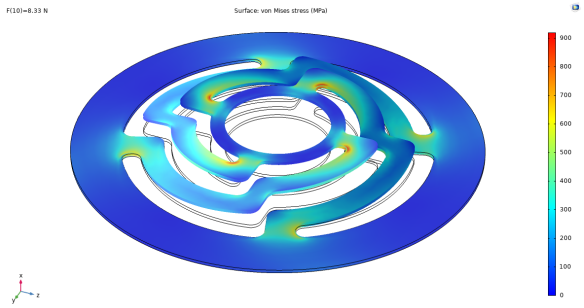

Figure 3.10: Stress distribution visualised on deformed geometry with applied axial force $F_e = 8.33N$. Maximum Von-Mises stress is 905 MPa.

A geometry was found that correlates well with the set requirements. The exhaust spring consists of a 0.3 mm thick flat circular spring including four bending leaf springs. Figure 3.10 visualizes the stress distribution of the maximum deformed state. For simplicity reasons, the load spring geometry was set identical to the exhaust spring geometry but with a thickness of 0.1 mm now. Figure 3.11 depicts the force-displacement relation for the two springs. A 3rd order polynomial is fitted through the data points, and the outcome is used as an input for in the exhaust mechanics model. For negative values of d_{pt}, the load-displacement curve is mirrored across the x-axis.

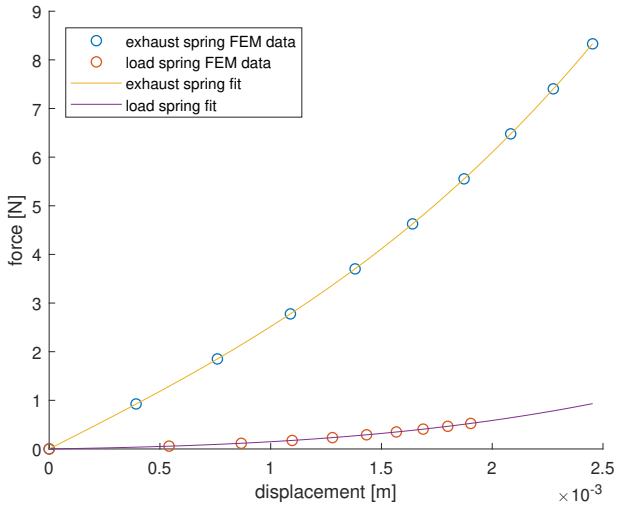

Figure 3.11: Force-displacement relation of the exhaust spring and load spring

3.2.6. INITIAL MODEL RESULTS

The models in aforementioned sections are combined according to the model workflow from Section 3.2 and can be solved for estimated measurement setup properties. To get an indication of the typical model results, the responses of different output variables are depicted in Figure 3.12. There is no reason to assume the model does not give appropriate results yet, since different phenomena as pressure increase at bottom piston position, pressure drop due to exhaust mass flow, and pressure decrease due to volumetric expansion can be observed. Next to the earlier defined outputs as displacements x, x_2, pressure p, temperature T, mass flows $\dot{m}_i, \dot{m}_e$, the model outputs that can be obtained includes piston forces $F_p = \Delta pA, F_s = -s\Delta x, F_b = -b\dot{x}, F_g = mg$ as outputs. Also, besides the average output power $P_{b,avg}$, the instantaneous power performed by the expanding gas $P_p = F_p\dot{x}$, spring $P_s = F_s\dot{x}$ and heat transfer $\dot{Q}_e = h\Delta T$ are useful model outcomes.

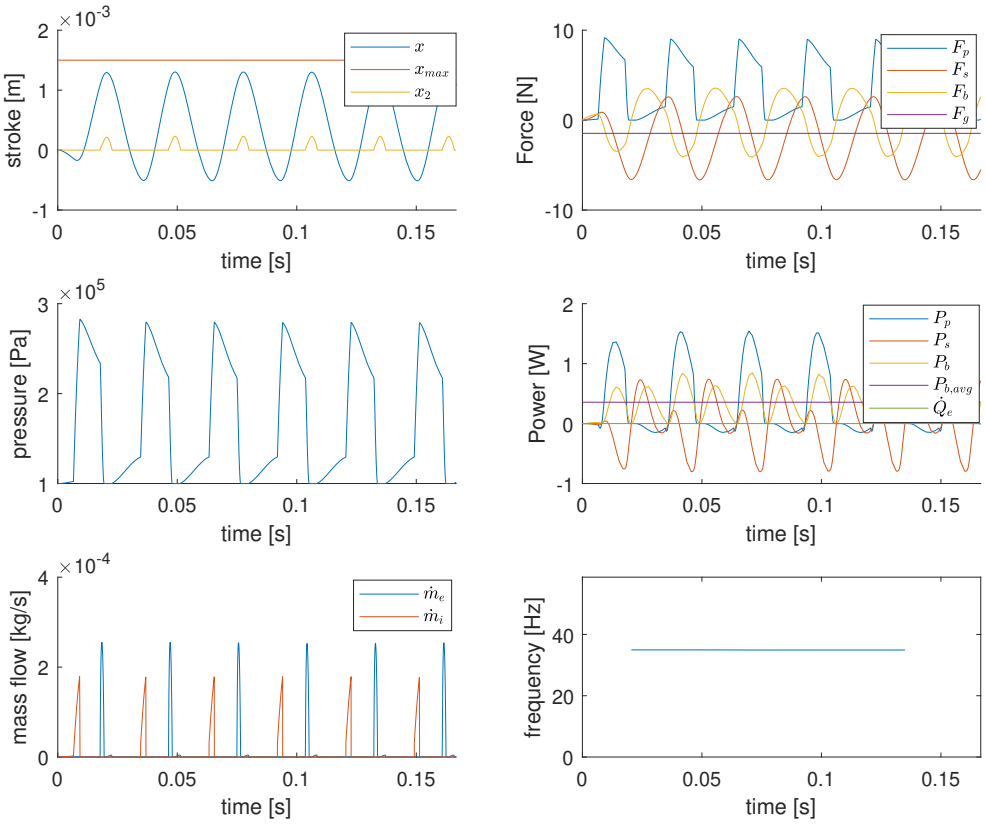

Figure 3.12: Model results, from left to right: displacements x, x_{max}, x_2, forces F_s, F_p, F_b, F_g, pressure p, powers $P_s, P_p, P_b, P_g, Q_{loss}$, mass flows $\dot{m}_e, \dot{m}_i$. Input parameters: (bellow variables from 3.4, $m = 0.15$kg, $s = 5920$N/m, $V_{dead} = 2.3 * 10^{-7}$m^3, $C_d = 0.7$[31], $d_{pt} = 2$mm, $b = 20$Ns/m, $k_i = 10^{-9}$kg/Pas, $p_i = 3.5 * 10^5$Pa, $Q_{cycle} = 0$W, $h = 0$W/K.

3.3. EXPERIMENT

To verify functioning of the proposed compliant expansion chamber and validate the model, an experimental study is conducted where the compliant expansion chamber with passive exhaust valve is fabricated and characterized in a measurement setup. A detailed characterization is necessary to gain full insight into the model and tune model variables such that a well-correlated model can be used for future designs.

3.3.1. MEASUREMENT SETUP

Figure 3.13 depicts the total measurement setup. Figure 3.15 gives a section view of the CAD of the measurement setup, excluding the pressurization system and control electronics. The relevant components are indicated with arrows. Figure 3.14 depicts a section view of the CAD of the compliant expansion chamber builtin in the measurement setup.

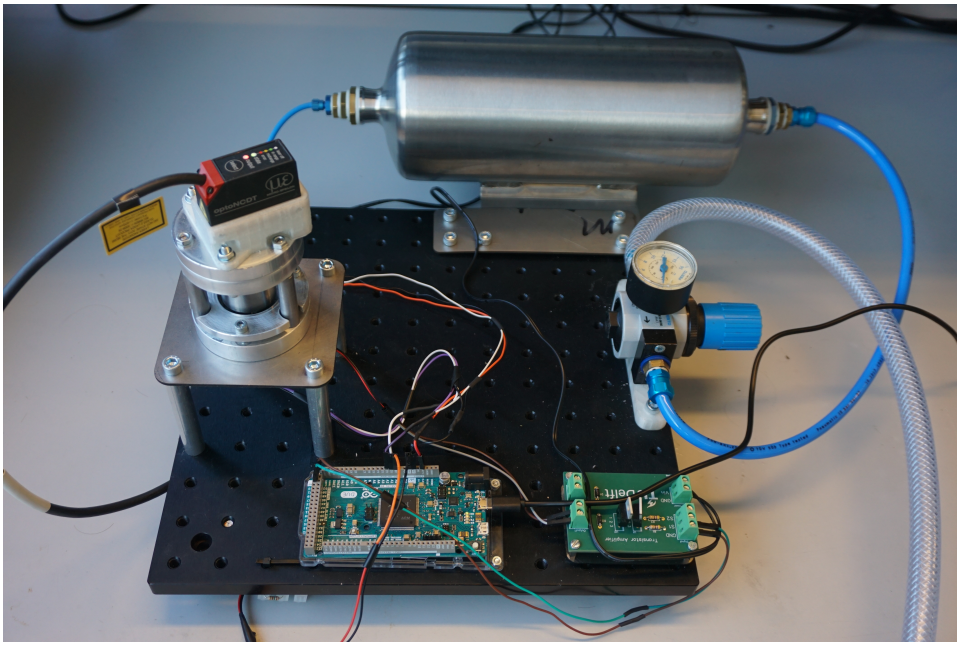

Figure 3.13: Photo of the total measurement setup. The compliant expansion chamber- exhaust valve assembly can be seen on the left. A pressurization system including a pressure regulator and air tank is visualised at the top of the figure. Control electronics including an Arduino Due microcontroller and MOSFET board can be seen on the bottom.

Since the aim of this measurement setup is to verify functioning of the passive exhaust valve and compliant expansion chamber, it is chosen to use compressed air as source of pressurization instead of a chemical fuel. A manual pressure regulator (0-5 bar) controls the pressure of the air inside the air tank (5L) depicted in Figure 3.13. A miniature solenoid valve (SMC S070, response time < 5 ms), located under the expansion chamber, supplies pressure pulses to the expansion chamber. The objective during solenoid valve selection was response time for fast opening and closing of the valve. The tank pressure as well as the expansion chamber pressure is monitored by two separate pressure sensors (Honeywell ABPDANN010BGAA5, 0-10 bar). Another design objective was to locate the solenoid valve as well as the pressure sensor as close as possible to the chamber itself with minimum dead flow path volume. This is done by incorporating a small inlet manifold directly under the expansion chamber to which the pressure sensor, solenoid valve and inlet coupling are connected. The solenoid valve is powered via a MOSFET board controlled by the Arduino Due microcontroller.

The compliant expansion chamber is identical to the bellow specified by Table 3.4. The top endplate of the bellow is bonded to a central shaft, where the steel load mass and load spring are connected to, as can be seen in Figure 3.14. The bottom endplate of the bellow is bonded to the exhaust spring. Both bonding steps are performed with an adhesive film (Toray EF8020) which is lasercut and thermally cured. Several bonding methods and bonding material thicknesses were considered a priori. The objective of the bonding method selection was maximum shear strength, but also temperature resistance (80) and low thermal deformation were required. Note that if a chemical fuel is used as pressurization source instead of the compressed air,

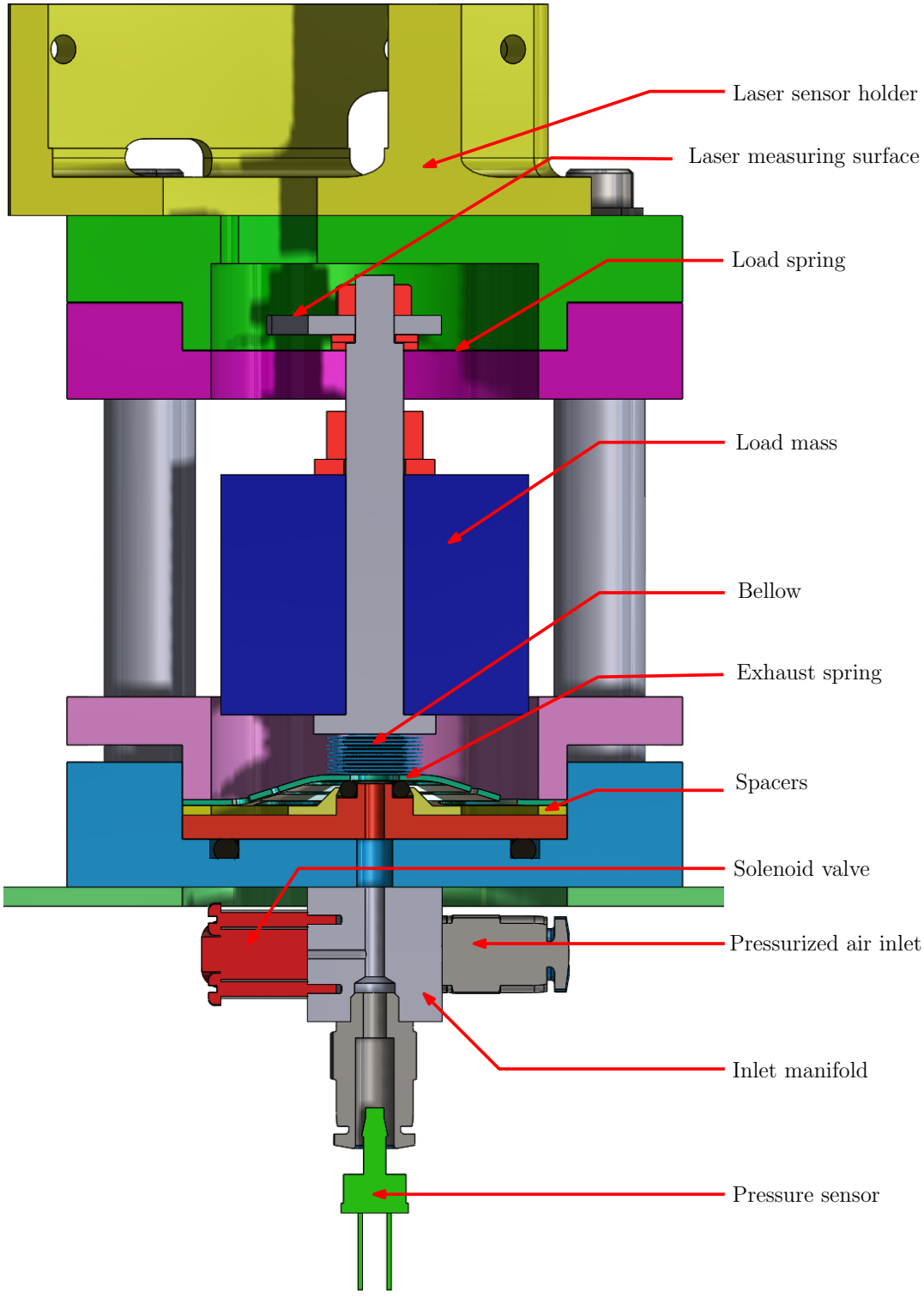

Figure 3.14: A section view of the CAD of the measurement setup

the bonding method is required to sustain much higher temperatures. The bonding methods were compared with shear strength tests, which are summarized in Appendix C.1 together with the curing cycles used. The exhaust spring and load spring are fabricated by lasercutting CrNi 1.4310 stainless steel sheet with the geometry specified in 3.2.5. The bottom side of the exhaust spring pushes on the o-ring, sealing the expansion chamber from the ambient air. The outer edge of the exhaust spring is clamped in a housing assembly. The

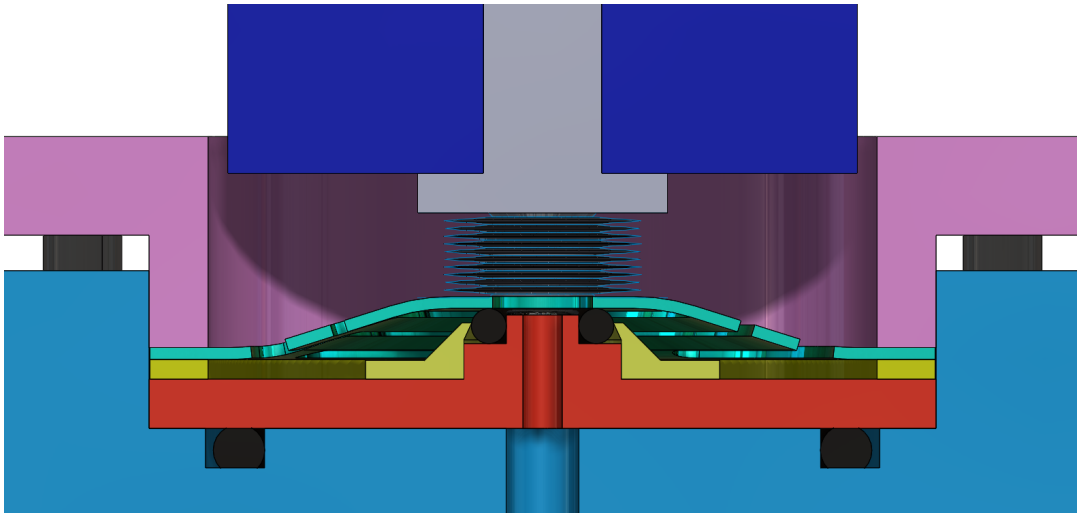

Figure 3.15: A detailed section view of the CAD of the compliant expansion chamber with exhaust valve integrated in the measurment setup.

pretension of the exhaust spring can be tuned by adding or removing 0.15 mm thick spacer rings. The load spring is also connected in the same manner to the housing assembly. It is chosen to break up housing assembly into several independent parts, making replacement easily possible if dimensions should be altered. The components of the housing assembly are fabricated by milling and lathing out of aluminum 6061 material. On top of the assembly, a laser triangulation sensor (micro-epsilon ILD-1401) is positioned in a laser holder to measure the position of the central shaft.

3.3.2. EXPERIMENT METHODOLOGY

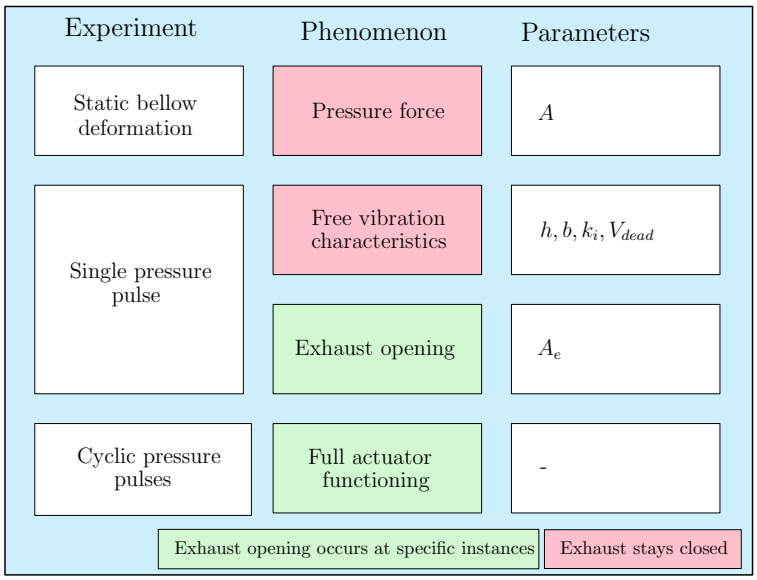

Figure 3.16: Experimental procedure, where the first column depicts the experiments conducted, the second column depicts the phenomena that are investigated during those experiments, and the last column denotes which parameters are determined by analysis of the experimental data.

The full thermodynamic model includes numerous variables, some of which can be directly calculated from setup geometry, but others remain relatively uncertain. To determine these design variables, an option would be to perform a full cyclic operation test of the actuator. The model variables could be determined by a minimization procedure where all variables are examined within their uncertainty range to identify which combination minimizes the model-measurements error. This is tried, however it is computationally intensive.

Moreover, this would not be insightful as it regards the model as a blackbox, where separate influence of each of the variables is difficult to understand and identify. A better option to gain insight into the system and the model discrepancies is to conduct separate experiments that can investigate system phenomena as pressure force, damping and exhaust opening movement independently. The main architecture of the experiments is depicted in Figure 3.16, that visualises which parameters are determined from the specific experiments.

First, a static bellow deformation experiment is conducted where the pressure-displacement dependency is measured while the exhaust valve is kept closed. With this experimental data, the magnitude of the pressure force and the effective thrust area A can be determined. Subsequently, single pulse experiments are performed where a single pressure pulse of constant duration is fed to the expansion chamber for different inlet pressures and pretension distances of the spacers. Damping performance, the inlet flow coefficient and dead volume can be determined from the free vibration characteristic (when the cavity remains closed). For the single pulse experiments where the exhaust valve does open, the exhaust valve functioning will be verified and exhaust opening criterion 3.20 will be investigated. Finally, cyclic pressure pulse experiments will be performed, where a new subsequent pressure pulse will be fed to the expansion chamber just before the piston reaches bottom position. This experimental evidence will be used to validate global actuator functioning.

3.3.3. STATIC BELLOW DEFORMATION EXPERIMENT

In the first experiment, a simple deformation measurement is performed. The pretension distance d_{pt} is set to 2 mm to prevent air leakage through the exhaust valve. Subsequently, excess pressure is relieved from the compliant expansion chamber by manually displacing the load mass and opening the exhaust valve, before letting it return to the resting state where the exhaust spring pushes against the o-ring. The solenoid is set to open position to equilibrate expansion chamber pressure with tank pressure. Afterwards, the pressure is gradually increased by adjusting the pressure regulator. Displacement and pressure are measured as a function of time. The quasi-static pressure-displacement data will be used to determine the experimental value of bellow thrust area A. An example of the pressure-displacement response is given in Figure 3.17.

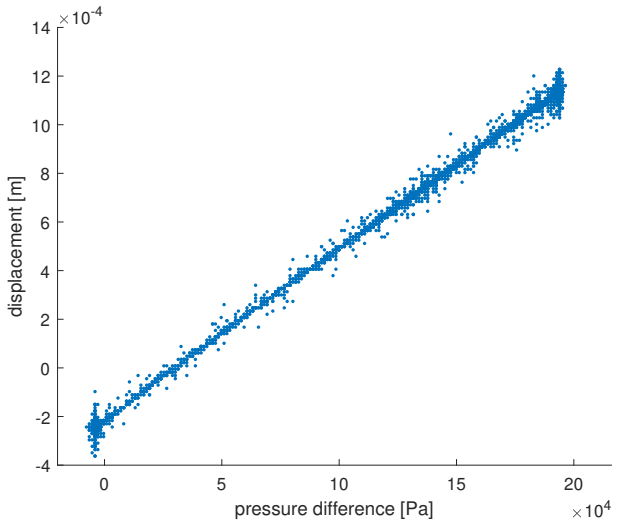

Figure 3.17: Displacement-pressure relation during a procedure where chamber pressure is gradually increased.

3.3.4. SINGLE PULSE EXPERIMENTS

To investigate the exhaust opening performance, a single pressure pulse is fed to the compliant expansion chamber in the second experiment. The main goal of this experiment is to measure at which bellow deformation the exhaust valve begins to open and to correlate this with opening criterion 3.20. Also, if the exhaust valves remain closed, the free vibration harmonics of the sealed cavity are used to determine V_{dead}, k_i, h, b

The procedure that has been carried out to conduct the single pulse experiment is explained now. First, the pretension distance d_{pt} is set by placing the correct amount of spacers in the assembly. Subsequently, excess

pressure is relieved from the compliant expansion chamber by manually displacing the load mass and opening the exhaust valve, before letting it return to the resting state where the exhaust spring pushes against the o-ring. Subsequently, a block signal of duration t_{open} is sent to the solenoid to provide a short pressure pulse to the expansion chamber. The displacement response x and pressure response p are measured as a function of time t. The tank pressure p_i is also measured shortly before the pressure pulse is applied.

This sequence is repeated four times for each actuator setting (t_{open}, p_i, d_{pt}), after which the variables p_i and d_{pt} are swept through the ranges depicted in table 3.3. Opening time t_{open} is kept constant. Note that the presence of a significant gravity force makes proper closing of the exhaust possible possible for negative values of d_{pt}.

Setting variable	Minimum value	Maximum value	Amount of intermediate values
p_i	0.64 bar	2.58 bar	4
d_{pt}	−0.62 mm	0.58 mm	4
t_{open}	6 ms	-	1

Table 3.3: Sweeping ranges of setting variables

INITIAL OBSERVATIONS OF DEVICE FUNCTIONING

Based on the observations of the measured pressure and displacement response, the different single pulse experiments performed can be categorized into three different categories:

1. Opening of the exhaust valve, full gas release
2. Exhaust valve remains closed, no gas release
3. Opening of the exhaust valve, partial gas release

The typical measured pressure response and typical measured displacement response of the different categories are depicted in Figure 3.18 and 3.19 respectively.

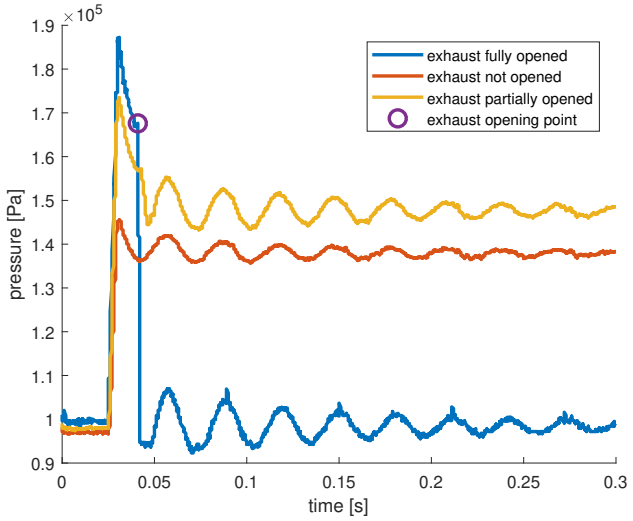

Figure 3.18: Comparison of the measured pressure responses of the different single pulse experiment categories

The following can be observed from the pressure and displacement response from the first category. Approximately 3 ms after the solenoid receives a high input signal, the pressure rises in the expansion chamber to its maximum pressure until the solenoid valve closes. Subsequently, the piston displaces upwards and pressure decreases slightly due to volumetric expansion. Afterwards, the sudden decrease of pressure to ambient pressure indicates that the exhaust valve has been opened. The duration and opening displacement appear to be sufficient for full pressure relief. After the piston reaches maximum displacement and returns downwards, a threshold displacement is reached where the exhaust valve closes again. Afterwards, the piston shows underdamped vibration while the bellow is sealed, thus compressing and decompressing the gas in the chamber.

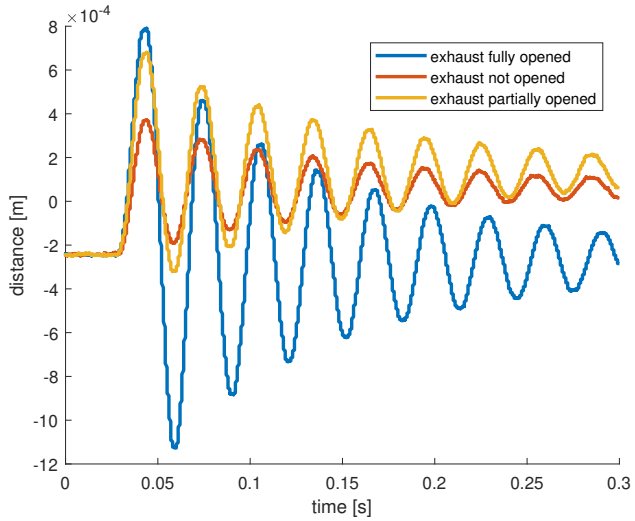

Figure 3.19: Comparison of the measured displacement responses of the different single pulse experiment categories

From the measured pressure and displacement response of the second category, it can be observed that after the initial pressure rise, the mean pressure remains high. The displacement amplitude is lower, apparently not sufficient for the bellow to accumulate enough axial force to pull open the exhaust valve. The displacement response shows subsequent underdamped vibration. The pressure response follows since the gas is being harmonically compressed and decompressed, but now at a higher mean value.
From the measured pressure and displacement response of the third category, it can be noticed that the pressure relief event has started, but that does not continue until ambient pressure. The displacement amplitude is sufficient to open the exhaust valve, but this exhaust valve opening duration and gap height x_2 are inadequate for total gas release.
The three different regimes observed in aforementioned single pulse experiments show that the exhaust valve operates successfully as long as sufficient displacement amplitude is reached to pull open the exhaust valve. Pretension distance has to be set such that exhaust event is triggered (first category), favourably near top piston position to maximize the length of the expansion stroke. However, exhaust opening should be triggered early enough to prevent insufficient gas removal, as is observed in the second category. All things considered, the aforementioned observations support successful functioning of the device as is explained in Section 2.7.1.

3.3.5. CYCLIC PULSE EXPERIMENTS

In the subsequent experiment, the continuous operation of the actuator is demonstrated. In contrast to the single pulse experiments, now multiple sequential pressure pulses are fed to the expansion chamber. The procedure of this experiment is identical to the single pressure pulse experiment up to and including the initiating pressure pulse of t_{open}. Now a new pressurization event of lower duration $t_{open,2}$ is triggered once displacement value reaches threshold $x_{cp} = -0.8mm$ while having negative velocity. Since little damping is present in the system, $t_{open,2}$ has to be chosen precisely to prevent the resonating system from accumulating too much energy. Opening durations t_{open} and t_{open2} are given in Table 3.4 along with the sweeping values of the other setting variables p_i and d_{pt}. Until the final fourth pulse, the displacement and pressure are measured as a function of time. Longer cyclic operation was possible to achieve but not performed, because the current setup does not allow measurement of longer duration due limited storage capacity of the Arduino. Also, current experiment delivered enough information, and unnecessary operation of the fragile bellow assembly was unfavourable.

INITIAL INVESTIGATIONS OF DEVICE FUNCTIONING

Figure 3.20 shows the measurement data of a cyclic pulse experiment. What can be observed is successful triggering of the new pressurization pulses and repeated opening of the exhaust valve. The general shape of pressure response within all cycles can be characterized by the following events: instantaneous pressure rise, slow pressure decrease due to volumetric expansion and instantaneous pressure relief. This supports

Setting variable	Minimum value	Maximum value	Amount of intermediate values
p_i	0.88 bar	2.12 bar	6
d_{pt}	-0.02 mm	-	1
t_{open}	6 ms	-	1
$t_{open,2}$	3 ms	-	1

Table 3.4: Sweeping ranges of setting variables in cyclic pulse experiments

successful cyclic operation of the proposed compliant expansion chamber with passive exhaust valve.

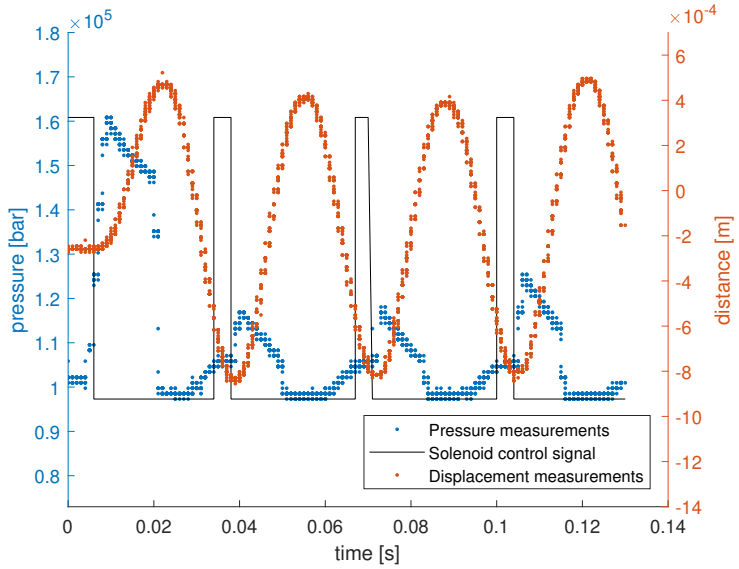

Figure 3.20: Pressure response p and displacement response x for cyclic pressure pulses. The solenoid control signal is visualised by the black line. Setting variables used: $p_i = 1.32$ bar, $d_{pt} = -0.02$ mm, $t_{open,1} = 6$ ms, $t_{open,2} = 3$ ms

Parameter	Theoretical value	Experimental value	Relative difference
A	$5.01 * 10^{-5} m^2$	$4.08 * 10^{-5} m^2$	-19%
h	-	$0 W/K$	-
b	-	$2.67 Ns/m$	-
V_{dead}	$2.3 * 10^{-7} m^3$	$2.47 * 10^{-7} m^3$	+7.4%
k_i	-	$3.34 * 10^{-10} kg * Pa/s$	-
A_e	$5.67 * 10^{-5} m^2$	$4.61 * 10^{-5} m^2$	-19%

Table 3.5: Theoretical and experimental values for parameters that are determined in this section.

3.4. PARAMETER DETERMINATION

In this section, parameters A, h, b, k_i, V_{dead} are determined by analysing the different experiments. This section follows the same structure as depicted in Figure 3.16, where it is visualised which experiments are used for the determination of certain variables. An overview of the experimentally determined parameters is given in Table 3.5, together with the theoretical values.

3.4.1. PRESSURE FORCE

The pressure force is a key model relation, since it determines the excitation of the piston each cycle and thereby power output. The pressure force is proportionally dependent on effective bellow pressure area A, hence this parameter will be determined in this section. The mathematical derivation in Appendix A.3 offers a theoretical estimate of bellow pressure area A based on geometrical parameters of the bellow. The static bellow deformation experiment is used to determine the experimental value of A, and thereby validate the geometrical estimate. In the static deformation experiment, piston displacement x can be described by Equation 3.33, assuming static equilibrium of the piston mass.

$$x = \frac{A}{s} p - \frac{mg}{s} \tag{3.33}$$

From the gradual deformation experiment, coefficient $c_1 = \frac{A}{s}$ is experimentally determined by least-squares fitting through the x, p measurement data. From stiffness s and the fit coefficient c_1, the experimental value of A is calculated and given in Table 3.5. This value for A is 19% smaller than calculated by 3.14. The discrepancy will be explained in the discussion.

3.4.2. FREE VIBRATION CHARACTERISTICS OF CLOSED BELLOW

In this section, the free vibration characteristics are inspected. Only single pressure pulse experiments from category two, where no exhaust event occurred, were used to remove the influence of exhaust flow variables from the equation, such that parameters V_0, k_i, b, h can be separately determined by a minimization procedure.

First, the heat transfer through the chamber wall is investigated. During the high pressure inlet pulse, a temperature rise is induced due to compressive heating. A significant heat transfer between expansion chamber and environment will lead to a gradual trend of decreasing temperature and thereby a gradual decrease in mean pressure. This gradual trend of decreasing mean pressure is visualised in Figure 3.21. From Figure 3.18 and all other single pulse experiments in the second category, it is observed that the pressure response is resonating around a mean value, but this mean value does not decrease significantly over time. Therefore it is chosen to neglect the influence of heat transfer in the model and heat transfer coefficient h is set to zero. This decision will be reconsidered in the discussion.

Subsequently, damping constant b is determined from the displacement response. To obtain b, the upper bounding equation of a simple damped harmonic oscillator (Eq. 3.34) is fitted by a minimization procedure, described in Appendix A.4. From obtained decay rate β, the damping coefficient b is calculated by Equation 3.35, and the result is depicted in Table 3.5.

$$x_{ub} = \alpha e^{-\beta t} + \gamma \tag{3.34}$$

$$b = 2m\beta \tag{3.35}$$

Now b and h are determined, the last parameters that will be determined in this section are dead volume

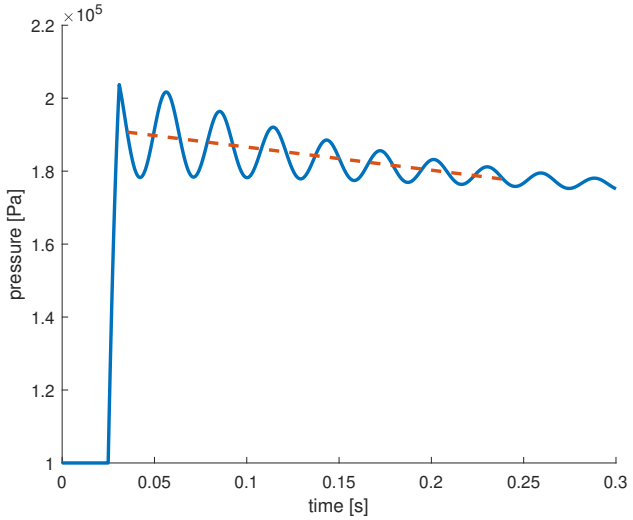

Figure 3.21: Trend of decreasing mean pressure due to heat loss

V_{dead} and inlet flow coefficient k_i. These variables have great influence on the pressure and displacement response in terms of the amplitude, equilibrium value as well as eigenfrequency, while their influence is cross-linked and therefore difficult to identify separately. This can be partly attributed to the fact that both V_{dead} and k_i influence the Helmholtz stiffness of the chamber, which describes the compressive stiffness of the gas body. Hence, variables V_{dead} and k_i are simultaneously determined by solving the minimization problem described in Appendix A.5. The solution is depicted in Table 3.5.

3.4.3. EXHAUST OPENING CRITERION

In this section, it is investigated how the exhaust opening criterion from Equation 3.20 compares to measured opening displacement x_{open}, and the experimental value of A_e is determined. To do so, the opening displacement x_{open} and opening pressure Δp_{open} was numerically determined for all single pulse experiments of category one, where the exhaust event was triggered. This opening point is indicated by the purple circle in Figure 3.18. Figure 3.22 depicts the experimentally obtained opening points x_{open} as a function of Δp_{open} for different d_{pt}. In this figure, the exhaust opening criterion from Equation 3.20 is also visualised for different d_{pt}, assuming the theoretical estimate for A_e.

What can be observed is that the opening displacement measurement data x_{open} are generally lower than estimated by the model, especially for higher d_{pt}. However, the theoretical estimate for A_e is relatively uncertain, which is of great influence on x_o by altering the slope of the x_o/p_o relation. The experimental value of A_e is determined by least-squares fitting the modelled lines of 3.20 to the measurement opening values. The reason that only A_e is fitted and other variables d_{pt} and $F_e(d_{pt})$ are held constant, is that the relative uncertainty of d_{pt} and $F_e(d_{pt})$ is estimated to be negligible compared to the relative uncertainty of A_e. The solution for A_e is given in Table 3.5. Figure 3.23 visualises how the exhaust opening criterion 3.20 for the experimental A_e compares to the measured values. The discrepancies will be explained in the discussion.

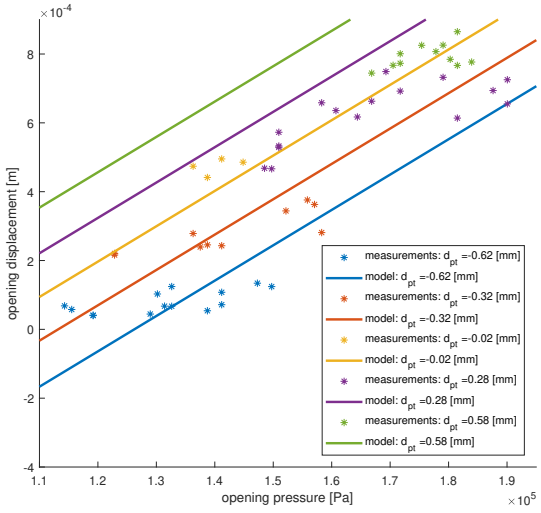

Figure 3.22: Opening displacement x_0 as a function of Δp for theoretical A_e for different d_{pt}. Model vs experimental data comparison.

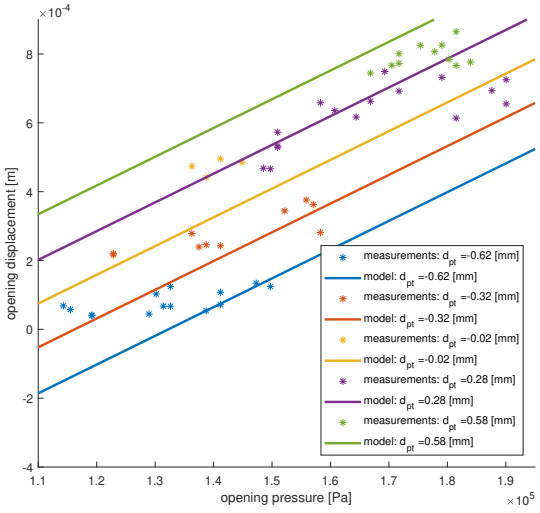

Figure 3.23: Opening displacement x_0 as a function of Δp for experimental A_e for different d_{pt}. Model vs experimental data comparison.

3.5. RESULTS AND DISCUSSION

In the previous section, functioning of the proposed exhaust valve and chamber concept has been successfully demonstrated and system behaviour was characterized. Still, many aspects of the novel compliant expansion chamber and integrated exhaust valve require further study. The discrepancies between theoretical and experimental values of the obtained parameters should be understood. Therefore, these discrepancies are discussed in the half of this section. Secondly, the obtained experimental parameters can be used as input parameters for the full actuator model assuming cyclic inlet pulses. The resulting model response is inspected and compared to the experimental data in the second half of the discussion.

3.5.1. PRESSURE FORCE

The pressure force is was initially overestimated, if one assumes the theoretical value of A that is calculated by Equation 3.14. The measured A is 19% lower than the theoretical value. This discrepancy may be explained due to uncertain outer diameter D_o and wavy bellow corrugations. Outer diameter D_o was initially determined by measuring the bellow exterior. However, the relevant outer diameter is actually the inside diameter of the welding connection between two subsequent corrugations, which is lower, thus reducing the actual A. Moreover, the derivation for theoretical A in Appendix A.3 assumes triangular bellow corrugations. These corrugations are in fact wavy, influencing the force profile along the bellow wall and thereby the equivalent A.

3.5.2. FREE VIBRATION CHARACTERISTICS

The experimental values for A, h, b, V_{dead} and k_i are used as input variables for the model and the model pretension d_{pt} is set sufficiently high to prevent exhaust opening. The resulting modelled pressure and displacement response is visualised in Figure 3.24. Figure 3.24 also visualises the measurement displacement pressure for comparison. The following discrepancies can be identified.

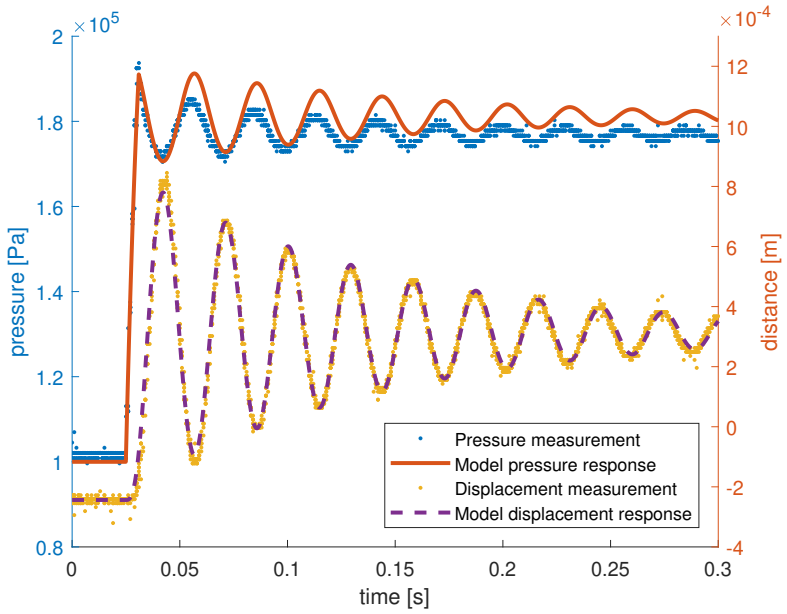

Figure 3.24: Model vs. measurement for a typical single pulse experiment. Measurement setting variables used: $p_i = 1.55$ bar, $d_{pt} = 0.58$ mm, $t_{open} = 6$ ms

1. The eigenfrequency of harmonic behaviour of the model response seems very well correlated with the measured values (within 1% relative difference), both in the displacement response and pressure response. This makes it likely that both stiffness s and the Helmholtz stiffness (dependent on V_{dead} and k_i) modelled accurately.

2. Inspecting Figure 3.24, it appears that the model pressure response does not match the measured values, since the mean pressure value in the free vibration section is approximately 5% higher than measured. Modelling less air compression, thus increasing V_{dead} or decreasing k_i, would decrease the

pressure equilibrium value, but also the displacement response, and there is no combination possible that mitigates both errors.
Be that as it may, a significant change in the pressure-displacement relation could be induced by increasing the modelled heat loss through the bellow wall. Hence, the earlier assumption of no heat loss is reconsidered. The earlier reasoning, that heat loss can only be significant if a gradually decreasing trend of mean pressure is observed, is debatable or even invalid. If heat loss is high, the bellow gas temperature would decrease to ambient temperature within a fraction of a cycle, meaning that associated pressure decrease due to heat loss will also happen within a cycle. If ambient temperature is reached, no further heat loss will take place and the mean pressure will also stay constant for the rest of the vibration response. This scenario is depicted in Figure 3.25 and 3.26 respectively, where the temperature and pressure response of a significant heat loss coefficient of 0.1W/K is compared against the temperature and pressure response of a heat loss coefficients of 0.004W/K and 0W/K.

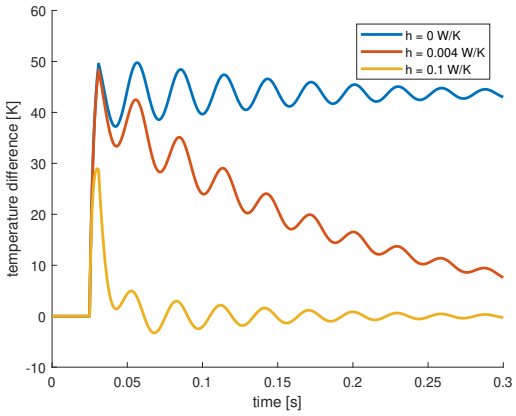

Figure 3.25: Influence of different heat loss coefficients on the temperature response of the single pulse experiment without exhaust opening

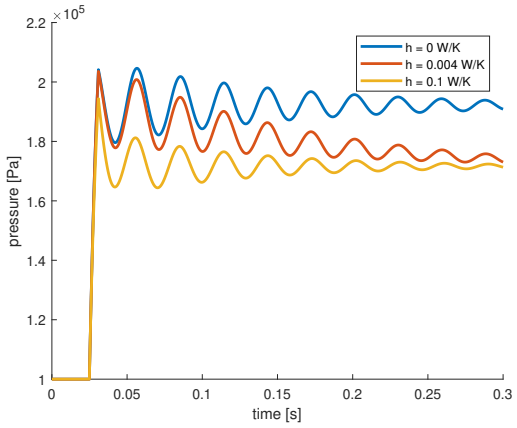

Figure 3.26: Influence of different heat loss coefficients on the pressure response of the single pulse experiment without exhaust opening

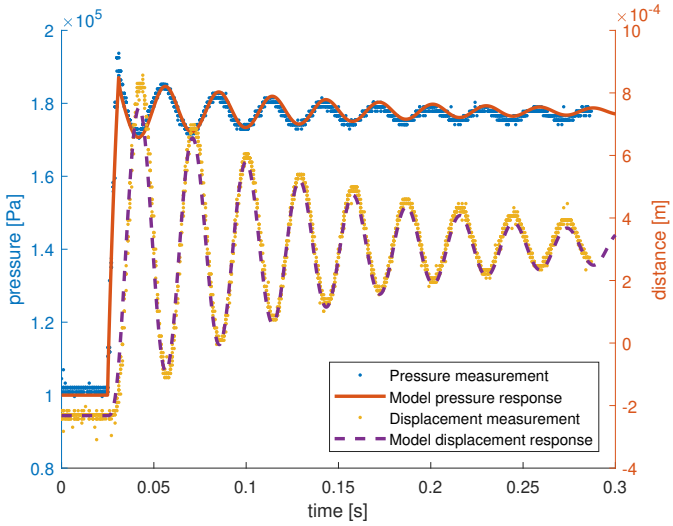

Figure 3.27: Model vs. measurement for a typical single pulse experiment. Measurement setting variables used: $p_i = 1.55$ bar, $d_{pt} = 0.58$ mm, $t_{open} = 6$ ms. Model parameteres used:$h = 0.4$W/K, $V_{dead} = 2.7 * 10^{-7}\, m^3$, $k_i = 4.64 * 10^{-10}\, \frac{kg}{Pas}$

k_i and V_{dead} are determined again by the procedure described in Appendix A.5, now for a significant heat transfer coefficient $h = 0.4$ W/K. A comparison with the single pulse experiment measurement values is depicted in Figure 3.27. What can be noted is that the pressure discrepancy is much lower, indicating that significant heat loss is probable. This can also be expected, since current expansion

chamber is thin-walled and has much higher area-to-volume than conventional engines. For this bellow, results indicate that the pressure generation is only a direct consequence of the additional gas mass in the chamber under ambient conditions, since the effect of the associated temperature increase is directly mitigated due to heat loss. Nonetheless, the actual heat loss coefficient h is impossible to determine from conducted experiments, since the difference between a heat loss coefficient h of 0.1 W/K and a much higher h cannot be deduced from the pressure or displacement measurements. What can be deduced is a minimal value for h, which is found to be approximately 0.1 W/K. Further research has to be conducted to examine the heat transport through the bellow wall and determine heat coefficient h more accurately.

3. Examination of the typical damping behaviour in Figure A.3, it can be observed that the damping appears to gradually become less strong as time passes. Firstly, this could be attributed to significant heat loss, leading to additional decay of displacement amplitude when temperature difference is high. Secondly, the damping force could scale quadratic with velocity instead of the modelled linear dependency, which is actually more logical for the aerodynamic damping present. This results in stronger damping for higher amplitudes.
   Given the displacement decay rate β calculated in Appendix A.4, the associated Q-factor of the system is approximately 12. This can be advantageous for actuator performance, since misfires or fluctuations in aerodynamic loading will not lead to sudden actuator stall.

4. A small phase difference can be observed between the measured harmonic pressure and the measured harmonic displacement, where the measured pressure signal is advanced relative to the displacement signal. This is unexpected, since the bellow cavity pressure follows the compression motion of the chamber, and this cavity pressure wave still has to be transported to the pressure sensor via a small orifice, which would mean delayed pressure measurement. However, the laser triangulation sensor contains internal processing circuitry that might require significant processing time before output, which explains the phase delay of the displacement measurement signal.

3.5.3. EXHAUST OPENING CRITERION

The discrepancies between modelled opening displacement x_o and measured opening displacement could have several reasons. For clarity, the exhaust opening criterion is given again in Equation 3.36.

$$x_o = \frac{F_e(d_{pt})}{s_b} + \frac{A_e}{s_b}\Delta p \tag{3.36}$$

If the theoretical A_e is assumed, it appears that the modelled x_o is significantly higher estimated than measured for higher pretension values, as can be seen in Figure 3.28. It could be that the spacer placement for the pretension of 0.28mm and 0.58mm was done incorrectly. Small contaminations between the 0.15mm spacer rings or misalignments will significantly reduce pretension and thereby measured opening displacement.

The error could also be completely attributed to incorrect theoretical A_e, then it is assumed that the stiffness term of Equation 3.36 is entirely correct. The fitting procedure described in previous section gives an experimental A_e that is 19% lower. The underlying source of the variation between theoretical and experimental A_e is investigated in a more detailed manner. Depicted in Figure 3.30 in purple, the region between the bellow connection root (indicated with a green circle) and the o-ring sealing line is regarded as the area A_e of the exhaust spring were combustion pressure acts on (Equation 3.19). A smaller experimental D_o than modelled is a probable reason for the discrepancy, since as explained earlier, D_o is determined by the diameter of the welding connection between two subsequent corrugations, which is lower than used exterior D_o, thus reducing the actual A_e. Both the theoretical A_e and experimental A_e are positive, meaning that the pressure force acting on the effective surface A_e resists the exhaust opening movement. Ideally, for a robust exhaust valve, A_e should be close to zero to eliminate the influence of pressure from the equation, such that opening displacement x_o is merely a function of component stiffnesses and pretension distances.

Nonetheless, inspecting Figure 3.29, the trend of the experimental x_{open}, p_{open} values show still a lower slope than modelled by Equation 3.36. This suggests that only varying modelled A_e will not capture the relation between x_o and Δp. Figure 3.29 appears to suggest that the pressure term of Equation 3.36 should be reduced and stiffness term of equation should be increased, in order to lower the slope of the line. However, increasing the stiffness term will also increase the vertical spacing between the lines of different pretension

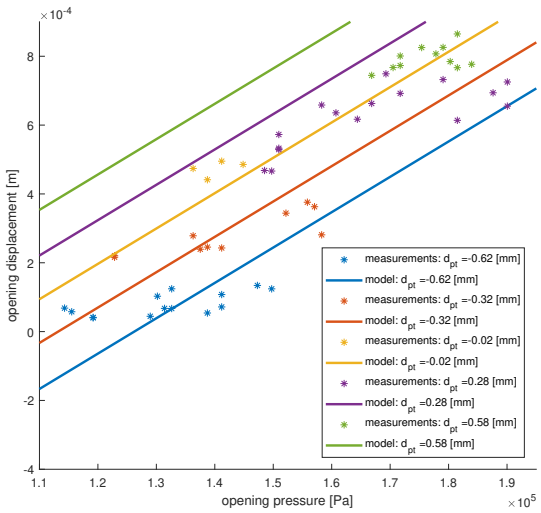

Figure 3.28: Opening displacement x_0 as a function of Δp for theoretical A_e for different d_{pt}. Model vs experimental data comparison.

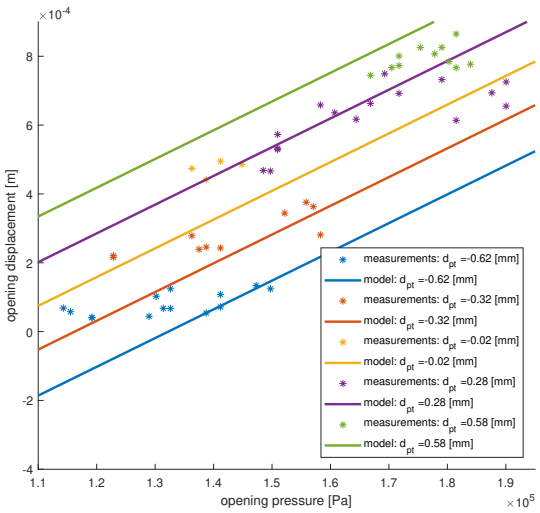

Figure 3.29: Opening displacement x_0 as a function of Δp for experimental A_e for different d_{pt}. Model vs experimental data comparison.

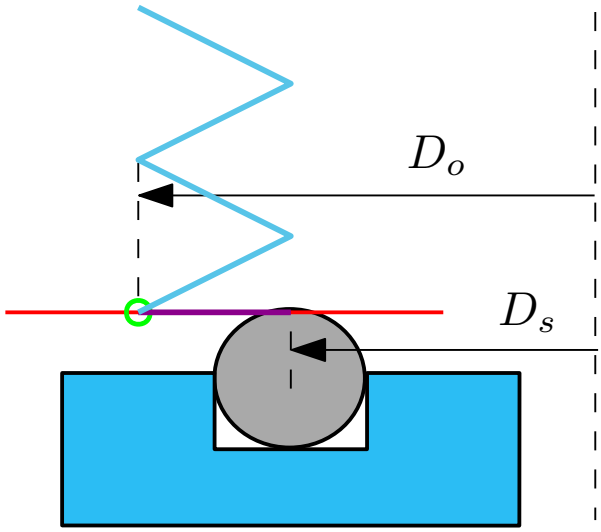

Figure 3.30: Effective pressure area A_e of exhaust spring, denoted in purple

values, and will not lead to smaller overall discrepancy. A significant increase in the stiffness term also means a significant error in exhaust spring stiffness, actual pretension or bellow stiffness. There is no clear reason to suspect any major error in both the force-deflection curve of the exhaust spring or the bellow stiffness. The pretension distance could be lower than estimated due to incorrect spacer placement, but higher than estimated is not very likely. The underlying source of the discrepancy in the exhaust opening criterion is not completely understood and remains an interesting scope for further study.

3.5.4. FULL DYNAMIC ACTUATOR FUNCTIONING WITH CYCLIC INLET PULSES

Finally, using the previously determined experimental parameters, the full actuator response is modelled using cyclic inlet pressure pulses. The model does not allow implementation of the displacement dependent inlet pulse triggering $k_i(x, \dot{x}, t)$ of duration t_{open2}. Therefore it is implemented that inlet flow factor k_i is a block signal function set to the same opening and closing times as recorded in the solenoid control signal. The following modelling steps are investigated:

1. Using the raw solenoid signal to switch modelled inlet flow on or off does not lead to an accurate inlet

pulse timing in the model. Timing discrepancies of 5 ms are observed. This can be partially attributed to the inertia of the solenoid mechanism, which results in significant opening delay and closing delay times. Also, the actual solenoid control signal durations t_{open} and $t_{open,2}$ can be varying with ±0.5 ms. This explains the varying peak pressure between the different cycles. Moreover, they are measured with an inaccuracy of ±0.5 ms. Accounting for the timing discrepancies by implementing an opening and closing delay leads to reduction of the timing error to lower than 1 ms.

2. If it is assumed that stiffness s stays constant, and does not decrease during exhaust opening, an eigenfrequency mismatch of 15% can be observed between the modelled and measured displacement response. If a variable stiffness is captured as in Equation 3.22, meaning that stiffness is reduced at the instance the exhaust opens and becomes configured in a serial arrangement with the exhaust spring, the eigenfrequency mismatch is reduced to within 1%. It is therefore recommended that the variable stiffness effect should be captured.

The resulting modelled pressure and displacement response are depicted in Figure 3.31, including the measured pressure and displacement for comparison. The following can be noticed:

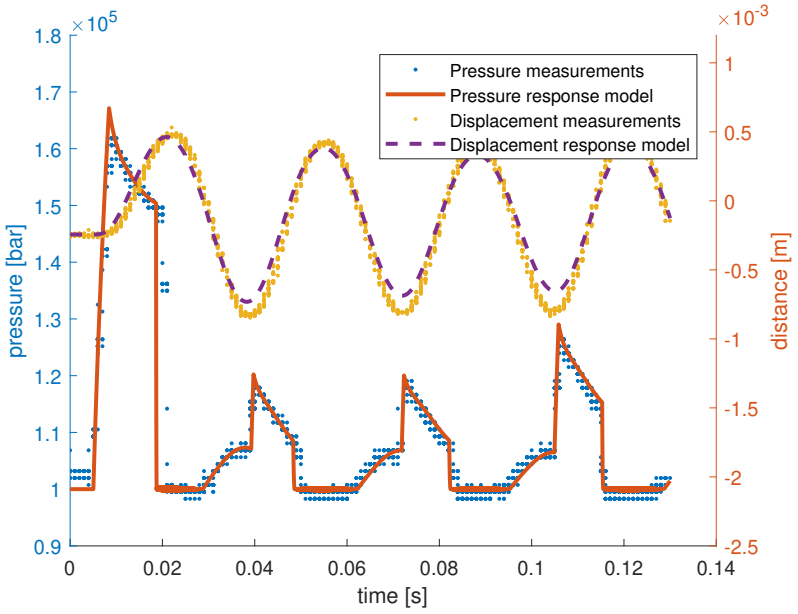

Figure 3.31: Cyclic pressure pulse response comparison. Inlet mass flow is switched using solenoid control signal, post-processed opening and closing delays, and variable s_b. Measurement setting used: $p_i = 1.32$ bar, $d_{pt} = -0.02$ mm, $t_{open,1} = 6$ ms, $t_{open,2} = 3$ ms. Model parameters: $h = 0.4$W/K, $V_{dead} = 2.7 * 10^{-7} m^3$, $k_i = 4.64 * 10^{-10} \frac{kg}{Pas}$

1. From comparing the model and measurements, the magnitude of the pressure response and eigenfrequency match well, and no clear discrepancies can be observed. Also, the modelled pressure response shows the same characteristic shape every cycle as measured, which is characterized by the following events: gradual pressure rise due to bellow volumetric compression, instantaneous pressure increase due to inlet pressure pulse, gradual pressure decrease due to volumetric expansion, instantaneous pressure drop until ambient pressure due to exhaust opening.

2. Inspecting the pressure response, it can be observed that the model estimates that the exhaust opens 1-2 ms earlier than measured in the first two cycles. This can be expected from the modelled displacement, since the modelled displacement amplitude is also higher than measured at the moment of exhaust opening. Additionally, the inaccuracies in the modelling of the exhaust opening criterion from previous section will also result in delayed or advanced exhaust opening timing.

3. The minimum displacement amplitude of the model is approximately 0.1mm higher than measured. This could have multiple reasons. It could be the case that damping coefficient b is modelled too high. Also, it suggests decreased bellow stiffness at low displacement values. It is not expected that the non-linearity of the load-displacement curve of the bellow is the source of this discrepancy, because this

curve likely shows geometric stiffening. However, it could be attributed to the O-ring compression stiffness, which is modelled to be rigid. Once the exhaust spring touches the O-ring during downward stroke, it becomes configured in serial arrangement with the bellow, which reduces the effective bellow stiffness. It is difficult to identify what the dominant reason is for the displacement discrepancy.

3.6. CONCLUSION

The compliant expansion chamber with an integrated passive exhaust valve is designed, built and successfully validated in a measurement setup. Experimental evidence proves the exhaust valve is capable of releasing the gas within one opening stroke. By setting the pretension of the exhaust spring, the exhaust opening point can be regulated to a desired bellow deformation amplitude.

In the fabrication procedure, it is for this design recommended to connect the bellow endplate with the exhaust spring by an adhesive film cured in an oven, which ensures a sealed, rigid connection. However, this method will not be suitable if high gas temperatures are reached.

The constructed model allows us to calculate outputs such as displacement response, pressure response, temperature response and power output, based on bellow geometry and component stiffnesses.

The model does capture the displacement dependent behaviour of exhaust opening and closing. However, further study should be conducted to describe the exhaust opening point more accurately, since it is not fully understood yet how the exhaust opening is dependent on bellow deformation and internal pressure of the bellow.

Model-measurement comparison of the pressure and displacement response indicates that heat loss through the bellow wall should be regarded as significant, even for this relatively low temperature range. It is not possible to determine the exact heat loss coefficient from conducted experiments, and this remains a relevant topic for further research.

The effect of varying stiffness during exhaust opening should be captured by the model, otherwise the eigenfrequency of the predicted displacement harmonics does not match with the actual displacement response.

If all observed discrepancies are considered, it is expected that the model predicts the pressure response, displacement response and power output within 10% accuracy. To that end, the proposed model is regarded as a valuable tool for development of future designs.

4

AN ELECTROWETTING-BASED FUEL INJECTION DEVICE

4.1. INTRODUCTION

Although the expansion chamber and exhaust valve are designed, built and validated, the chemical actuator cannot function independently yet without a chemical pressurization source and suitable injection module. As proposed in Chapter 2, we pursue pressurization by catalytic decomposition of hydrogen peroxide. A droplet of hydrogen peroxide fuel is dispensed from a reservoir, accelerated over an electrode array using electrowetting-on-dielectric (EWOD) and directed towards a catalyst for decomposition upon contact. A schematic of the proposed design is given again in Figure 4.1, to visualise how the injection module can be integrated into the expansion chamber. The general architecture of the electrode array is depicted in Figure 4.2. Note that multiple injection modules can be situated on the substrate (depicted in purple), pointing from the center radially outwards towards the catalyst ring.

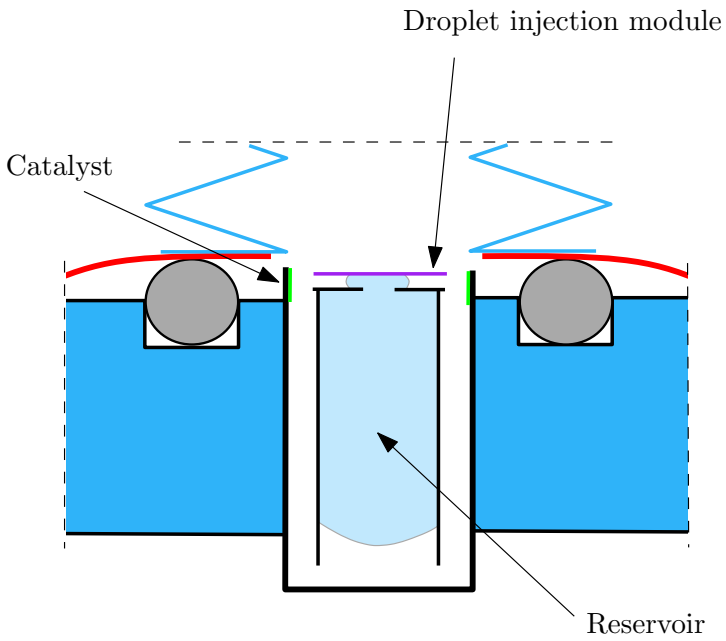

Figure 4.1: Schematic of a single injection module

The goal of this chapter is threefold. First, it aims to enrich the previously developed actuator model with a submodel that predicts the gas and heat generation of the catalysis reaction, such that the required hydrogen peroxide volume per cycle can be estimated. Secondly, it intends to develop an analytic model that predicts the droplet trajectory from reservoir to catalyst as a function of time. Thirdly, it is tried to validate the modelled droplet trajectory in an experimental setup. The outline of this chapter is visualised in 4.3.

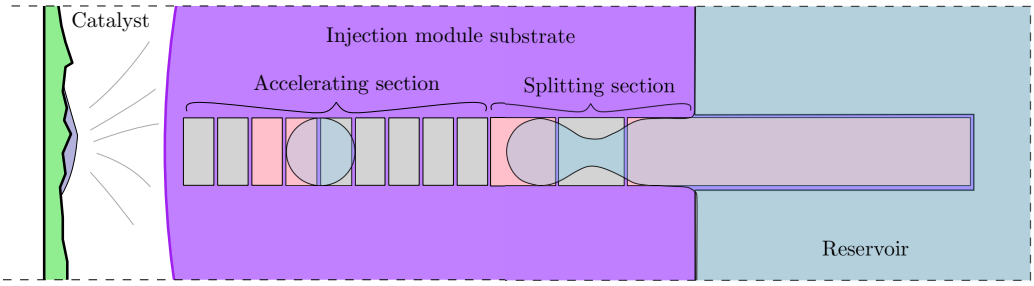

Figure 4.2: Schematic of a single injection module (top view). Actuated electrodes are visualised in pink.

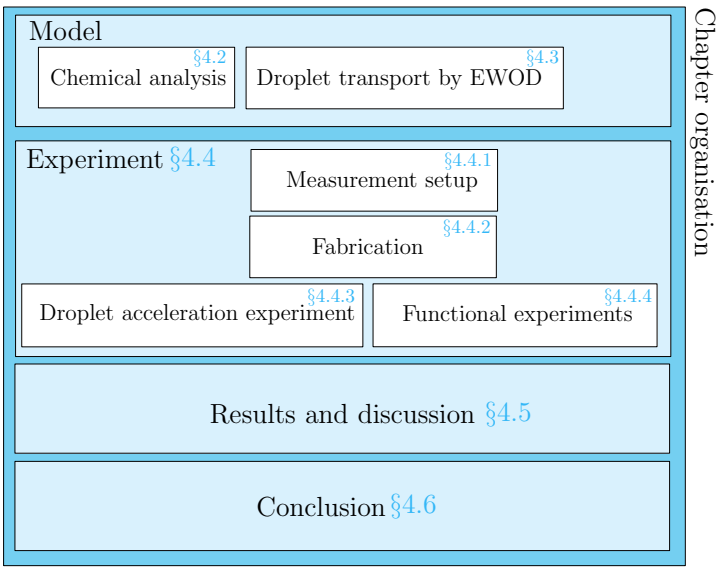

Figure 4.3: Chapter organisation

4.2. CHEMICAL ANALYSIS

4.2.1. INTRODUCTION CHEMICAL ANALYSIS

In this section, the chemical reaction of hydrogen peroxide decomposition is studied. The goal of this analysis is to determine how much gas and heat is generated per unit of fuel volume. The gas and heat generation will be implemented in the actuator model from the previous chapter, to be able to conclude which amount of fuel per cycle should be ejected to achieve desired actuator performance.

4.2.2. CHEMICAL REACTION

In order to predict pressure generation of the hydrogen peroxide decomposition reaction, it is important to investigate the chemical reaction thoroughly. The catalytic decomposition of hydrogen peroxide with Manganese Oxide catalyst is described by the following reaction [47].

$$H_2O_2 \xrightarrow{MnO_2} H_2O + \frac{1}{2}O_2$$

The chemical reaction leads to gas generation that directly increases the amount of gas in the chamber and thereby leads to a pressure increase. Also, the heat generated from this exothermic reaction leads to heating of the reaction products as well as heating of the water present in the hydrogen peroxide solution, resulting in full evaporation or partial evaporation depending on the hydrogen peroxide mass fraction c used. Both will be investigated further in the subsequent two sections.

4.2.3. GAS GENERATION

The aim of this section is to relate the mass of the decomposition gas products to the reactant volume of hydrogen peroxide. Eventually, an incoming mass flow function has to be constructed to simulate the gas being generated from the hydrogen peroxide fuel. As a first step, the hydrogen peroxide mass and the water mass in the fuel solution can be calculated by Equation 4.1 and 4.2 respectively, where c indicates the mass fraction of hydrogen peroxide in the solution. The molar quantity of hydrogen peroxide can be calculated by dividing the mass by the molar mass as in Equation 4.3.

$$m_{H_2O_2} = \frac{c}{\frac{c}{\rho_{H_2O_2}} + \frac{1-c}{\rho_{H_2O}}} V_f \tag{4.1}$$

$$m_{r,H_2O} = \frac{1-c}{\frac{c}{\rho_{H_2O_2}} + \frac{1-c}{\rho_{H_2O}}} V_f \tag{4.2}$$

$$n_{H_2O_2} = \frac{m_{H_2O_2}}{M_{H_2O_2}} \tag{4.3}$$

By inspecting the relative molar quantities of the reactant and products in the reaction, the molar quantities of the reaction products can be calculated by Equation 4.4 and 4.5. The mass of the reaction products is obtained by multiplying again with the molar mass as in Equation 4.6 and 4.7.

$$n_{O_2} = n_{H_2O_2} \tag{4.4}$$

$$n_{p,H_2O} = \frac{1}{2} n_{H_2O_2} \tag{4.5}$$

$$m_{O_2} = n_{O_2} M_{O_2} \tag{4.6}$$

$$m_{p,H_2O} = n_{p,H_2O} M_{H2O} \tag{4.7}$$

The liquid water mass after the reaction is determined by summing the water mass present in the fuel solution and the product water mass, depicted in Equation 4.8. Assuming the reaction releases enough heat to fully evaporate this water mass, the total gas mass being generated is described by Equation 4.9.

$$m_{H_2O} = m_{p,H_2O} + m_{r,H_2O} \tag{4.8}$$

$$m_i = m_{H_2O} + m_{O_2} \tag{4.9}$$

It is chosen to simulate the gas generation by a constant inlet mass flow $\dot{m}_i$ of duration t_i, such that the accumulated inlet mass flow integrated over the cycle time will equate to m_i effectively. The duration t_i and actual shape of this mass flow curve are interesting subjects for discussion. Fuel mass burning or decomposition rate could be described by Wiebe functions to describe the gas generation rate accurately [80], however for simplicity reasons it is chosen to assume constant mass flow.
The incoming mass flow should be timed around bottom piston position. Implementation of this inlet timing in the analytic functions of the thermodynamic model is less straightforward than it seems. Appendix A.6 describes how the inlet mass flow timing is analytically described around bottom piston position. The resulting equation is described in Equation 4.10.

$$\dot{m}_i = \frac{m_i}{t_i} \frac{1}{1 + e^{g_1(|\dot{x}| - \dot{x}_i)}} \frac{1}{1 + e^{-g_1 \ddot{x}}} \tag{4.10}$$

This mass flow function will be implemented in the thermodynamic model by replacing the inlet mass flow term in Equation 3.13 and 3.12. It is important to note that in the thermodynamic model, the ideal gas law describes the pressure-density relation by R, which is medium specific. After the first cycles, the initial air present in the expansion chamber is expelled and replaced by oxygen gas and water vapour, which has other molar mass and thereby a different R. Therefore, R, but also specific heat values c_p and c_v, should be updated for the mixture concerned, which is also described in Appendix A.6. Now the inlet mass flow is described and the thermodynamic model is updated for the correct gas properties, the second step is to determine the temperature of the generated gas in order to quantify the inlet energy flow. This is done in the next section.

4.2.4. HEAT GENERATION

Due to the exothermic nature of the reaction described in Equation 4.2.2, heat is released, which subsequently will be used for heating processes in the following chronological order: liquid water and oxygen gas heating until the boiling point of water, liquid water evaporation, and heating water vapour and oxygen gas to their final temperature. This section describes how the final temperature is determined.
Hess's law describes the change in enthalpy of the reaction per mole of reactant, as is described in Equation 4.11 [21]. The heat release Q can be simply calculated by multiplying ΔH with the molar quantity of hydrogen peroxide.

$$\Delta H = \sum \left[\Delta H^{\theta}_{f(products} - \Delta H^{\theta}_{f(reactants)} \right] \tag{4.11}$$

$$Q = \Delta H n_{H_2O_2} \tag{4.12}$$

If full water evaporation is assumed, which is true for a mass fraction c of 0.95, the final temperature of the oxygen and water vapour mixture can be calculated by Equation 4.13 [21], where T_0 is ambient temperature and T_{boil} is the absolute boiling temperature of water.

$$T_i = \frac{Q - C_{evap,H_2O} m_{H_2O} - n_{H_2O} c_{p,H_2O,l}(T_{boil} - T_0) - n_{O_2} c_{v,O_2}(T_{boil} - T_0)}{n_{H_2O} c_{v,H_2O} + n_{O_2} c_{v,O_2}} + T_{boil} \tag{4.13}$$

The inlet energy flow $c_p \dot{m}_i T_i$ in the thermodynamic model from previous chapter is updated by replacing the inlet temperature with the temperature calculated in Equation 4.13. After doing so, the thermodynamic model from the previous chapter, which assumed high pressure pulses of air as inlet, is fully updated for the chemical decomposition reaction of hydrogen peroxide. The energy intake can be regulated by setting V_f

to the performance demands. Now the full actuator response can be modelled for hydrogen peroxide fuel intake, a initial model evaluation is done in the next section to determine a suitable V_f.

EFFICIENCY

To determine if the actuator would able to achieve the research goal, the efficiency should be determined. Note that the output power is the power dissipated in the damper, which can be related to lift production as is described in Appendix A.1. The efficiency of the chemical actuator can be calculated by Equation 4.14

$$\eta = \frac{\int_0^{t_1} b\dot{x}^2 dt}{e_{H_2O_2} \int_0^{t_1} \dot{m}_i dt} \tag{4.14}$$

where $e_{H_2O_2}$ is the energy density of hydrogen peroxide and t_1 the period of which the efficiency should be calculated.

4.2.5. THERMODYNAMIC MODEL RESULTS AND FUEL VOLUME DETERMINATION

A suitable droplet size should be determined for the droplet transport experiment later in this chapter. The droplet size in the droplet transport experiment must be is roughly comparable with the droplet size of future miniature actuator designs, since experimental conclusions regarding the droplet trajectory will then also be valid for future designs. Therefore, bellow in the measurement setup of previous chapter is used as reference for the fuel volume determination, since it represents the approximate size of a chemical actuator for a FW-MAV.

The actuator model response is thus evaluated using the geometry of the expansion chamber setup from previous chapter, using a hydrogen peroxide concentration of 95%. The fuel volume V_f is swept in order to find a suitable quantity that will keep the vibration of the mass in the measurement setup within the maximum allowed bellow deformation, and a volume V_f of 28 nL was determined. The associated output power and efficiency are 0.22W and 5% respectively, which are not enough to reach the specific power requirement from Equation 2.2. It should be noted that the bellow geometry and the parameters s_b, b, m are non-optimal for maximum power output and efficiency, which is not necessary for this stage of development. Figure A.6 in Appendix A.7 can be referred to for the model results.

Subsequently, a choice has to be made into how much separate droplets this volume is divided. This is an important consideration since droplet transport dynamics as well as catalysis reaction speed is greatly influenced by droplet size. Moreover, a larger quantity of droplets results in a larger quantity of injection modules, making it possible to regulate fuel inflow by actuating only a fraction of the injection modules.

Meskers reported a minimum reaction time of 70 ms for a relatively large hydrogen peroxide droplet volume of 22μl and hydrogen peroxide-water mass relation of 30%-70%. Reaction time could be significantly decreased if droplet volume is decreased or hydrogen peroxide concentration is increased [47]. Based on aforementioned considerations, a droplet diameter of 300μm is chosen for in current analysis. This will lead to four injection modules and a droplet volume of 7 nL. If this volume droplet reduction and increased concentration compared to the research of Meskers will lead to sufficient decrease of reaction time has to be further investigated, however this lies outside of the scope of this study.

4.3. DROPLET TRANSPORT BY ELECTROWETTING-ON-DIELECTRIC

4.3.1. INTRODUCTION

After aforementioned analysis investigated the amount of fuel that should be ejected onto the catalyst once every cycle, the droplet motion will be investigated in this section.
Considerable research is conducted in the area of EWOD for transporting and splitting of droplets for unit processes including encapsulation, mixing and extraction of biomedical liquids on biochips [40, 50]. However, this research is mainly focussed to the field of medical diagnosis or drug delivery where accuracy and consistency of the volume are paramount [40, 51], in contrast to droplet speed. To be suitable as an injection concept, this the droplet transport technique should be able to demonstrate a high droplet velocity as well as a high dispensing frequency. This research area is not well-covered and not trivial since unlike regular droplet motion in normal channels with constant pressure drop, the droplet movement is of discrete and unsteady nature due to the sequential electrode switching [50]. Therefore it is chosen to investigate the droplet dynamics of EWOD and model the trajectory of the droplet, to determine if the droplet can be transported from reservoir to catalyst within the available time.

4.3.2. INITIAL DESIGN CONSIDERATIONS AND PLATE CONFIGURATION

During the design of the injection module, the objective is to maximize droplet transport velocity and keep the droplet splitting duration under the cycle period of the actuator. The droplet transport velocity should be maximized, since this will maximize the spacing between a droplet that touches the catalyst surface and a droplet that is 'underway' on the accelerator section of the injection module. This is favourable, since the decomposition of the droplet that has reached the catalyst surface will generate a high temperature pressure wave that is unfavourable for robust droplet transport.
In terms of substrate layout, two main plate configurations are possible to generate the required electric field, each having different performance in terms of the droplet transport velocity they can achieve.

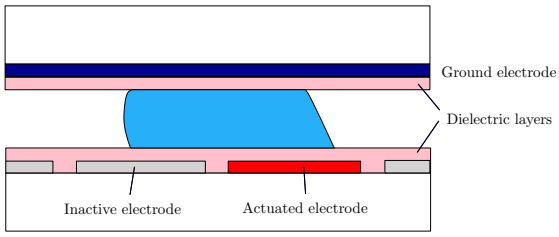

Figure 4.4: Parallel-plate configuration

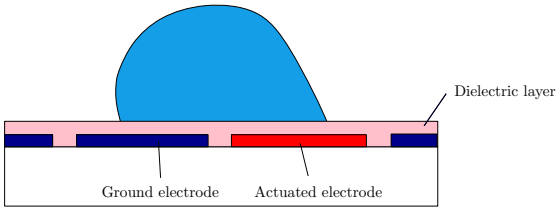

Figure 4.5: Single-plate configuration

The first type, the parallel-plate configuration, consists of two plates placed in parallel arrangement from eachother with an air gap in between, as is depicted in Figure 4.4. The bottom plate situates the driving electrodes insulated by a dielectric layer and hydrophobic layer, which are actuated sequentially to initiate droplet movement. A continuous grounding electrode is positioned in the top plate, above all the driving electrodes, to ground the liquid droplet [13]. This grounding electrode is insulated by a dielectric layer and hydrophobic layer as well, but also non-insulated versions are possible, dependent on the device characteristics [13, 61].
In the second type, the single-plate configuration, only a single plate is used to situate the electrodes embedded in a dielectric layer and hydrophobic layer, as depicted in Figure 4.5. The electrodes are sequentially switched from actuated state to grounded state to drive the droplet. Advantages of this configuration with respect to the parallel-plate configuration include faster mixing, simpler mechanical design, reduction in viscous drag, increased transport velocity and the capacity to move larger volumes on a given footprint [3, 13]. Therefore, it is chosen to proceed with a single-plate configuration, since maximum droplet transport velocity is key.

4.3.3. DROPLET TRAJECTORY MODEL

FORCE GENERATION

To analyse the dynamics of the droplet transport, the following model was constructed. A conducting droplet of contact radius r lies on a dielectric layer with permittivity ϵ_r and thickness t. Under the dielectric layer, rectangular electrodes are situated of width w as depicted in Figure 4.6. The electrode gap width is assumed to be negligible in this analysis. If a voltage is applied between the electrode and the droplet, a line force

density f_w is generated at three-phase contact line (TCL) depending on the local voltage V underneath. The line force density can be described by Equation 4.15 [7, 13].

$$f_w = \frac{\epsilon_0 \epsilon_R}{2t} V^2 \tag{4.15}$$

$$\cos\theta(V) - \cos\theta_0 = \frac{\varepsilon_r \varepsilon_0}{2\gamma_{lg} t} V^2 \tag{4.16}$$

This leads to a change of the local contact angle from θ_0 to θ_V along this line described by the Lippmann-Young equation 4.16[13], where $\gamma_l g$ is defined as the liquid surface tension. There exists an upper limit for the voltage V, where electrical breakdown occurs of the dielectric layer. This voltage limit can be calculated by Equation 4.17, where E_{bd} is the dielectric strength of the layer.

$$V_{bd} = E_{bd} t \tag{4.17}$$

Additionally, there is another phenomenon that bounds the actuating voltage. Above a certain threshold voltage, contact angle saturation occurs, making Equation 4.15 being no longer valid [**?**] and leading to an upper limit for f_w. Increasing the actuation voltage until contact angle saturation might also lead to permanent damage to the insulator [**?**]. Therefore, the device should ideally be operated under the voltage where the saturation effect of contact angle occurs, which can be described by Equation 4.18 [42].

$$V_{sat} = \sqrt{\frac{2t\gamma_{lg}(\cos\theta_{sat} - \cos\theta_0)}{\epsilon_0 \varepsilon}} \tag{4.18}$$

If contact angle hysteresis is neglected, the driving force F_w on the droplet in x-direction can be obtained by integrating the line force density f_w over the contact line as follows.

$$F_w = \int_{TCL} f_w cos(\phi) dl = \frac{\epsilon_0 \epsilon_R}{2t} L V^2 \tag{4.19}$$

where L is the projected length of the TCL in x-direction, which is not influenced by the shape of the TCL above the active electrodes. It should be noted that for this equation to be valid, the electrodes should extend past both sides of the droplet in vertical direction. If the different electrodes are switched from high voltage to ground in a sequential manner, the droplet will be constantly pulled towards the active electrodes and therefore accelerated.

OPTIMAL SWITCHING SEQUENCE

Sequential switching with constant switching rate is widely implemented across literature, however literature about optimal sequential switching control for maximum acceleration is relatively scarce. The majority of literature that studies droplet velocity does not show careful control of the switching time such that a droplet does not have to wait until a subsequent electrode is set active [50, 77]. Therefore, the optimal switching sequence is investigated further by means of Figure 4.6. Depending on the position x of the droplet, an optimum combination of electrodes should be switched on to maximize F_w. This optimum combination of electrode switching can be characterized by $x_w(t)$, which defines the boundary line between the active electrodes and ground electrodes. Now x_w is defined as a function of x_c in Equation 4.20.

$$x_w = x + x_c \tag{4.20}$$

To maximize F_w, the projected length L should be maximized and consequentially an electrode actuation state should be chosen such that x_c is minimized. The minimum x_c possible is defined as in Equation 4.21 by using a remainder operator.

$$x_{c,opt} = sgn(2(x \mod w) - w) * min((x \mod w), w - (x \mod w)) \tag{4.21}$$

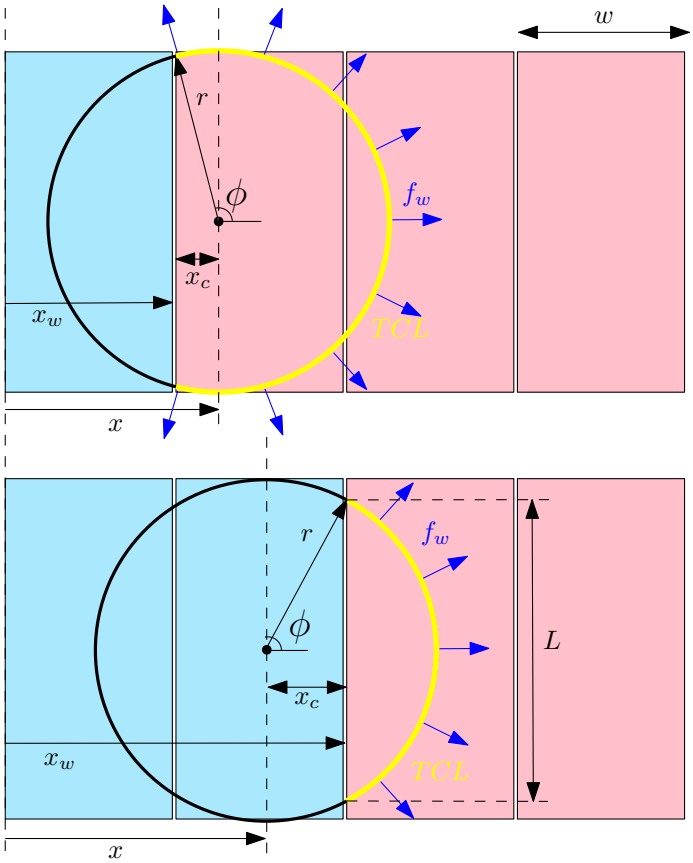

Figure 4.6: Schematic of acceleration electrodes including dimensions. The actuated electrodes are depicted in red and the inactive electrodes are depicted in blue.

Using trigonometry, the following equation for F_w will be true if the electrode switching sequence is optimized.

$$F_{w,opt} = \frac{\epsilon_0 \epsilon_R}{2t} V^2 \left[2\sqrt{r^2 - x_{c,opt}^2} \right] \tag{4.22}$$

DRAG FORCE

Drag force F_{shear} is induced by viscous surface-shear stress and can be described by Equation 4.23 [3], where μ is the viscosity and h the droplet height.

$$F_{shear} = \frac{5\mu\dot{x}}{2h}\pi r^2 \tag{4.23}$$

If contact line friction and other drag forces are neglected, the the droplet trajectory can be obtained by solving Equation 4.24 numerically for x from initial conditions $x = 0, \dot{x} = 0$.

$$\ddot{x} = \frac{F_{w,opt} - F_{shear}}{\rho_{H_2O_2} V_d} \tag{4.24}$$

INITIAL MODEL EVALUATION AND EXPERIMENT COMPARISON

An initial model evaluation is done and the result is compared with literature data from research by Baneerjee et al. The modelled and experimental droplet trajectory is visualised in Figure 4.7., as well as the optimal electrode switching state x_w. The red line depicts the driving force as a result of this sequential switching, which shows a relatively low force variation as the droplet moves over the electrodes. Electrodes should be slender (low w/r ratio) to limit the effect of force variation.

The discrepancies between experimental data from Baneerjee et al. and the developed model that can be observed in Figure 4.7 are the following. The initial acceleration (at 0-2 ms) is higher in the experimental data

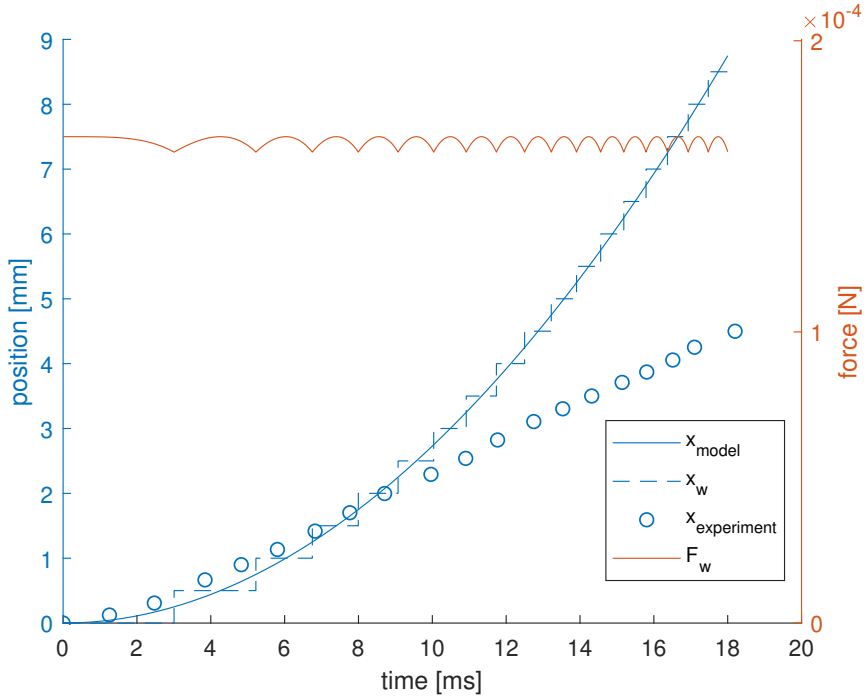

Figure 4.7: Trajectory of droplet (blue): model compared with experiment. In red, the modelled driving force F_w is given. Parameters used: $w = 0.5$mm, $V_d = 3.9\mu$l, $\epsilon_r = 3.9$, $t_d = 2.5\mu$m, $U = 110V$, r = 1 mm

and a saturation in velocity is observed, what is not observed in the model. The higher acceleration can be explained by the fact that the leading edge of the droplet is measured in the experiment, in contrast to the center of gravity that the model assumes. Deformation of the droplet leads to a higher initial acceleration of the leading edge, while the center of gravity does not accelerate as much. The velocity saturation could be easily explained by the fact that a constant switching rate is used in their study, in contrast to the variable switching rate of the model.
What can be also observed from this comparison is that the experimental acceleration (from 1-4 ms) is roughly comparable (±30%) with modelled acceleration.
This initial inspection of literature data of Banerjee et al. and model analysis yields the following initial findings.

1. Acceleration comparison (from 1-4 ms) suggests that the force generation predicted by the model is actually possible to achieve (within error range of 30%)
2. Model comparison suggests it is advantageous for droplet velocity if a variable switching rate is implemented
3. The experiment of Banerjee et al. shows that droplets can be transported over a distance of 4 mm within a time of 18 ms, which comparable to what is required for the injection module.
4. Modelled droplet acceleration scales inversely quadratic with droplet radius

The promising initial findings show that the proposed concept could potentially achieve a desired droplet trajectory. This also motivates further experimental validation of the model.

4.3.4. DROPLET SPLITTING

Now the droplet trajectory in the accelerating section can be mathematically related to the design parameters of the injection module, the duration of the droplet splitting event should be investigated, in order to verify if the whole sequence of droplet manipulations can be performed within one cycle. Favourably, a reasonably accurate analytic or reduced model should be used to calculate the dynamic behaviour of droplet splitting. If this exists or possible to deduce, this provides significant time saving in the design stage and is also more insightful [8]. Although analytic static splitting models are widely proposed in literature [16**?**], analytic models

to calculate the dynamic behaviour of droplet splitting are scarce or non-existing. Therefore, several research projects used finite element modelling to investigate the influence of geometric parameters and material properties on the droplet generation dynamics [8, 57], whereas other literature does this investigation by performing experimental work [8, 51]. Current study does not model the dynamic splitting behaviour, although two literature research projects are investigated to give initial conclusions about the feasibility of the duration of splitting action. Figure 4.8 depicts the electrode layout used for the splitting method of current design as well as the layouts used in the studied literature. Figure 4.8 also describes the desired splitting duration and desired droplet volume of current design, as well as the proven splitting times and droplet volumes of the literature experiments.

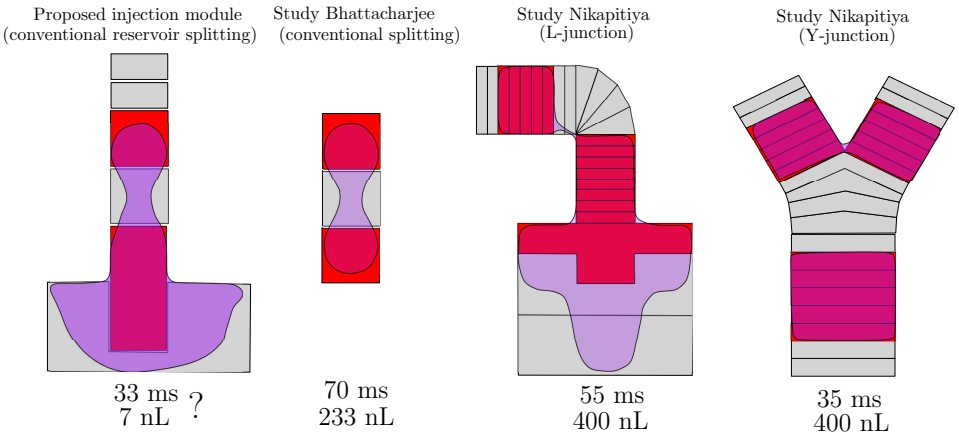

Figure 4.8: Splitting methods (from left to right): Conventional reservoir splitting, conventional electrode splitting [8], L-junction splitting, Y-junction splitting [51]

Electrohydrodynamic simulations and experimental work by Bhattacharjee investigated droplet splitting by using three square electrodes and concluded that 247 ul droplets are able to be splitted within 70 ms. Nikapitiya et al. researched the droplet dispensing frequency of 400 nL droplets from a reservoir using an L-junction. The study concluded that L-junctions could significantly decrease splitting time to 55 ms, compared to a splitting time of 230 ms when using a conventional reservoir for this droplet size. Subsequent droplet splitting of a 400 nL independent single droplet could be performed by Y-junction within 35 ms. If both junctions are added in series, the droplet generating rate could be as high as 36 Hz for these device and droplet dimensions [51].
Droplet splitting time can be further reduced if droplet size is decreased [8]. Despite the fact that the experimental findings of splitting durations of the concerned literature cannot be directly applied to the electrode design of current research, it can be assumed that splitting durations between both layouts do not lie an order of magnitude apart.
This initial investigation of droplet splitting shows that a droplet dispensing frequency of 30 Hz is not proven yet. However, the literature investigated make it plausible that this would be possible, if one compares the droplet volumes used and splitting durations achieved. This motivates that further research should be conducted to experimentally verify the minimum duration of reservoir splitting.

4.3.5. INITIAL MODEL RESULTS

If it is assumed that the electrodes are actuated at the contact angle saturation voltage, the droplet trajectory can already be modelled without a notion of the dielectric layer thickness and material. Equation 4.18 and Equation 4.22 are substituted in Equation 4.24 and numerically solved to obtain the droplet trajectory over the acceleration section. For now, it is assumed that before the droplet acceleration event, the droplet is split from the reservoir in 33 ms with constant velocity. It is also assumed that the splitting event takes place on the first six electrodes. After the acceleration section, the droplet flies in the flying section with constant velocity towards the catalyst surface. For a droplet volume of 7 nL, and 16 electrodes of width w of 200 μm, the modelled trajectory of multiple droplets is depicted in Figure 4.9. Note that droplets are sequentially dispensed and accelerated with a frequency of 30 Hz. The trajectories indicate that with this geometry, the droplet of 7 nL can be transported over the acceleration section and flying section within 7 ms. The electrode array size would make this injection module suitable for integration in the previously built expansion chamber.

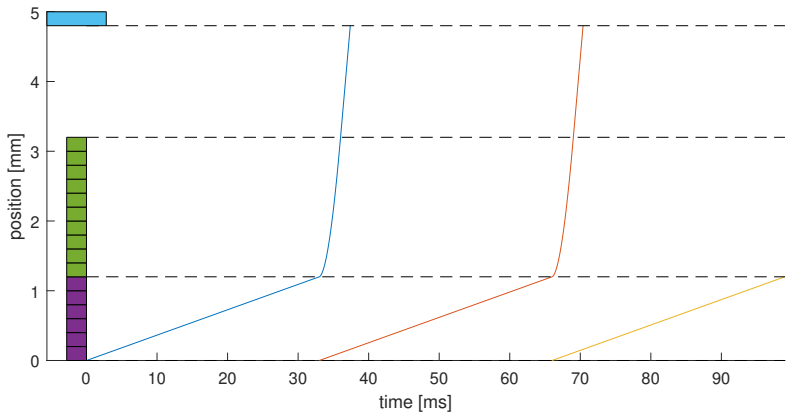

Figure 4.9: Droplet trajectory for three droplets that are dispensed from the reservoir with a frequency of 30 Hz. A schematic of the electrode array and catalyst is visualised on the left.

4.4. EXPERIMENT

After studying how the geometric and fluid variables are influencing droplet dynamics, an experimental study is conducted aiming to validate the droplet transport models and investigate if a desired transport trajectory can be achieved. Experimental analysis of the decomposition reaction is beyond the scope of this study and therefore all experiments are performed with DI water.

4.4.1. MEASUREMENT SETUP

ELECTRODE PATTERN AND GENERAL DEVICE PARAMETERS

The core part of the developed measurement setup is the injection module itself, which consists of a glass slide with a gold-film electrode pattern. Figure 4.10 shows a microscopic image of the electrode pattern, consisting of a reservoir and a linear electrode array of 16 electrodes. Figure 4.12 shows a microscopic image of a single electrode. The electrode dimensions are given in Table 4.1. Interdigitated electrodes geometry were used to partly mitigate the effect of electrode gap [34], since the electrode gap reduces the active length of the TCL.

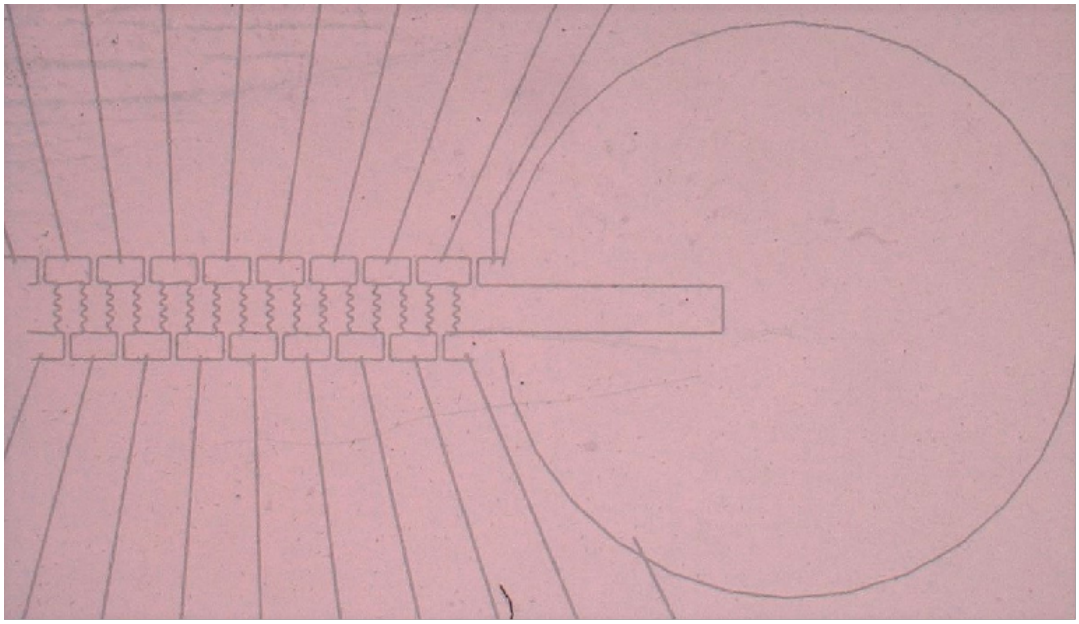

Figure 4.10: Microscopic image of full electrode array and reservoir

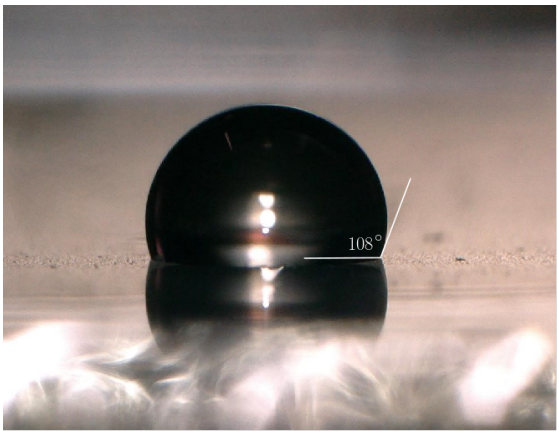

Figure 4.11: Initial contact angle (108 °) of DI water droplet on Fluoropel surface

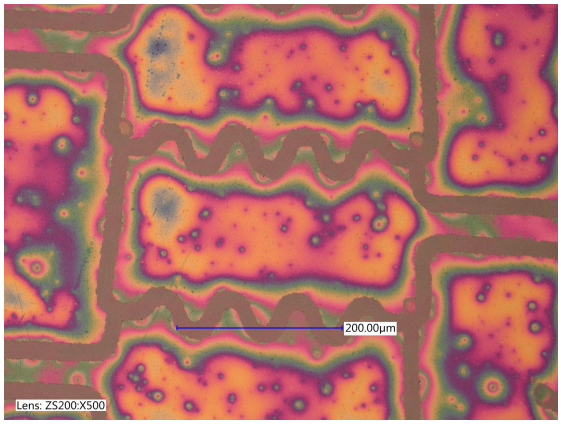

Figure 4.12: Microscopic image of single electrode

The electrodes were manufactured by physical vapor deposition of gold onto a rectangular glass slide, which is further described in Section 4.4.2. The insulative lines that actually pattern the electrodes , indicated by

the darker lines in Figure 4.10, are removed by laser-depletion. Design and manufacturing considerations of the insulation lines are further highlighted in Section 4.4.2. The electrode array is covered with a SU-8 dielectric layer and Fluoropel hydrophobic layer. The initial contact angle of a DI water droplet on Fluoropel is measured at 108 °, as is visualised in Figure 4.11. The spincoating procedure is further explained in section 4.4.2. For this material choice and the spincoating parameters used, the film thicknesses are estimated to be as described in Table 4.1. Table 4.1 also gives an estimation for the estimated breakdown voltage as well as an estimation for the voltage at which contact angle saturation occurs. The device will be first operated at 130V, well under the estimated breakdown voltage of 147 V.

Device parameter	**Value**
electrode width w	200 μm
electrode length L_e	400 μm
thickness SU-8 [49]	0.7 [μm]
thickness Fluoropel [43]	30 [nm]
Breakdown voltage	147 [V]
initial contact angle θ_0	108 °
saturation contact angle θ_{sat} [15]	70 °
saturation voltage	164 [V]

Table 4.1: Device parameters of injection module

ELECTRODE VOLTAGE SUPPLY AND CASING

The electrodes are connected electrically by 3M Anisotropic Conductive Film 7371 to PCB contacts, which are connected to FET driver module by a set of cables. The driving module switches the electrode voltages to either high voltage or ground, triggered by control signals provided by an Arduino Due microcontroller. The high voltage is generated by a high voltage power supply. The slide with electrodes, PCB contact pads, driver module and microcontroller are integrated in a casing depicted in Figures 4.13 and 4.14. Figure 4.15 shows an exploded view and cross-sectional view on how the different components are situated relatively to eachother. A clamped stack of layers is created to make contact between the PCB contact pads, conductive adhesive layers and gold contact pads on the EWOD slide.

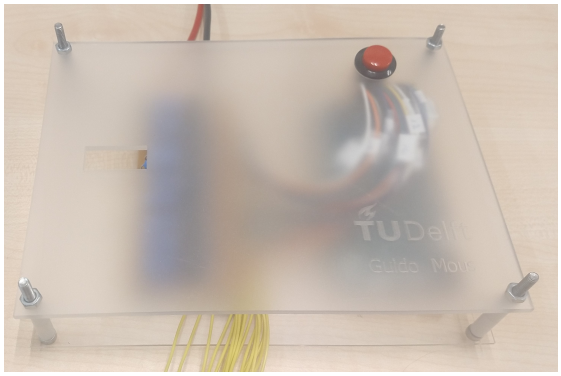

Figure 4.13: Top view of the measurement setup casing

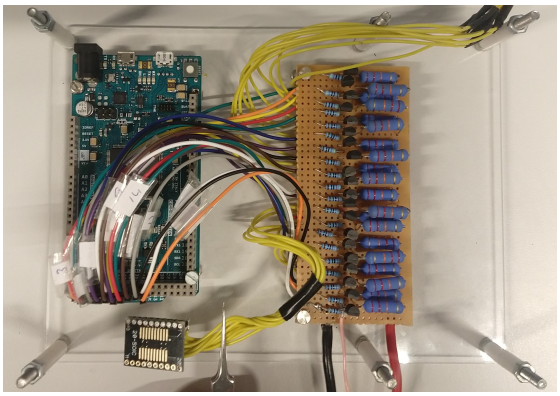

Figure 4.14: Top view of the internal circuitry of the voltage supply, consisting of the Arduino as microcontroller, a MOSFET array for electrode switching and a PCB for substrate connection.

4.4.2. FABRICATION

In this section, the fabrication procedure of the electrode pattern on the glass slide as well as the procedure of dielectric and hydrophobic layer coating is given. The advantage of the fabrication process is that the full sequence from gold deposition until glass coating can be performed within hours at the university.

ELECTRODE PATTERNING PROCEDURE

First, the glass slide was cleaned with IPA before rinsing with DI water and drying to ambient air. Secondly, physical vapor deposition of gold was performed for 60 seconds at 20 mA onto the glass slide. Subsequently,

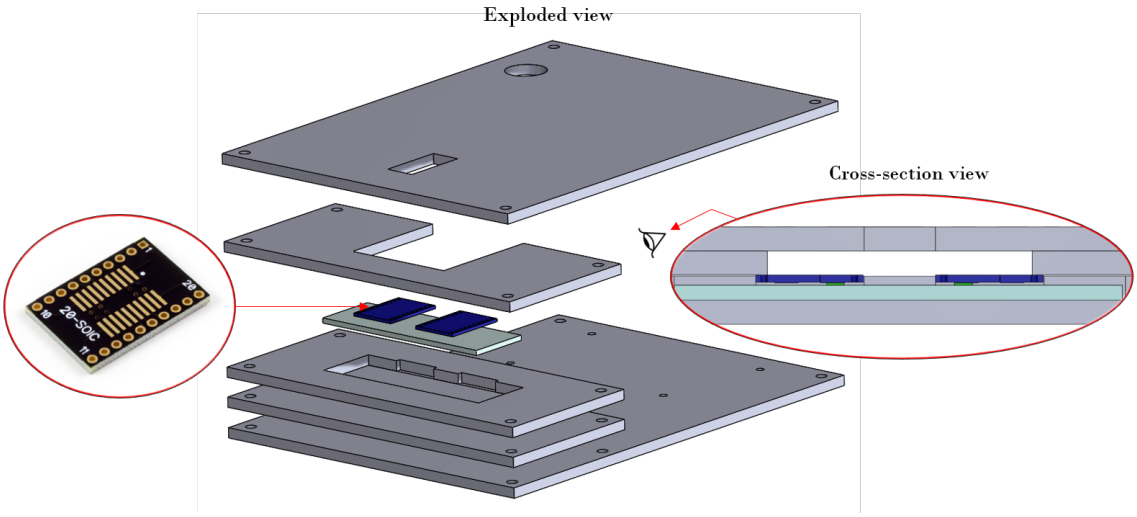

Figure 4.15: CAD of the casing components including PCB board in blue, conductive adhesive layers in green and glass slide in light blue. Spacers, wiring, Arduino and MOSFET board are excluded in this figure.

the gold film was patterned by removing insulative lines (black in Figure 4.16) with laser depletion. Since the line width and glass damage are strongly dependent on the laser settings, the laser current, frequency, repetition and speed were swept to investigate settings that minimized the line width as well as guaranteed sufficient insulative property. The effect of the current setting is displayed in Figure 4.17.

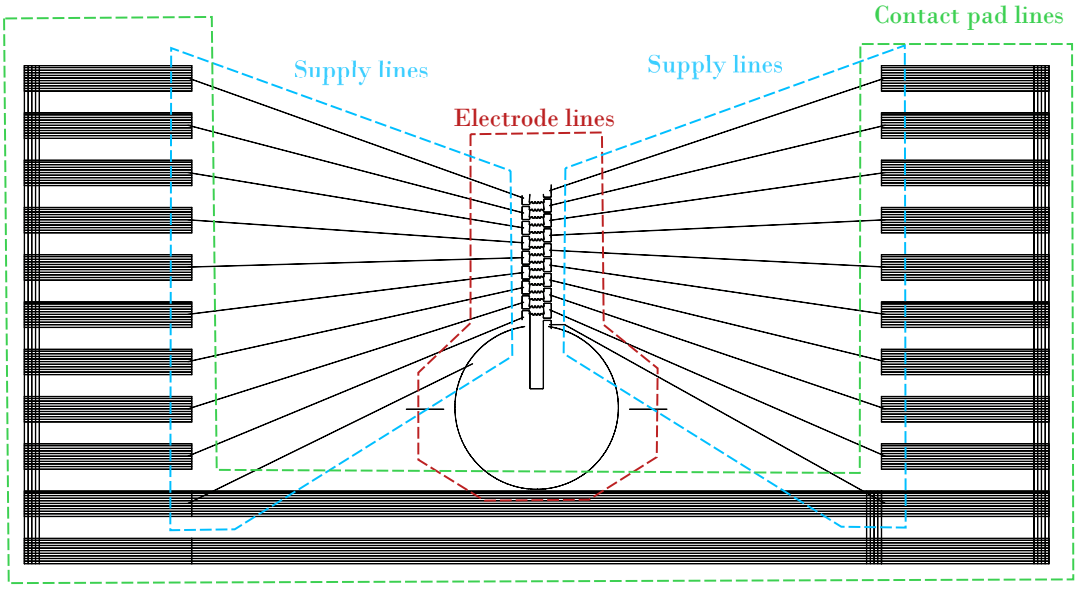

Figure 4.16: Insulative pattern. Different regions are visualised where different laser settings were used.

Current was differentiated for different sections of the insulation area. For areas that lie far from the potential droplet locations, a higher current was used to create wider insulation lines to cover the required insulated area in minimal amount of laser operations. The different areas are denoted in Figure 4.16. All insulative lines were depleted with the following laser settings: 50 kHz frequency, 1 repetition, 100 mm/s laser velocity with varying current. For the electrode lines, supply lines and contact pad lines a laser current of 2.3A, 2.6A and 4.6A was used respectively. At some line intersections, insulation lines are purposely extended 20μm past their intersection point, to prevent leaving a short-circuiting path in case of manufacturing inaccuracies.

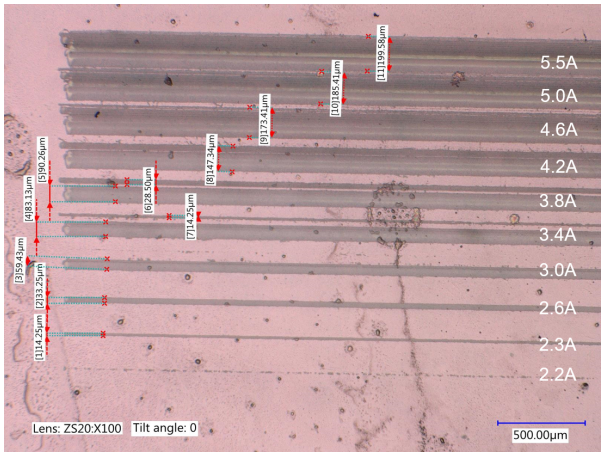

Figure 4.17: Different laser depletion current settings, 50 kHz frequency, 1 repetition, 100 mm/s laser velocity.

DIELECTRIC AND HYDROPHOBIC LAYER DEPOSITION

For the dielectric layer, necessary voltage can be reduced by minimizing term $\frac{\epsilon_r}{2t}$. However, ease of fabrication will be dominant in this study. Therefore, a combination of diluted SU-8 2007 and Fluoropel 1601V was chosen as the dielectric layer and hydrophobic layer, which can both be applied by spin-coating.
The dielectric and hydrophobic layer was applied by the following steps. First, the glass slide with gold film was cleaned again with IPA before rinsing with DI water and drying to ambient air. The contact pads were masked by Kapton tape. The SU-8 resin was prepared by diluting SU-8 2007 with solvent cyclopentanone with mass-ratio m_{cp}/m_{SU-8} of 2.67 to achieve a desired viscosity of 2.5 cSt. Gas bubbles were removed by placing the solution for an hour in a vacuum desiccator. Subsequently, the substrate was placed in the spin-coater and 1 mL of SU-8 solution was dripped onto the center. A spread cycle of 500 rpm was performed for 10 seconds before a spin cycle of 30 seconds at 2000 rpm. Afterwards, the substrate was baked at a hotplate of 150 °C for 15 minutes. After cooling in ambient air, 0.5 mL Fluoropel was spincoated by a spreading cycle of 10 seconds at 500 rpm followed by a spin cycle of 60 seconds at 3000 rpm. Subsequently, the substrate was baked on a hotplate for 10 minutes at 80 °C and 10 minutes at 160 °C, before the Kapton tape was removed to expose the electrical contacts.

4.4.3. DROPLET ACCELERATION EXPERIMENT

When fabrication was complete, the main experiment was carried out. The goal of the main experiment, the droplet acceleration experiment, is to accelerate a 7 nL droplet over the linear electrode array, by actuating the electrodes in a feed-forward loop and determine if the validate if the modelled droplet trajectory can be achieved.
A 7 nL with 3 g/L NaCl droplet was dispensed with a pipette on the first electrode of the injection module. Subsequently, the electrodes were actuated in a feed-forward loop that follows the optimum switching sequence and droplet displacement was measured as a function of time.

4.4.4. FUNCTIONAL VERIFICATION EXPERIMENTS

The original droplet acceleration experiment did not give the desired outcome, since contact angle change nor droplet motion was achieved. Different functional verification experiments were carried out to verify if independent components were working correctly, and to identify the failure causes of the system. The following experiments were carried out in chronological order. For each experiment, the goal and method are discussed.

FUNCTIONAL EXPERIMENT

The functional experiment was carried out to investigate if any actuated electrode could induce contact angle change and droplet motion in the first place. No feed-forward electrode actuation was done.
A 7 nL with 3 g/L NaCl was dispensed on the electrode array. The electrodes were manually actuated one-by-one to see if contact angle change or droplet motion could be induced. The experiment was repeated by displacing the droplet to each of the other electrodes. The experiment was repeated again by grounding the

droplet with a wire that is inserted into the droplet, to increase the electric field over the TCL.

ELECTRODE VOLTAGE SUPPLY EXPERIMENT

Since contact angle change nor droplet motion was achieved in previous experiment, a functional verification experiment was carried out to investigate if the correct voltage was supplied to the gold electrodes.
First, voltage measurement of the PCB pads was used to identify if the MOSFET circuit was working correctly. Second, a glass slide with a continuous gold film was fabricated. Then the PCB was adhered to the top of the gold-coated slide by the conductive film, and it was clamped and placed in the setup as depicted in 4.15. Resistance measurement performed between the PCB contacts was used to identify if the conductive film gave a conductive connection between PCB and gold substrate.

ITO GLASS EXPERIMENT

The goal of this experiment was to demonstrate significant contact angle change and droplet motion, on a new ITO-glass substrate with a significantly simplified electrode array.
The new simplified electrode design is given in Figure 4.18.

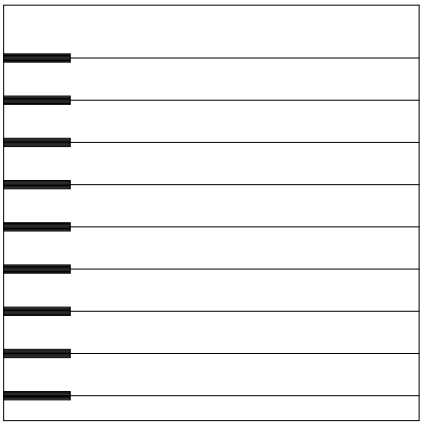

Figure 4.18: Electrode pattern of ITO coated glass device

A prefabricated ITO-glass was used instead of the glass slide with gold film, to significantly increase the robustness of the conductive layer. The conductive layer was patterned by the same method as previously described and the hydrophobic and dielectric layer were also fabricated as previously described. was used to have a more robust conductive film. A 1 μL droplet with 3 g/L NaCl was dispensed on the substrate and electrodes were manually actuated one-by-one to see if contact angle change or droplet motion could be induced. The experiment was repeated again by grounding the droplet with a wire that is inserted into the droplet.

4.5. RESULTS AND DISCUSSION

Successful droplet transport was not achieved in any of the conducted experiments, nor repeatable contact angle change without permanent damage to the injection module substrate. The functional verification experiments were used to check which parts of the were successfully functioning and identify the failure causes. In this chapter, we discuss the potential failure causes that are identified in these subexperiments and discuss how these failure causes can be mitigated in future designs. It is chosen to summarize this failure cause analysis in a table. Table 4.2 summarizes for each experiment:

1. The phenomenon that each experiment aims to verify. It also describes if this was verification was achieved.
2. The possible failure cause, if this phenomenon is not observed.
3. The consequence of this failure cause.
4. How this failure cause can be mitigated in future designs. It also describes if this mitigation step was performed in a subsequent experiment.

Appendix B.4 can be referred to for a full description of this experimental failure cause analysis.

Experiment	Verify		Failure cause	Consequence	Mitigation	
Droplet acceleration	Droplet trajectory	×	Incorrect voltage supply	No force generation	Redesign voltage supply	✓
Functional experiment	Contact angle change and droplet movement	×	Incorrect voltage supply	No force generation	Redesign voltage supply	✓
Electrode voltage supply	Electrode voltage	×	Conductive film makes no contact to each gold electrode tab	No voltage supply to electrode	Redesign PCB connection	✓
					Use DIMM connector for electrical connection to substrate	×
					Use wire bonding for electrical connection to substrate	×
			Gold film breakage	No voltage supply to electrode	Improve adhesion by plasma etching	×
					Use premanufactured ITO glass	✓
ITO glass A	Contact angle change and droplet movement	×	Contaminations under dielectric layer as glass flakes or dust	Dielectric breakdown	Perform more thorough cleaning procedure before spincoating	✓
			Dielectric layer too thin	Dielectric breakdown	Choose actuating voltage based on measured dielectric thickness	×
					Increase dielectric thickness by spincoating with higher SU-8 viscosity	✓
ITO glass B	Contact angle change	✓				
	Droplet movement	×	Contaminations under dielectric layer as glass flakes or dust	Dielectric breakdown	Perform even more thorough cleaning procedure before spincoating	×
			Spatial variation of dielectric layer thickness	Dielectric breakdown	Use other masking method than Kapton tape	×
					Use other deposition method than spincoating	×
			Hydrophobic layer too thin	Charge trapping and hydrophobic layer damage	Increase hydrophobic layer thickness	×

Table 4.2: Experimental failure mode analysis. In the first two columns, this table describes what phenomenon the experiments try to verify, and if this achieved (achieved: ✓, not achieved: ×). The last three columns describe what the expected failure causes are, what the consequence is of this failure cause, and what steps can be undertaken to mitigate the failure cause. If this mitigation step was performed in the subsequent experiment is also denoted in the last column (performed: ✓, not performed: ×).

4.6. CONCLUSION

The developed thermodynamic model of the compliant expansion chamber and passive exhaust valve is expanded with a chemical model that describes the gas and heat generation as a function of hydrogen peroxide fuel volume. The outputs of this model, which include the displacement response, pressure response, pressure-volume diagram and the conversion efficiency, is valuable information for the generation of future designs. The model estimates that a fuel volume of 28 nL is needed to power expansion chamber in the measurement setup from previous chapter. Future research has to be conducted in order to verify if reaction time of the hydrogen peroxide catalyst reaction can be reduced to a fraction of the 33 ms cycle time. Also, it is recommended to integrate a hydrogen peroxide fuel injection module and catalyst into the earlier proposed expansion chamber to validate the functioning of the full system.
The modelled trajectory of fuel droplet transport by EWOD on a linear electrode array of 16 400x200 μm electrodes is suitable for high frequency droplet delivery onto the catalyst. The droplet trajectory model suggests that a significant droplet delivery speed improvement can be made if the sequential actuation of the electrodes is performed in an optimum manner, maximizing the length of the actuated TCL on every location of its trajectory. In future research, experimental work has to be performed in order to validate this modelled trajectory, and investigate the scaling laws of this estimated trajectory, since this could not be performed in this research. Also, high frequency droplet splitting from a reservoir should be demonstrated in future experimental work.
The following conclusions can be drawn from the fabrication procedure of the EWOD electrode pattern. Electrode fabrication by gold-sputtering on a glass slide and sequential insulative lines removal by laser depletion is a promising, simple fabrication concept and is advantageous if fast prototype iteration is strived for. Significant robustness improvements have to be made to the electrode layer to have successful integration in a practical EWOD chip, such as adhesion improvement by plasma-cleaning.
Special attention has to be given to the smoothness and cleanliness of the electrode layer before spincoating, since contaminants might otherwise cause dielectric film imperfections that will lead to short-circuiting. Finally, careful consideration of the spatial variation of dielectric and hydrophobic thickness as well as actuation voltage is necessary to reduce the possibility of dielectric breakdown and charge trapping. Nonetheless, despite that experimental droplet acceleration was not achieved, the initial investigations and developed droplet transport model show that a set of compact injection modules can deliver sufficient hydrogen peroxide fuel volume to pressurize the proposed actuator.

5

TOWARDS A PRACTICAL DESIGN FOR 10 MINUTES OF FLIGHT ENDURANCE

5.1. INTRODUCTION

In Chapter 3, the proof-of-concept of the compliant expansion chamber and passive exhaust valve was demonstrated. In addition, the measured time-dependent pressure and displacement data showed the correct descriptive performance of the thermomechanical model. In this chapter, we will use the thermomechanical actuator model to determine actual geometrical parameters of a compliant expansion chamber that would fulfill the requirements of a FWMAV with 10 minutes of flight endurance.

5.2. CONSIDERATION OF OPTIMISATION FOR MAXIMUM FLIGHT ENDURANCE

In order to support 10 minutes of flight endurance, the actuator should comply with the power-to-weight requirement defined in Chapter 2. Also, the actuator should comply with the mass requirement, which limits the mass of the actuator to 5 grams, and should ideally have a cycle frequency of 30 Hz to be in the optimal range of flapping frequencies. To be able to explore the design space that is able to comply with these requirements, an optimisation of the actuator parameters would be insightful.
However, an optimization of the geometrical parameters D_o, D_i, L and mechanical parameters b, m, s to maximize the flight endurance is beyond the scope of this study. To do this correctly, one requires more information than the actuator model currently can capture. For example, it should be known how the key parameters as actuator mass and heat loss coefficient scale with model parameters (D_o, D_i, s, L, b, m). This optimization is an interesting subject for further research, but not possible yet. The geometrical parameters of the proposed practical actuator are chosen by logic, rather than extensive multidimensional optimisation of the model.

5.3. A PRACTICAL BELLOW DESIGN

Essentially, the work performed by the gas expansion is a result of the area under the pressure-volume diagram, and is thus directly related to the volume change (between maximum and minimum deformation of the bellow) and pressure change (between maximum pressure after the catalyst reaction and ambient pressure). The actuator model suggests that it does not strictly matter if this volume change is a result of a high-stroke, low-area combination or a low-stroke, high-area combination. However, in order to minimize the heat loss (the importance of minimal heat loss is clarified later), it is favourable to have minimal surface area of the bellow wall. That demotivates the use of slender ($D_o << L$) or flat ($D_o >> L$) bellow geometry. The optimal ratio (D_o/L) is dependent on the amount of corrugations and other geometrical aspects, but is estimated to be approximately two for the chosen bellow design. The bellow variables chosen are depicted in Table 5.1. Considering the maximum strain ($\Delta x/L$) of the smaller bellow used in the measurement setup, a maximum

Bellow parameter	**Value**
Length L	10 mm
Outside diameter D_o	20 mm
Internal diameter D_i	10 mm
Maximum stroke Δx	3 mm
Bellow mass m_{bellow}	2 g
Stiffness s	5000 N/m

Table 5.1: Bellow parameters of practical design

Component	Mass [g]
Actuator body	0.6
Exhaust spring	0.5
O-ring	0.01
Fuel injection module substrate	0.02
Bellow	2.0
Other	0.1
Total	3.2

Table 5.2: Mass distribution of the actuator

stroke Δx of 3 mm was estimated for a bellow with a length of 10 mm. It is assumed that this bellow weighs 2 grams and has a stiffness of 5000 N/m. Both of these estimations are based on scaling analysis of the smaller bellow used in the measurement setup, as well as inspection of off-the-shelf metallic bellows of comparable size.

5.4. A PRACTICAL ACTUATOR DESIGN

To identify the mass of the other components of the actuator, a practical actuator design is generated that includes an aluminum body, silicon injection module substrate and steel exhaust spring. The actuator body (red), exhaust spring (yellow) and injection module substrate (purple) are depicted in Figure 5.1 and 5.2. The bellow with aforementioned dimensions is also depicted in this figure, visualised in blue. Including the bellow, the actuator weighs approximately 3.2 grams, as can be seen in Table 5.2. This table gives the mass distribution for the actuator system proposed.

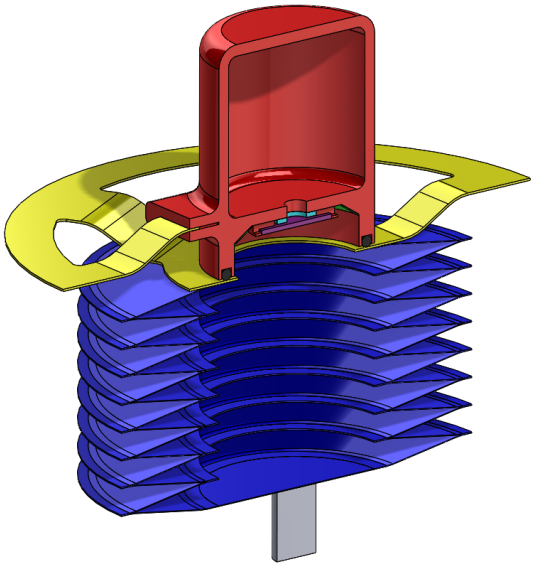

Figure 5.1: Visualisation of the actuator design in CAD (cross-section)

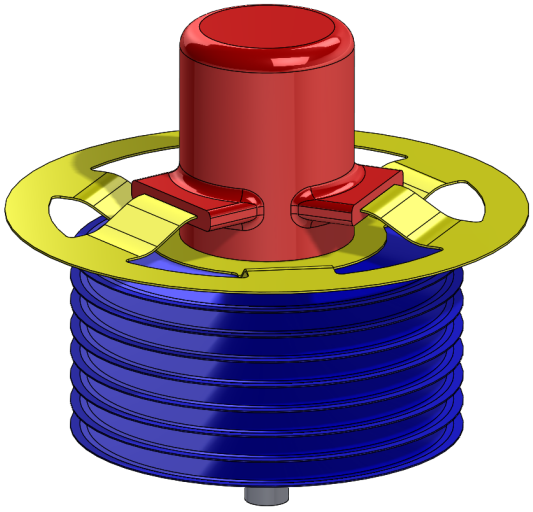

Figure 5.2: Visualisation of the actuator design in CAD (isometric view)

5.5. OTHER PARAMETER CONSIDERATIONS

In this section, it is described how the other parameters as m, b, V_f are determined, which is done by logic rather than extensive model analysis.

The equivalent load mass m, which is actually determined by the wing mass, wing length and geometrical advantage of the actuator-wing transmission, is chosen such to comply with the frequency requirement.

The damping coefficient of the load b, which is effectively determined by the wing area, wing length, the drag coefficient of the wing and the transmission ratio, influences the power output of the system to a certain extent. It may seem self-evident that increasing the damping coefficient will lead to more output power.

However, this is only true to a certain extent. As damping coefficient b is further increased the system becomes eventually critically damped, which obstructs the resonance motion of the system and deteriorates the output power. Therefore, a damping coefficient is determined in an iterative manner and set to a value which is close to optimal.
The fuel injected per cycle is not a free parameter, but merely a parameter that follows from the choice of the bellow geometry, damping and heat loss of the system. This is further explained. To maximize the work performed by the gas, the amplitude of the resonance motion should be at the limit of maximum and minimum bellow deformation. The fuel injected per cycle determines the amplitude of vibration directly. Too much fuel injection will result in exceeding the deformation limits of the bellow, however decreasing the fuel injection will lead to non-optimal use of the available bellow stroke. Therefore, the fuel injected has to be chosen such that the amplitude of the resonance motion is kept at the bellow limit.
The necessary fuel to be injected to keep the resonance motion at the required amplitude is highly dependent on the heat loss coefficient. A higher heat loss coefficient will lead to decreased average pressure over the expansion stroke, decreasing the output work and thus leading to a decrease in amplitude of vibration. Consequentially, to compensate for this, the fuel injected per cycle should be increased to keep the resonance motion of the system at maximum amplitude. This significantly reduces the conversion efficiency of the system.
The exhaust valve parameters as exhaust valve stiffness and pretension are chosen such that the exhaust valve is opened a fraction before top piston position, to maximize the length of the pressurized expansion stroke.

5.6. PERFORMANCE ANALYSIS

Based on the bellow design and aforementioned parameter considerations, the model response is evaluated for different heat loss coefficients h. The heat loss coefficients that are assumed are described in Table 5.3. It should be noted that the minimum heat loss coefficient h of 0.1 W/K is the estimated minimum heat loss coefficient of the bellow used in previous measurement setup. The resulting pressure-volume characteristics are visualised in Figure 5.3.

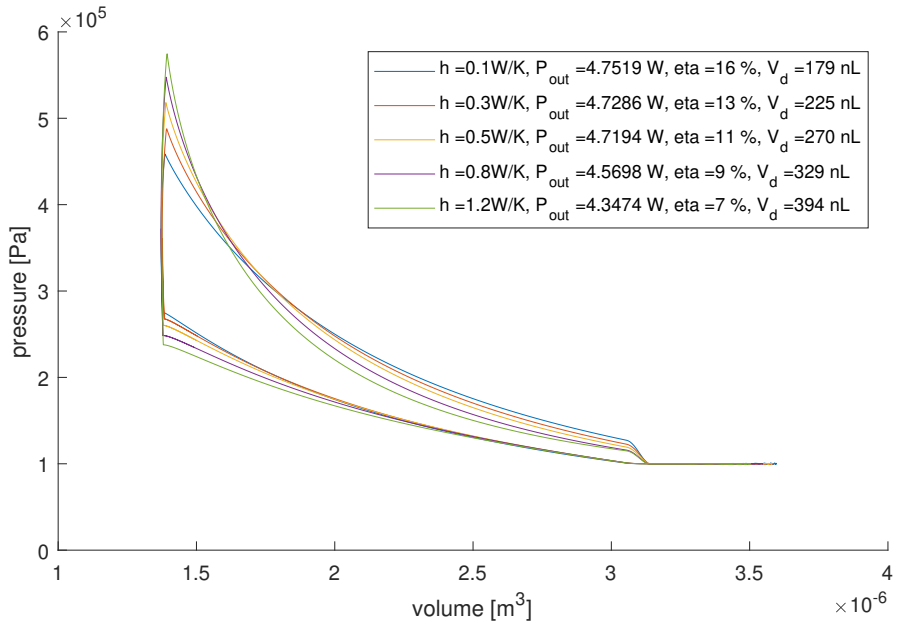

Figure 5.3: Pressure-volume response of a practical actuator design with bellow geometry and stiffness as is described in Table 5.1, for different heat loss coefficients.

What can be concluded is that for higher heat loss coefficients, the required fuel volume per cycle needed is higher. As can be seen in the figure, an increased fuel volume per cycle leads to increased peak pressure, but a faster pressure decrease. The power output stays approximately constant for different heat loss coefficients, but the efficiency reduces significantly for increasing heat loss. The resulting fuel volume, output power and efficiency are given in Table 5.3.

Heat loss coefficient [W/K]	Fuel volume [nL]	Output power [W]	Efficiency [%]
0.1	179	4.8	16
0.3	225	4.7	13
0.5	270	4.7	11
0.8	329	4.6	9
1.2	394	4.3	7

Table 5.3: Performance estimations for different heat loss coefficients

The calculated power output and efficiency are compared with the power-to-weight requirement. First, the power-to-weight ratio of the actuator is obtained by dividing the modelled output power with the total actuator mass (Table 5.2). The result is depicted in Figure 5.4, for different heat loss coefficients.

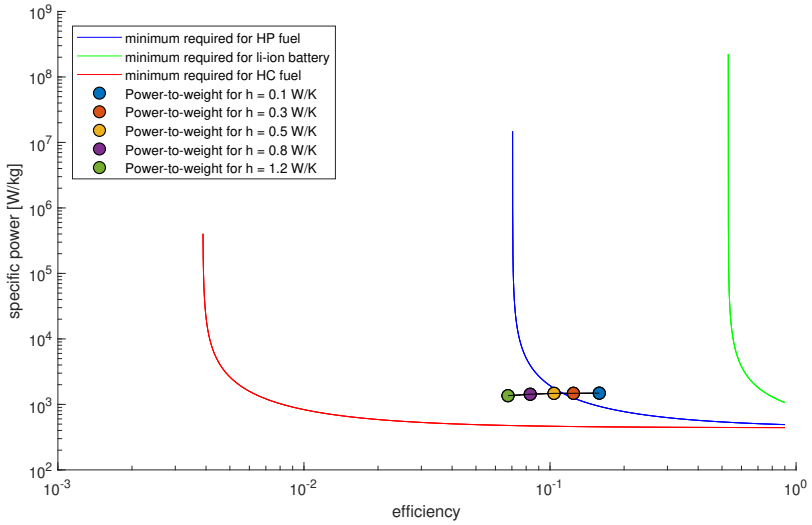

Figure 5.4: Power-to-weight requirement for a FWMAV actuator in order to fly in excess of 10 minutes, compared with the power-to-weight data of the proposed design

What can be concluded from Figure 5.4, is that the heat loss coefficient is decisive. If a heat loss coefficient of 0.3 W/K or less is achieved for the practical actuator design proposed, the power-to-weight requirement for a flight endurance of 10 minutes is fulfilled.

5.7. RECOMMENDATIONS

It should be noted that the minimum expected heat loss coefficient for the bellow used in the measurement setup, which has a surface area approximately 4 times smaller than proposed bellow, is 0.1 W/K and that a heat loss coefficient of 0.3 W/K or less is required. Further research should address the heat loss problem of the thin-walled expansion chamber. It is recommended to investigate thermal insulation of the chamber, either by careful material choice or sophisticated design solutions like double-walled bellows.
Besides addressing the heat loss problem, it is key to investigate if mechanical characteristics of the bellow (L=10mm, D_o=20mm, D_i=10mm, Δx=3mm, m_{bellow}=2g, s=5000N/m) can be achieved. Moreover, the analysis conducted in this chapter motivates further study of compliant hollow structures that have maximum internal volume change.

6

CONCLUSION

By a detailed conceptual study, this study motivates that a chemical actuator with a compliant expansion chamber, passive exhaust valve and electrowetting-based fuel injection would be a suitable actuator design choice to support 10 minutes of FWMAV flight endurance.
The advantages of the compliant expansion chamber are that it mitigates the leakage and friction problem completely, compared to conventional miniature piston-cylinder engines. The periodically varying tension force of the bellow expansion chamber can be exploited to open an exhaust valve, leading to an exhaust valve that requires no external control or power. This makes the exhaust valve to operate in an autonomous manner, where only the correct pretension setting of the exhaust spring is required.
The combination of the hydrogen peroxide as fuel and EWOD as fuel delivery concept, leads to a design that has low power requirements and has simple mechanical complexity. Moreover, the catalyst reaction of hydrogen peroxide mitigates the quenching issue, found in miniature hydrocarbon combustion engines, completely.

For clarity, we summarize the main conclusions of Chapter 3 and 4. The compliant expansion chamber with integrated passive exhaust valve is designed, built and successfully validated in a measurement setup that uses compressed air as source of pressurization. The experiments conducted prove the expansion chamber and exhaust valve concept, since the passive valve is being pulled open based on bellow deformation, and is capable of performing full pressure relief within one opening stroke. By setting the pretension of the exhaust valve spring, the exhaust opening point can be regulated to a desired bellow deformation amplitude.
An actuator model is constructed to predict this displacement dependent gas release behaviour of the exhaust valve. Moreover, this model can predict the displacement behaviour and power output of the actuator, as well as the time-varying pressure and temperature of the gas in the bellow cavity. The actuator model is validated against pressure and displacement measurements, and can predict the displacement and pressure response as well as power output within 10 % accuracy. Further research has to be conducted to predict the heat loss through the bellow wall.
The actuator model is expanded by a chemical model to determine the model response as a function of the hydrogen peroxide fuel intake. As a result, the conversion efficiency of the actuator can be modelled. The model estimates that a fuel volume of 28 nL hydrogen peroxide is necessary to power the experimental actuator developed in Chapter 3. Future research has to be conducted to verify if reaction time of the hydrogen peroxide catalyst reaction for this fuel volume range can be reduced to a fraction of the 33 ms cycle time. This study also recommends that in future experimental work, a hydrogen peroxide fuel delivery module and catalyst are implemented into the proposed compliant expansion chamber, to experimentally validate the functioning of the full system.
The fuel transport from reservoir to catalyst is modelled by analysing the displacement dependent EWOD driving force. The droplet trajectory model indicates that a 7 nL droplet can be transported over a linear electrode array of 16 400x200 μm (3.2 mm length) within 7 ms. Based on the droplet trajectory model, it is described how the electrodes should be actuated as a function of time to maximize the electrowetting-force at every position of the linear electrode array. This time-varying electrode switching rate leads to superior droplet velocity, compared to electrode switching at a constant rate. It is recommended to experimentally validate this droplet trajectory in future research, as well as experimentally characterizing high frequency (>30 Hz) droplet-reservoir splitting. Despite the fact that experimental droplet transport was not achieved in this research, the developed droplet transport model suggests that a set of compact injection modules can deliver sufficient hydrogen peroxide fuel volume to pressurize a miniature chemical actuator.

Finally, this study concludes that the chemical actuator design proposed is a viable option to power FWMAV that strives for a flight endurance of 10 minutes. It is deemed that the mass of actuator components, includ-

ing the bellow, actuator body, injection modules, exhaust spring and O-ring, can be designed to a mass of approximately 3.2 grams. If this is reached, the model calculates that a bellow with parameters (L=10mm, D_o=20mm, D_i=10mm, Δx=3mm, m_{bellow}=2g, s=5000N/m, h = 0.3 W/K) will fulfill power-to-weight requirement and thus support flight endurance in excess of 10 minutes. This would result in an actuator with an efficiency of 13 %, power output of 4.7W and a fuel consumption of 225 nL hydrogen peroxide (95% mass fraction) per cycle.

It is recommended that in further research, it is investigated if it is possible to design and manufacture a bellow with these design specifications. To further increase power output, further study of compliant hollow structures that can support high internal volume change would be insightful. Besides the mechanical characteristics of the expansion chamber, special attention has to be given to address the heat loss problem of the thin-walled expansion chamber design. Correct thermal insulation of the chamber should be addressed, either by careful material choice or sophisticated design solutions like double-walled bellows.
All in all, the proposed miniature chemical actuator with a compliant expansion chamber, passive exhaust valve and electrowetting-based fuel injection is expected to be a promising contender to increase the flight endurance of FWMAV. Moreover, it would be a suitable actuator for other small-scale energy generation applications where a high power-to-weight ratio is key.

BIBLIOGRAPHY

[1] Aichlmayr, H. T., Kittelson, D. B., & Zachariah, M. R. (2002). Design Considerations , Modeling , and Analysis of Micro-Homogeneous Charge Compression Ignition Combustion Free-Piston Engines.

[2] Annen, K. D., Stickler, D. B., & Woodroffe, J. (2003). Linearly-oscillating miniature internal combustion engine (mice) for portable electric power. *Aerospace Sciences Meeting and Exhibit*, (41), 1–9.

[3] Banerjee, A. N., Qian, S., & Joo, S. W. (2011). High-speed droplet actuation on single-plate electrode arrays. *Journal of Colloid and Interface Science*, *362*(2), 567–574.

[4] Barth, E. J., Gogola, M. A., Wehrmeyer, J. A., & Goldfarb, M. (2002). The design and modeling of a liquid-propellant-powered actuator for energetically autonomous robots. *ASME International Mechanical Engineering Congress and Exposition, Proceedings*, (pp. 917–923).

[5] Barth, P. W. (1995). Silicon microvalves for gas flow control. *International Conference on Solid-state Sensors and Actuators*, *8*, 276–279.

[6] Berry, S., Kedzierski, J., & Abedian, B. (2007). Irreversible electrowetting on thin fluoropolymer films. *Langmuir*, *23*(24), 12429–12435.

[7] Berthier, J., Dubois, P., Clementz, P., Claustre, P., Peponnet, C., & Fouillet, Y. (2007). Actuation potentials and capillary forces in electrowetting based microsystems. *Sensors and Actuators, A: Physical*, *134*(2), 471–479.

[8] Bhattacharjee, B. (2012). Study of Droplet Splitting in an Electrowetting Based Digital Microfluidic System. (September), 171.

[9] Bolsman, C. T. (2010). *Flapping wing actuation using resonant compliant mechanisms*.

[10] Burugupally, S. P. (2014). Development of a small scale resonant engine for micro and mesoscale applications.

[11] Burugupally, S. P., & Weiss, L. (2018). Power generation via small length scale thermo-mechanical systems: Current status and challenges, a review. *Energies*, *11*(9), 12–15.

[12] Chakraborty, I., Tang, W. C., Bame, D. P., & Tang, T. K. (2000). MEMS micro-valve for space applications. *Sensors and Actuators, A: Physical*, *83*(1), 188–193.

[13] Chang, J. H., & Pak, J. J. (2011). Twin-plate electrowetting for efficient digital microfluidics. *Sensors and Actuators, B: Chemical*, *160*(1), 1581–1585.

[14] Chen, S., Lu, S., Liu, Y., Wang, J., Tian, X., Liu, G., & Yang, Z. (2016). A normally-closed piezoelectric micro-valve with flexible stopper. *AIP Advances*, *6*(4).

[15] Chevalliot, S., Kuiper, S., & Heikenfeld, J. (2012). Experimental validation of the invariance of electrowetting contact angle saturation. *Journal of Adhesion Science and Technology*, *26*(12-17), 1909–1930.

[16] Cho, S. K., Moon, H., & Kim, C. J. (2003). Creating, transporting, cutting, and merging liquid droplets by electrowetting-based actuation for digital microfluidic circuits. *Journal of Microelectromechanical Systems*, *12*(1), 70–80.

[17] Christensen, H. I., & Khatib, O. (2017). *Progress on Pico Air Vehicles*, vol. 100.

[18] Dahm, W. J., Ni, J., Mijit, K., Mayor, R., Qiao, G., Benjamin, A., Gu, Y., Lei, Y., & Papke, M. (2002). Micro internal combustion swing engine (MICSE) for portable power generation systems. *AIAA Aerospace Sciences Meeting and Exhibit*, (40).

[19] Davidovic, D., Piñon, J., Burnett, E. F., & Srebric, J. (2012). Analytical procedures for estimating airflow rates in ventilated, screened wall systems (VSWS). *Building and Environment*, *47*(1), 126–137.

[20] de Croon, G., Perçin, M., Remes, B., Ruijsink, R., & De Wagter, C. (2016). *The DelFly*. Springer.

[21] Engel, T. (2014). *Physical Chemistry*, vol. 20.

[22] Farrell Helbling, E., & Wood, R. J. (2018). A Review of Propulsion, Power, and Control Architectures for Insect-Scale Flapping-Wing Vehicles. *Applied Mechanics Reviews*, *70*(1), 1–9.

[23] Floreano, D., & Wood, R. J. (2015). Science, technology and the future of small autonomous drones. *Nature*, *521*(7553), 460–466.

[24] Fobel, R., Fobel, C., & Wheeler, A. R. (2013). DropBot: An open-source digital microfluidic control system with precise control of electrostatic driving force and instantaneous drop velocity measurement. *Applied Physics Letters*, *102*(19).

[25] Gerdes, J. W., Gupta, S. K., & Wilkerson, S. (2012). A review of bird-inspired flapping wing miniature air vehicle designs. *Journal of Mechanism and Robotics*, *4*(2).

[26] Glynne-Jones, P., Coletti, M., White, N. M., Gabriel, S., & Bramanti, C. (2008). A feasibility study on using inkjet technology, micropumps, and MEMs as fuel injectors for bipropellant rocket engines. *44th AIAA/ASME/SAE/ASEE Joint Propulsion Conference and Exhibit*, (pp. 1–15).

[27] Groen, M. (2015). *Microvalves for precise dosing*.

[28] Gupta, H. (2006). *Fundamentals of Internal Combustion Engine*.

[29] Guzman, L., Miotello, A., Checchetto, R., & Adami, M. (2002). Ion beam-induced enhanced adhesion of gold films deposited on glass. *Surface and Coatings Technology*, *158-159*, 558–562.

[30] Heywood, J. B., & Sher, E. (1999). *The two-stroke cycle engine : its development, operation, and design*. Philadelphia, PA: Taylor & Francis ;.

[31] Hooke, C. J., Hajihosseinloo, M. A., & Walton, D. (1989). Note on the discharge coefficients of annular orifices. *Aeronautical Journal*, *93*(925), 183–188.

[32] Hue P. Le (1998). Progress and Trends in Ink-jet Printing Technology. *Journal of Imaging Science and Technology*, *42*(1), 49–62.

[33] Huff, M. (1990). A pressure-Balanced Electrostatically Actuated Microvalve.

[34] Jang, L. S., Hsu, C. Y., & Chen, C. H. (2009). Effect of electrode geometry on performance of EWOD device driven by battery-based system. *Biomedical Microdevices*, *11*(5), 1029–1036.

[35] Johnstone, R. W. (2004). An Introduction to Surface-Micromachining. 1, (pp. 1–2). Kluwer Academic Publishers.

[36] Kawamura, Y., Fujisaki, Y., & Tanaka, S. (1994). Electrostatically Driven Gas Valve with High Conductance. *Journal of Microelectromechanical Systems*, *3*(2), 76–80.

[37] Keennon, M., Klingebiel, K., Won, H., & Andriukov, A. (2012). Development of the nano hummingbird: A tailless flapping Wing Micro Air Vehicle. *50th AIAA Aerospace Sciences Meeting Including the New Horizons Forum and Aerospace Exposition*, (January), 1–24.

[38] Klett, D. E., Afify, E. M., Srinivasan, K. K., & Jacobs, T. J. (2017). Internal combustion engines. *Energy Conversion, Second Edition*, *I*(36), 223–255.

[39] Lee, J., Kim, K., & Kwon, S. (2015). Fabrication and Performance Evaluation of a Micro Igniter Membrane Assembly for Mems Thruster Array.

[40] Lin, Y. Y., Welch, E. R., & Fair, R. B. (2012). Low voltage picoliter droplet manipulation utilizing electrowetting-on- dielectric platforms. *Sensors and Actuators, B: Chemical*, *173*, 338–345.

[41] Liu, D. K. C., Friend, J., & Yeo, L. (2010). A brief review of actuation at the micro-scale using electrostatics, electromagnetics and piezoelectric ultrasonics. *Acoustical Science and Technology*, *31*(2), 115–123.

[42] Liu, H., Dharmatilleke, S., Maurya, D. K., & Tay, A. A. (2010). Dielectric materials for electrowetting-on-dielectric actuation. *Microsystem Technologies*, *16*(3), 449–460.

[43] Lu, J. (2018).

[44] McGee, T. G., Raade, J. W., & Kazerooni, H. (2004). Monopropellant-driven free piston hydraulic pump for mobile robotic systems. *Journal of Dynamic Systems, Measurement and Control, Transactions of the ASME*, *126*(1), 75–81.

[45] Meckes, A., Behrens, J., Kayser, O., Benecke, W., Becker, T., & Müller, G. (1999). Microfluidic system for the integration and cyclic operation of gas sensors. *Sensors and Actuators, A: Physical*, *76*(1-3), 478–483.

[46] Mehrabian, H., & Feng, J. J. (2014). Auto-ejection of liquid drops from capillary tubes. *Journal of Fluid Mechanics*, *752*, 670–692.

[47] Meskers, A. (2010). High energy density micro-actuation based on gas generation by means of catalysis of liquid chemical energy.

[48] Miao, Y., Zuo, Z., Feng, H., Guo, C., Song, Y., Jia, B., & Guo, Y. (2016). Research on the Combustion Characteristics of a Free-Piston Gasoline Engine Linear Generator during the Stable Generating Process. *Energies*, *9*(8), 1–19.

[49] MicroChem (2015). SU-8 2000.5-2015 Permanent Epoxy Negative Photoresist, processing guidelines. (pp. 1–5).

[50] Nahar, M. M., Nikapitiya, J. B., You, S. M., & Moon, H. (2016). Droplet velocity in an electrowetting on dielectric digital microfluidic device. *Micromachines*, *7*(4), 1–16.

[51] Nikapitiya, N. Y. B., Nahar, M. M., & Moon, H. (2017). Accurate, consistent, and fast droplet splitting and dispensing in electrowetting on dielectric digital microfluidics. *Micro and Nano Systems Letters*, *5*(1).

[52] Oh, K. W., & Ahn, C. H. (2006). A review of microvalves. *Journal of Micromechanics and Microengineering*, *16*(5).

[53] Phan, H. V., & Park, H. C. (2019). Insect-inspired, tailless, hover-capable flapping-wing robots: Recent progress, challenges, and future directions. *Progress in Aerospace Sciences*, (August), 100573.

[54] Preetham, B. S., Anderson, M., & Richards, C. (2012). Modeling of a resonant heat engine. *Journal of Applied Physics*, *112*(12).

[55] Preetham, B. S., Anderson, M., & Richards, C. (2014). Mathematical modeling of a four-stroke resonant engine for micro and mesoscale applications. *Journal of Applied Physics*, *116*(21).

[56] Riofrio, J., & Barth, E. J. (2015). Experimental Assessment of a Free Elastic-Piston Engine Compressor with Experimental Assessment of a Free Elastic-Piston Engine Compressor with Separated Combustion Chamber.

[57] Samad, M. F., Kouzani, A. Z., Hosain, M. K., Magniez, K., Islam, M. S., Kaynak, A., Das, S., Alam, M. N., & Moghadam, A. A. (2015). Analysis of droplet mixing and splitting operations by a low actuation voltage electrowetting-on-dielectric device. *2014 4th International Conference on Engineering Technology and Technopreneuship, ICE2T 2014*, (4), 289–294.

[58] Sher, E., & Sher, I. (2011). Theoretical limits of scaling-down internal combustion engines. *Chemical Engineering Science*, *66*(3), 260–267.

[59] Sher, I., Levinzon-Sher, D., & Sher, E. (2009). Miniaturization limitations of HCCI internal combustion engines. *Applied Thermal Engineering*, *29*(2-3), 400–411.

[60] Shi, B., Yu, H., & Zhang, J. (2018). The effects of the various factors and the engine size on micro internal combustion swing engine (MICSE). *Applied Thermal Engineering*, *144*(August), 262–268.

[61] Song, J. H., Evans, R., Lin, Y. Y., Hsu, B. N., & Fair, R. B. (2009). A scaling model for electrowetting-on-dielectric microfluidic actuators. *Microfluidics and Nanofluidics*, *7*(1), 75–89.

[62] Sprague, S. B., Park, S. W., Walther, D. C., Pisano, A. P., & Fernandez-Pello, A. C. (2007). Development and characterisation of small-scale rotary engines. *International Journal of Alternative Propulsion*, *1*(2-3), 275–293.

[63] Thorncroft, G., Patton, J. S., & Gordon, R. (2007). Modeling compressible air flow in a charging or discharging vessel and assessment of polytropic exponent. *ASEE Annual Conference and Exposition, Conference Proceedings*.

[64] Van Blarigan, P., Paradiso, N., & Goldsborough, S. (1998). Homogeneous charge compression ignition with a free piston: A new approach to ideal otto cycle performance. *SAE Technical Papers*.

[65] van den Heuvel, H. (2015). Conceptual Development of a catalytic expansion actuator for a Resonating-body Flapping-wing Micro Air Vehicle.

[66] Van Der Wijngaart, W., Ask, H., Enoksson, P., & Stemme, G. (2002). A high-stroke, high-pressure electrostatic actuator for valve applications. *Sensors and Actuators, A: Physical*, *100*(2-3), 264–271.

[67] van Wageningen, T. (2012). Design analysis for a small scale hydrogen peroxide powered engine for a Flapping Wing Mechanism Micro Air Vehicle.

[68] Wang (2017). *Modeling, design and optimization of flapping wings for efficient hovering flight*.

[69] Wang, Z. J., Birch, J. M., & Dickinson, M. H. (2004). Unsteady forces and flows in low Reynolds number hovering flight: Two-dimensional computations vs robotic wing experiments. *Journal of Experimental Biology*, *207*(3), 449–460.

[70] White, F. (2011). Fluid Mechanics. *Technische Mechanik*, (pp. 385–416).

[71] Wood, R. J. (2008). The first takeoff of a biologically inspired at-scale robotic insect. *IEEE Transactions on Robotics*, *24*(2), 341–347.

[72] Wu, H., Dey, R., Siretanu, I., van den Ende, D., Shui, L., Zhou, G., & Mugele, F. (2020). Electrically Controlled Localized Charge Trapping at Amorphous Fluoropolymer–Electrolyte Interfaces. *Small*, *16*(2).

[73] Xia, C., Zhang, Z., Huang, G., Zhou, T., & Xu, J. (2018). A micro swing rotor engine and the preliminary study of its thermodynamic characteristics. *Energies*, *11*(10).

[74] Xu, X., Sun, L., Chen, L., Zhou, Z., Xiao, J., & Zhang, Y. (2014). Electrowetting on dielectric device with crescent electrodes for reliable and low-voltage droplet manipulation. *Biomicrofluidics*, *8*(6).

[75] Yang, X. (2001). A MEMS Valve for the MIT Microengine.

[76] Yang, X., Grosjean, C., & Tai, Y. C. (1999). Design, fabrication, and testing of micromachined silicone rubber membrane valves. *Journal of Microelectromechanical Systems*, *8*(4), 393–402.

[77] Yi, Z., Feng, H., Zhou, X., & Shui, L. (2020). Design of an Open Electrowetting on Dielectric Device Based on Printed Circuit Board by Using a Parafilm M. *Frontiers in Physics*, *8*, 1–10.

[78] Yobas, L., Huff, M. A., Lisy, F. J., & Durand, D. M. (2001). A novel bulk-micromachined electrostatic microvalve with a curved-compliant structure applicable for a pneumatic tactile display. *Journal of Microelectromechanical Systems*, *10*(2), 187–196.

[79] Zdunich, P., Bilyk, D., MacMaster, M., Loewen, D., DeLaurier, J., Kornbluh, R., Low, T., Stanford, S., & Holeman, D. (2007). Development and testing of the mentor flapping-wing micro air vehicle. *Journal of Aircraft*, *44*(5), 1701–1711.

[80] Zhang, S., Guo, Z., & Wang, J. (2009). Performance analysis of a 2-stroke micro free-piston swing engine. *Petroleum Science*, *6*(3), 313–318.

[81] Zhang, X., Mehra, A., Ayón, A. A., & Waitz, I. A. (2003). Igniters and temperature sensors for a micro-scale combustion system. *Sensors and Actuators, A: Physical*, *103*(1-2), 253–262.

[82] Zhou, R., Ye, Q., Li, H., Jiang, H., Tang, B., & Zhou, G. (2019). Experimental study on the reliability of water/fluoropolymer/ITO contact in electrowetting displays. *Results in Physics*, *12*, 1991–1998.

A

APPENDIX A

A.1. FLIGHT TIME ANALYSIS

To analyse the power usage of a FWMAV in flight, the following abstraction is made to deduce the simple wing dynamics, depicted in Figure A.1. The following assumptions are made:

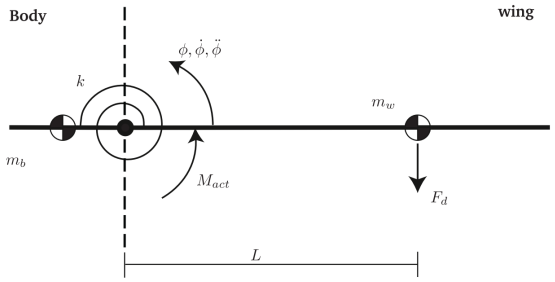

Figure A.1: Schematic of the wing model.

1. The wing mass m_w is insignificant compared to body mass m_b. Therefore, the linkage from the centre hing to m_b can be regarded fixed to ground and body motions are negelected.
2. The centre of mass as well as the centre of pressure of the aerodynamic drag force F_d on the wing are located at characteristic length L away from the centre hinge.
3. The wing is hinged on the body. Parallel to this hinge, a torsion spring with torsional stiffness k is connected.
4. The body exerts a moment M_{act} on the wing to maintain it's flapping motion and overcome drag forces.

The wing forces are modelled as the following [9]:

$$F_d = C_d * L^2 * \dot{\phi}^2 sgn(\dot{\phi}) \tag{A.1}$$

$$F_l = C_l * L^2 * \dot{\phi}^2 \tag{A.2}$$

Assuming the wings will flap in a sinus with amplitude A and in resonance frequency ω of the system, the required moment M_{act} can be calculated that will sustain hovering flight [9].

$$\phi = A * cos(\omega t) \tag{A.3}$$

$$M_{act} = 2m_t \frac{C_d}{C_l} Lgcos^2(\omega t) sgn(cos(\omega t)) \tag{A.4}$$

A.1.1. NO MASS REDUCTION EFFECT

Now, the average mechanical power is calculated, which is constant for batteries. This gives a requirement on the minimum mechanical output power of the actuator, which is apparently linear with vehicle mass m_t and linear with and aerodynamic constant α.

$$\bar{P} = \frac{8}{3\pi} \frac{C_d}{C_l} AL\omega g m_t = \alpha m_t \tag{A.5}$$

For batteries, which mass does not reduce during flight, the total energy is calculated as

$$E = \frac{\int_0^{\Delta t} \bar{P} dt}{\eta} = \frac{\bar{P}\Delta t}{\eta} \tag{A.6}$$

where η is the efficiency of the actuator. The minimum required power density p_{min} of the actuator can be calculated by rewriting the terms of the total mass m_t, where m_b is the body mass, m_a the actuator mass, m_b the remaining mass and e_f is the energy density of the battery.

$$m_t = m_b + m_a + m_e = m_b + \frac{\bar{P}}{p} + \frac{\bar{P}\Delta t}{\eta e_f} \tag{A.7}$$

$$p_{min} = \frac{\alpha}{1 - \frac{\alpha \Delta t}{\eta e_f} - \frac{m_b}{m_t}} \tag{A.8}$$

A.1.2. MASS REDUCTION EFFECT

For chemical energy carriers, mechanical output power can be decreased during flight, since the vehicle gets lighter by the sequential combustion of the fuel. The average mechanical power over each flapping cycle can be described by the following equation, where m_i is the initial vehicle mass.

$$\bar{P}(t) = \alpha \left[m_i - \int_0^t \frac{\bar{P(\tau)}}{e_f \eta} d\tau \right] \tag{A.9}$$

The solution of this differential equation is

$$\bar{P}(t) = \alpha m_i e^{-\frac{\alpha t}{\eta e_f}} \tag{A.10}$$

The mechanical work W done by the actuator is

$$W = \int_0^{\Delta t} \bar{P}(t) dt = m_i \eta e_f \left[1 - e^{-\frac{\alpha \Delta t}{\eta e_f}} \right] \tag{A.11}$$

By the same method as in equation A.7, the minimum required power density of the actuator to sustain a flight of Δt is

$$p_{min} = \frac{\alpha}{e^{-\frac{\alpha \Delta t}{\eta e_f}} - \frac{m_b}{m_i}} \tag{A.12}$$

In this study, a body mass fraction of 0.5 is assumed, identical to the Nano Hummingbird vehicle, which has the greatest endurance of all MAVs and PAVs under 20 grams [23]. Also, the aerodynamic efficiency c_d/c_l is assumed to be 0.15 for vehicles in this size range [9, 69].

A.2. SPECIFIC POWER FLIGHT TIME ANALYSIS

If the vehicle is power limited, the following equation describes the total weight of the vehicle.

$$m_t = m_b + m_a + m_e + c = m_b + \frac{\bar{P}}{p} + \frac{\bar{P}\Delta t}{\eta e_f} \tag{A.13}$$

Mass addition c is now added to the equation, describing the additional mass that the battery needs to include to cope with the power requirement. c can be calculated by:

$$c = \frac{P}{p_f} - \frac{E}{e_f} = \frac{\alpha m_t}{p_f} - \frac{\alpha m_t \Delta t}{e_f \eta} \tag{A.14}$$

where p_f is the specific power of the battery. The flight time is calculated by:

$$\Delta t = \eta e_f (\frac{1}{\alpha} - \frac{m_b}{m_t \alpha} - \frac{1}{p_a} - c) \tag{A.15}$$

However, c is dependent on Δt, hence this set of equations cannot be applied explicitly. So first an initial Δt is guessed before iteratively computing c and Δt until results are converged.

A.3. BELLOW PRESSURE AREA DERIVATION

To derive the effective bellow pressure area, a simplification of the bellow geometry is made, assuming triangular corrugations with inner diameter D_i, outer diameter D_o. A single corrugation consists of a double ring segment which hinges about O. The stiffness k_δ of a single corrugation is modelled as a spring connected between point A and point B in Figure A.2. The area of the upper ring with projected radial length l as well as the area of the lower ring of the corrugation is defined as A_c, calculated in Equation A.16. The stiffness k of the bellow of with N corrugations is related to k_δ as in Equation A.17. The vertical extension δ of a single corrugation is related to total deformation x as in Equation A.18.

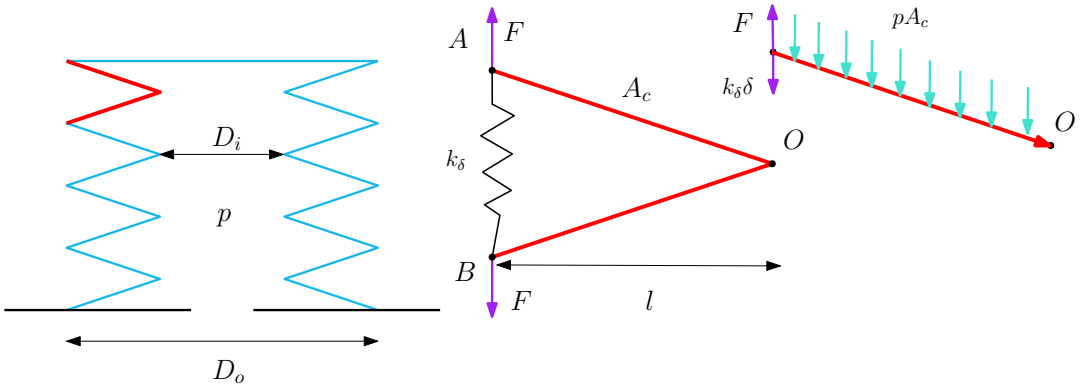

Figure A.2: Schematic of simplified bellow geometry

$$A_c = \frac{\pi}{4}(D_o^2 - D_i^2) \tag{A.16}$$

$$k_\delta = kN \tag{A.17}$$

$$\delta = \frac{x}{N} \tag{A.18}$$

The axial force F at the ring-shaped joints at A and B can be modelled as in Equation A.18.

$$F = p\frac{\pi}{4}D_o^2 \tag{A.19}$$

Static equilibrium is assumed and therefore the moment about rotation point O is set to zero, which leads to:

$$p\frac{\pi}{4}D_o^2 l = pA_c(\frac{1}{2}l) + (kN)(\frac{x}{N})l \tag{A.20}$$

Rearranging and substitution leads to the following general deformation equation, where the area $A = \frac{\pi}{8}(D_o^2 + D_i^2)$ can be extracted from.

$$p\frac{\pi}{8}(D_o^2 + D_i^2) = kx \tag{A.21}$$

A.4. β FITTING PROCEDURE

In this section, parameter β is determined by fitting Equation A.22 through all maxima $\hat{x}_{ub,j,q}$ of the free vibration response.

$$x_{ub} = \alpha e^{-\beta t} + \gamma \tag{A.22}$$

It is important to note that β is assumed to stay constant between the experiments, therefore a single β is sought accross all experiments. However, α_j and γ_j are varying, and therefore separately determined for each experiment. Thus, the following minimization procedure is performed.

$$\begin{aligned} \min_{\beta} \quad & f_\beta(\beta) = \sum_{j=1}^{n_j} \sum_{q=1}^{n_q} \left(\frac{x_{ub}(t_q, \beta, \alpha_j, \gamma_j) - \hat{x}_{ub,j,q}}{\hat{x}_0} \right)^2 \\ \text{subject to} \quad & \beta_{min} \leq \beta \leq \beta_{max} \end{aligned} \tag{A.23}$$

where j denotes the measurement number, n_j the amount of measurements, q the maxima number, n_q the amount of maxima and t_q the time of each maxima. The maxima value $\hat{x}_{ub,j,q}$ is the mean value of the three maximum measurement values around. The result and comparison with a typical measurement is depicted in Figure A.3. The solution for β is 9.06 1/s. It suggests less strong damping for smaller amplitudes.

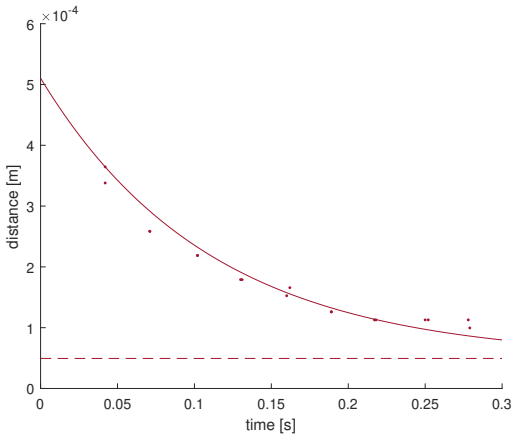

Figure A.3: Single fit which shows the typical discrepancy, caused by less strong damping for smaller amplitudes.

A.5. k_i AND V_{dead} FITTING PROCEDURE

k_i and V_{dead} are determined fy fitting the model response through the free vibration of the sealed cavity. Note that for each measurement j, $p_{i,j}$ is varying while a single k_i and V_{dead} are sought, since they do not vary across the different measurements. The mathematical formulation of the minimization problem performed is given below.

$$\begin{aligned} \min_{V_{dead},k_i} \quad & f_{vk}(V_{dead},k_i) = \sum_{j=1}^{n_j}\sum_{q=1}^{n_q}\left[w_x\left(\frac{x_j(t_q,V_{dead},k_i,p_{i,j})-\hat{x}_{j,q}}{\hat{x_0}}\right)^2 + w_p\left(\frac{p_j(t_i,V_{dead},k_i,p_{i,j})-\hat{p}_{j,q}}{\hat{p_0}}\right)^2\right] \\ \text{subject to} \quad & V_{dead,min} \le V_{dead} \le V_{dead,max} \\ & k_{i,min} \le k_i \le k_{i,max} \end{aligned} \tag{A.24}$$

Here j denotes the measurement number, n_j the amount of measurements, q denotes the index of a single measurement value, n_q the amount of samples per measurement. f_{vk} denotes the objective function to be minimized, $\hat{x}_{j,i}$ and $\hat{p}_{j,i}$ the measurement values. $\hat{x}_0 = 10^{-3}m$ and $\hat{p}_0 = 0.5 * 10^{-5}Pa$ are scaling values. The bounding values are $k_i i, min = 3.0 * 10^{-10}kg/Pa * s$, $k_{i,max} = 3.8 * 10^{-10}kg/Pa * s$, $V_{dead,min} = 2.3 * 10^{-7}m^3$ and $V_{dead,max} = 2.6 * 10^{-7}m^3$. The bounding values of k_i are guessed and updated iteratively. The bounding values for V_dead are estimated based on CAD data. The solution to problem A.24 is found to be $V_{dead} = 2.38 * 10^{-7}m^3$ and $k_i = 3.11 * 10^{-10}kg/Pa * s$ and is compared with experimental data in Figure A.4.

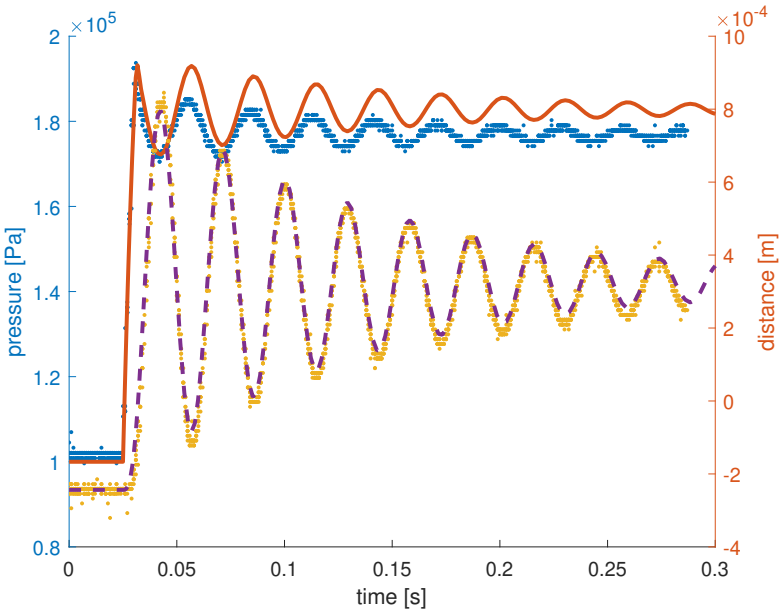

Figure A.4: Model vs. measurement for a typical single pulse experiment. Setting variables used: $p_i = 2.171$ bar, $d_{pt} = 2.43$ mm, $t_{open} = 6$ ms

A.6. CATALYST REACTION MASS FLOW ANALYSIS

To enforce that inlet flow of oxygen and water vapour mixture is only enabled around bottom position, the inlet flow function is set to be a product of the following functions $u_1(\dot{x})$ and $u_2(\ddot{x})$ as indicated in Figure A.5a and A.5b respectively. The threshold velocity $\dot{x}_i$ that determines the velocity window around bottom piston should be set such that the inlet flow has duration t_i. If it is assumed that $\ddot{x}$ is constant during this event, the threshold velocity $\dot{x}_i$ can be deduced from Figure A.5c as in Equation A.25. The final mass flow function $\dot{m}_i$ is given in Equation A.26. Checking of the accumulated mass flow $\int \dot{m}_i dt$ indicates correct mass addition of constant m_i every cycle.

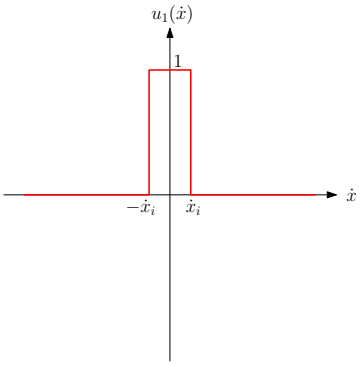

(a) Logistic function that defines velocity window where the inlet flow should be enabled.

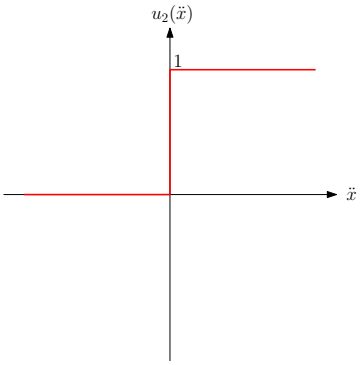

(b) Logistic function that defines acceleration window where the inlet flow should be enabled, effectively leading to inlet mass flow only at bottom piston position

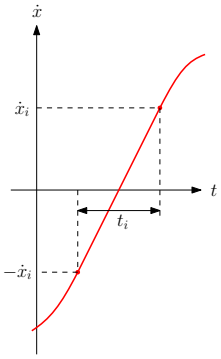

(c) Piston velocity, indicating velocity window of duration t_i

$$\dot{x}_i = \frac{\ddot{x} t_i}{2} \tag{A.25}$$

$$\dot{m}_i = \frac{m_i}{t_i} \frac{1}{1 + e^{g_1(|\dot{x}| - \dot{x}_i)}} \frac{1}{1 + e^{-g_1 \ddot{x}}} \tag{A.26}$$

The medium specific gas constant R is updated in Equation A.27 by assuming a gas mixture of water vapour and oxygen with applicable mass fractions [21]. The updated R differs 8% from the air gas constant.

$$R = \frac{\bar{R}}{M_{mixture}} = \bar{R} \left[\frac{m_{H_2O}}{m_{H_2O} + m_{O_2}} \frac{1}{M_{H_2O}} + \frac{m_{O_2}}{m_{H_2O} + m_{O_2}} \frac{1}{M_{O_2}} \right] \tag{A.27}$$

Identically, the specific heat values c_p and c_v should be updated for the mixture concerned here as is described in the following equations.

$$c_p = \frac{n_{H_2O}}{n_{H_2O} + n_{O_2}} c_{p,H_2O} + \frac{n_{O_2}}{n_{H_2O} + n_{O_2}} c_{p,O_2} \tag{A.28}$$

$$c_v = \frac{n_{H_2O}}{n_{H_2O} + n_{O_2}} c_{v,H_2O} + \frac{n_{O_2}}{n_{H_2O} + n_{O_2}} c_{v,O_2} \tag{A.29}$$

A.7. MODEL RESULTS FOR HYDROGEN PEROXIDE CATALYST REACTION

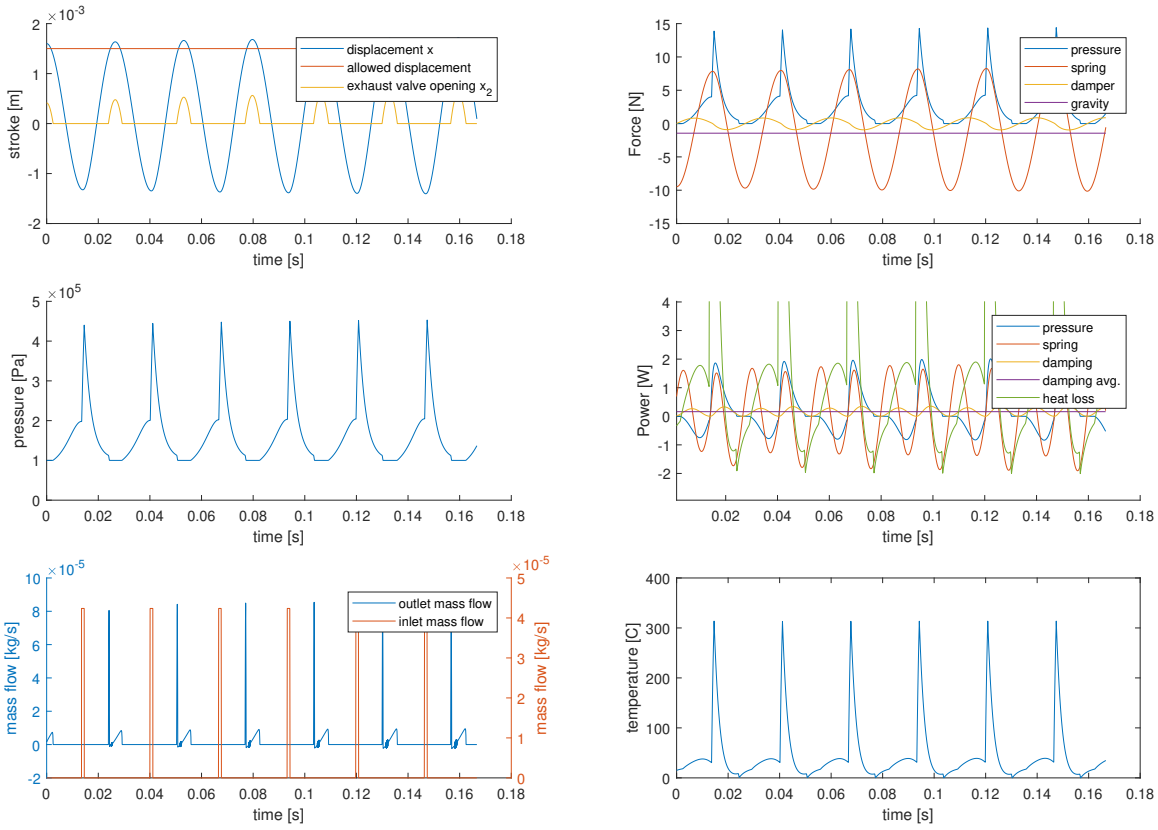

Figure A.6: Model results for the following variables: $V_f = 28nL, h = 0.1W/K, V_{dead} = 0m^3$ and bellow geometry of previous chapter

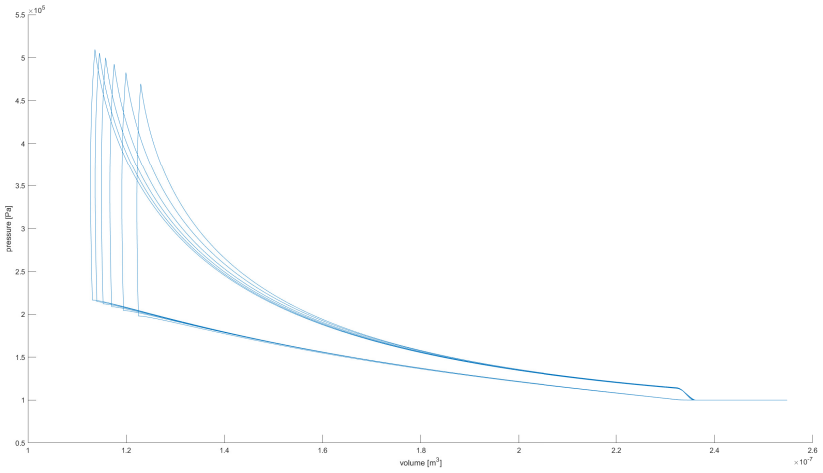

Figure A.7: Pressure-volume relation of the model evaluation done in Figure A.6.

B

APPENDIX B

B.1. DESIGN OPTION TREE (DOI)

B.1.1. EXPANSION CHAMBER DOI

The design option tree for the expansion chamber subsystem in given in figure B.1.

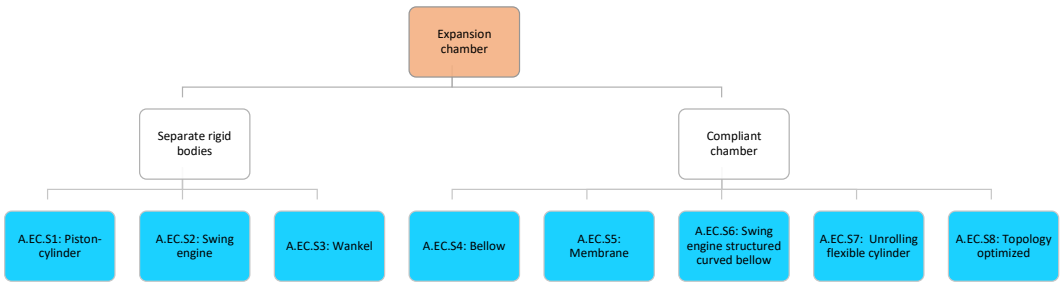

Figure B.1: The design option tree for the expansion chamber subsystem. The orange block denotes the subsystem, the white blocks the solutions categories and the cyan block the concept solutions.

B.1.2. FUEL EXHAUST DOI

The design option tree for the expansion chamber subsystem in given in figure B.2.

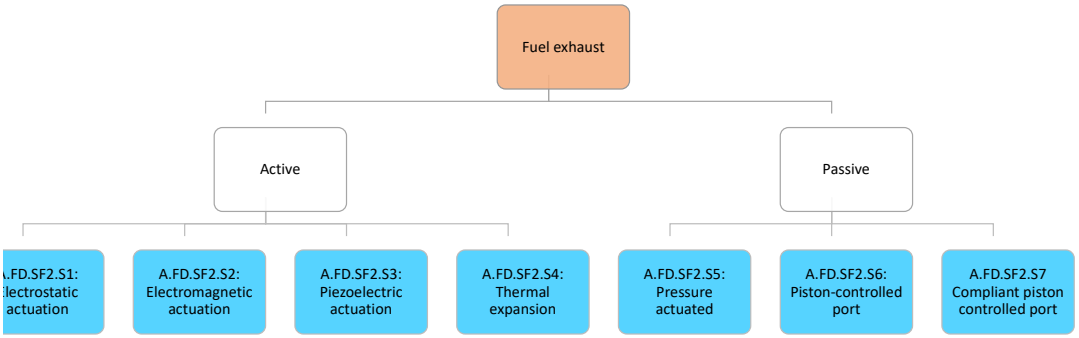

Figure B.2: The design option tree for the fuel exhaust subsystem. The orange block denotes the subsystem, the white blocks the solutions categories and the cyan block the concept solutions.

B.1.3. FUEL DELIVERY DOI

The design option tree for the expansion chamber subsystem in given in figure B.3.

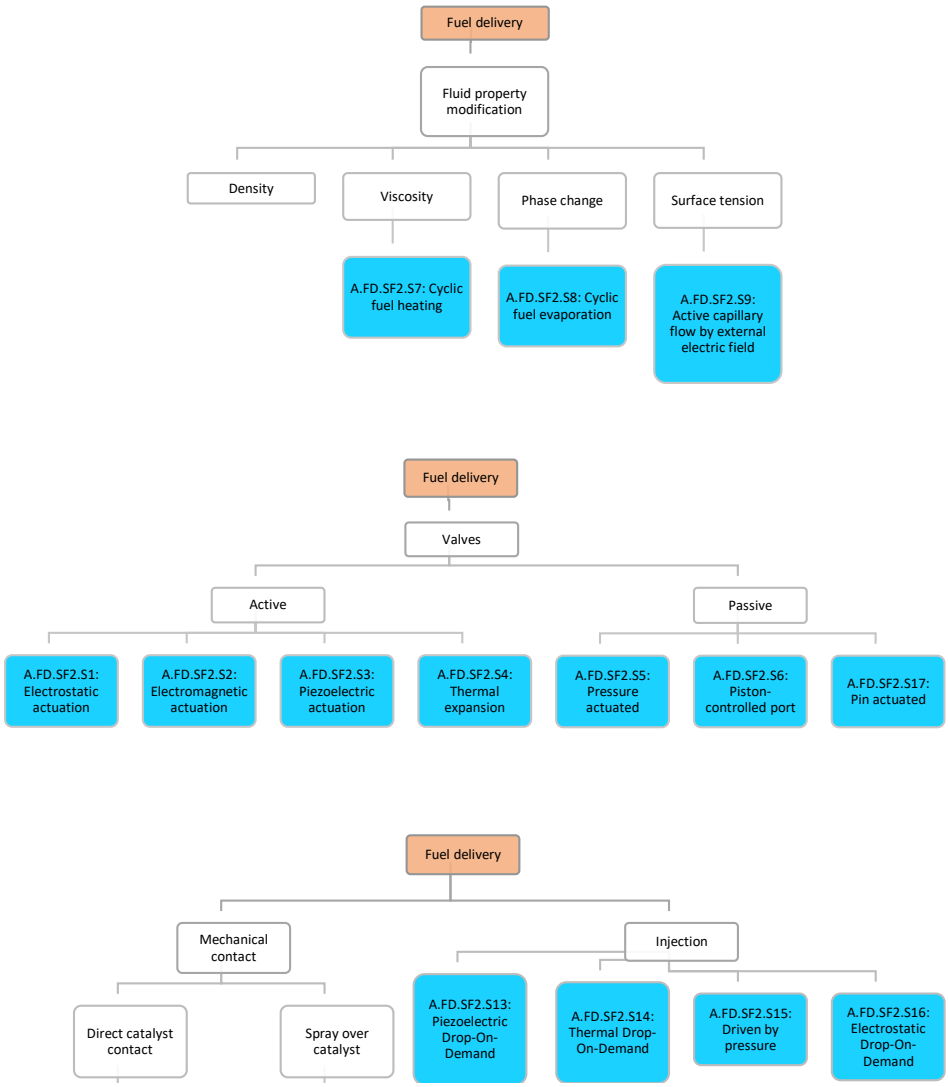

Figure B.3: The design option tree for the fuel delivery subsystem. The orange block denotes the subsystem, the white blocks the solutions categories and the cyan block the concept solutions.

B.1.4. IGNITION MECHANISM DOI

The design option tree for the ignition mechanism subsystem in given in figure B.4.

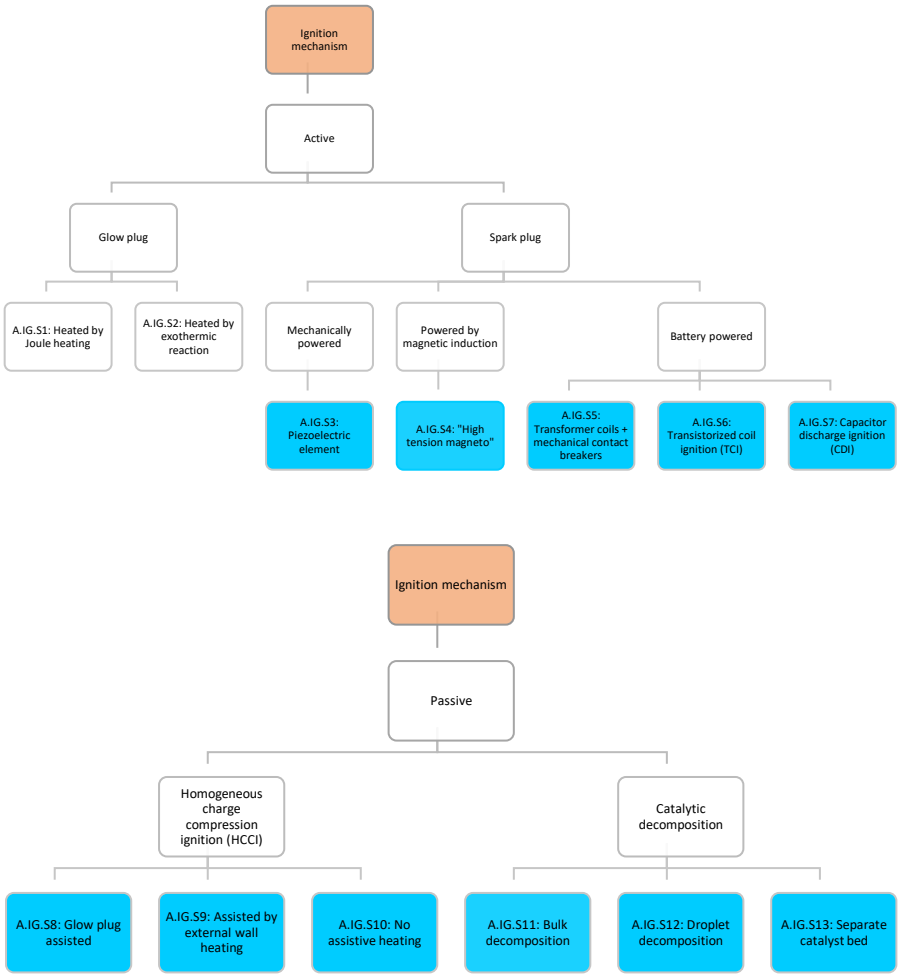

Figure B.4: The design option tree for the ignition mechanism subsystem. The orange block denotes the subsystem, the white blocks the solutions categories and the cyan block the concept solutions.

B.2. CONCEPT OVERVIEW

In the table B.1, a concept overview is given including references to literature if available. Non-eliminated concepts are depicted in bold. For eliminates concept, an elimnation reason is given.

B.3. CONCEPT COMPARISON TABLES

In table B.2, B.3, B.4, B.5 a detailed concept comparison is given for the expansion chamber, exhaust valve, fuel delivery and ignition mechanism respectively.

Number	Description	Ref.	Elimination reason
	Expansion chamber		
A.EC.S1	Conventional piston-cylinder engine without sealing rings	[2, 65]	Excessive leakage between cylinder and piston
A.EC.S2	Swing engine	[18, 60]	Excessive leakage between swing arm and cavity body
A.EC.S3	Wankel engine	[38, 73]	Has more clearance gap than conventional piston-cylinder concept
A.EC.S4	**Single bellow**	[10, 54]	
A.EC.S5	**Membrane**	[56]	
A.EC.S6	Swing engine curved bellow	-	Complex to assemble and manufacture, curved bellows not available off-the-shelf
A.EC.S7	Unrolling flexible cylinder	[67]	Complex to manufacture and assemble, not robust, high strains
A.EC.S8	**Topology optimized compliant expansion chamber**	-	
	Exhaust valve		
A.FE.S1	**Electrostatic actuation, stroke powered by combustion pressure**	[33, 66]	
A.FE.S2	Electromagnetic actuation	[27, 52]	High power consumption compared to electrostatic
A.FD.S3	Piezoelectric actuation	[12, 14]	High voltages needed
A.FE.S4	Thermal expansion	[5, 27]	High power consumption compared to electrostatic
A.FE.S5	**Pressure-pin actuated**	-	
A.FE.S6	Piston-controlled port	[30]	Without sealing rings excessive leakage
A.FE.S7	**Compliant piston-controlled port**	-	
	Fuel delivery		
A.FD.S1	Electrostatically actuated valve	[36, 75]	Small air gaps required limits orifice size
A.FD.S2	Electromagnetically actuated valve	[27, 52]	Limited work density, unfavorable scaling of electromagnetic forces
A.FD.S3	Piezoelectrically actuated valve	[12, 14]	High voltages needed
A.FD.S4	Thermal expansion valve	[5, 27]	High power consumption
A.FD.S5	**Pressure actuated valve (Reed valve)**	[30]	
A.FD.S6	Piston-controlled port	[30]	Excessive leakage without piston sealing rings
A.FD.S7	Fuel viscosity modification by heating (thermocapillary)	[52, 74]	Complex, slower and more power consumption than electrocapillary
A.FD.S8	**Cyclic fuel evaporation by heating**	-	
A.FD.S9	**Active capillary droplet delivery by EWOD**	[3, 40]	
A.FD.S10	Contact betw. moving catalyst and accumulated fuel droplet	[65]	Fuel contact difficult to predict, not repeatable
A.FD.S11	Contact betw. moving catalyst and accumulated fuel film	[65]	Fuel contact difficult to predict, not repeatable
A.FD.S12	Fuel is sprayed over catalyst by pin that penetrates a fuel filled tube	[65]	No reliable dosing
A.FD.S13:	**Piezoelectric Drop-On-Demand**	[32]	
A.FD.S14:	Thermal Drop-On-Demand	[32]	High power consumption due to bubble evaporation
A.FD.S15:	Electromagnetic Drop-on-demand	[32]	Unfavorable scaling of electromagnetic forces
A.FD.S16:	**Electrostatic Drop-On-Demand + combustion pressurized**	[32, 33]	
A.FD.S17:	**Pin actuated**	-	
	Ignition mechanism		
A.IG.S1	**Glow plug heated by Joule heating**	[39, 81]	
A.IG.S2	Plug heated by exothermic reaction	-	Extra chemical needed, unnecessary complex
A.IG.S3	Spark plug powered by piezoelectric element upon compression	[28]	Complex
A.IG.S4	Spark plug powered by magnetic induction ("high tension magneto") with transformer	[28]	Complex, heavy windings
A.IG.S5	Spark plug powered by battery with transformer, switched by mechanical contact breakers	[28]	Heavier and less robust than TCI
A.IG.S6	Spark plug powered by battery, switched by transistors (TCI)	[28]	Effectively the same as CDI, but is not able to generate high voltages for spark
A.IG.S7	**Spark plug powered by capacitor (CDI)**	[28]	
A.IG.S8	**Homogeneous charge compression ignition (HCCI)**	[1, 64]	
A.IG.S11	Catalytic bulk decomposition	[65]	Low surface to volume ratio than droplet, limited reaction time
A.IG.S12	**Catalytic droplet decomposition**	[47, 65]	
A.IG.S13	Catalytic decomposition in separate catalyst bed	[4, 44]	Flow restriction between reaction chamber leads to unnecessary pressure loss and time delay

Number		Mass		Efficiency		Reliability		Manufacturability		Complexity	Academic relevance	
A.EC.S4	+	Thin walled design has very little mass	++	Enough design variables to achieve sufficient compliance. Relatively little energy is converted to strain energy of expansion chamber	+	Possibly fragile design. Possibility to verify analytically. Less buckling issues then A.EC.S8. Proven manufacturing methods. Yielding or breakage could be problem due to high strains	+	Edge welding or electrodeposition possible. Medium lead times	o	Amount of design variables is relatively few. Parasitic vibrations of bellow should be thoroughly studied.	o	Novel to use compliant structures as expansion chamber
A.EC.S5	+	Thin membrane has very little mass	-	Limited design variables to achive desired compliance. Combustion energy is partially converted to "balloon inflation" instead of wing movement	+	Use of more compliant materials might suffer from thermal issues and too much damping. Parasitic motions and fragility is limited. Predicatable	++	Simple to manufacture with lasercutting. Ideal joining method has to be studied. Small lead times	+	Amount of free variable of single circular membrane is very limited. Deformations are predictable and possible to solve analytically	o	Novel to use compliant structures as expansion chamber
A.EC.S8	++	Can be optimized for mass in more extent than membrane and bellow	++	Enough design variables to achieve sufficient compliance. Relatively little energy is converted to strain energy of expansion chamber. Lift maximization possible]	-	Possibly fragile design. Difficult to verify design analytically.	–	Organic topology difficult to manufacture with conventional manufacturing methods as cutting or welding of sheets. Electrodeposition might be possible. Long lead times	–	Complex, both in design and manufacturing. Advantage is that if boundary conditions and objectives are set up correctly, no additional work has to be spent on dimensioning of the design	++	Novel application. Novel to use compliant structures as expansion chamber. Includes deformation under pneumatic loading, lift or wing root moment maximization and thin-walled design

Table B.2: Concept comparison for expansion chamber

Number		Mass	Efficiency		Reliability		Manufacturability		Complexity	Academic relevance	
A.FE.S1	-	Needs additional high voltage source and control. Valve itself will consist of set of rings/membranes and will not be heavy	o	Little power consumption	–	Electrostatic 'catching' and release is dependent on stiction, dynamic bouncing behaviour, surface tension if wet area. Fuel ejection is dependent on previous combustion pressure. Misfires lead to no droplets being ejected.	-	Construction can consist out of a stack of thin rings and membranes manufactured by lasercutting. Micrometer thin insulation layers have to deposited on membranes. Electrical contacts of valve bodies and membranes have to designed in a practical way	–	Complex, actuator design, electrical design, structural design, combustion pressures are all interrelated	++	Very novel, new type of valve actuation
A.FE.S5	+	Valve itself is very compact and made of thin sheet materiaal. Additional structure should between the bottom of the expansion chamber and the opening pin	++	No power consumption	+	Upon misfiring the piston body should have enough kinetic energy to touch pin. Compliant expansion chamber should be laterally stiff enough to prevent parasitic motions that compromise pin touching precision.	++	Valve itself can be easily made by a lasercutting. Pin structure is positioned outside expansion chamber and does not have strict stiffness requirements. Thus it can be made by 3D printing, lasercutting or conventional milling or lathing	+	Relatively simple, pretension of valve mechanism could be cumbersome as well as ensuring no parasitic oscillations for precise pin touching	+	Novel, not seen in conventional engines
A.FE.S7	+	Valve itself is compact and integrated within expansion chamber. Small additional structure is needed with greater diameter than bellow to fix ring	++	No power consumption	++	If designed correctly, valve opening is only dependent on piston position and bellow deformation. Metal-to-metal impacts and ring vibrations can be an issue	+	Ring can be made by lasercutting. Difficulty is attaching bellow end to thin ring by welding, adhesion or monolithic manufacturing like electrodeposition. A soft material for sealing and damping may be incorporated	+	Relatively difficult mechanical design. All stiffnesses should exactly match in order to function properly. Advantage is that it is passive and relatively independent on combustion cycle.	+	Novel, innovation is in the fact that valve opening is entirely dependent on state of deformation

Table B.3: Concept comparison for the exhaust valve

Number		Mass		Efficiency		Reliability		Manufacturability		Complexity		Academic relevance	
A.FD.S5	++	Compact thin-walled valve, no additional circuits	++	No power consumption	+	Misfires leads to improper fuel dosing. Stiction issues	++	Simple, could be manufactured out of single film with a laser cutter	++	Relatively simple, design requires balancing of elastic forces and combustion pressures	–	Widely used in engines, no innovation
A.FD.S8	-	Compact tube design, additional heating elements, very high battery requirements	–	Excessive power consumption for low evaporation time.	o	Combustion heat will gradually penetrate towards valve body, and will influence evaporation. However it has no moving parts, no stiction, vibration	o	Heat exhanger in the form of off-the-shelf tubes is relatively simple to manufacture	o	Relatively complex thermal design, very simple mechanical design. Electronic circuit and fast power control is needed	+	Relatively novel, not seen in conventional engines in this form
A.FD.S9	o	Compact tube design, additional high voltage electronic circuit	+	Very little power consumption	+	No mechanical concerns. Heat penetration from combustion chamber will lead to viscosity change that enhances fuel ejection	–	Requires electrical insulation of capillary tube, manufacturing converging nozzle, electric contacts, assembly of nozzle array	-	Complex. Modelling of viscous forces, pressure forces, electrowetting, capillary forces, ejection dynamics. Simple mechanical design	++	Very novel
A.FD.S13	o	Additional high voltage electronic circuit, compact valve design	-	Relatively high power consumption	++	Reliability proven in off-the-shelf inkjet heads	++	Very difficult when custom manufacturing, but printhead is taken off-the-shelf	+	Requires nozzle control	o	Novel in engine applications but not in printer industry
A.FD.S16	o	Additional high voltage electronic circuit, compact valve design,	o	Since electrostatic actuator does not deliver work but only 'holds' it requires relatively less power than other DOD concepts.	–	Misfires will lead to uncertainty in combustion pressures. Electrostatic catching and release is dependent on 'bouncing behaviour', damping and stiction which is difficult to predict.	–	Requires film designs with micrometer insulation layers. Valve should be floating in expansion chamber. Requires electric contacts on membranes and other electronic circuit	–	Although droplet ejection is same as in other state-of-the-art DOD designs, it is difficult to model. Electrostatic catching and release is a rather complex mechanism. Requires additional high voltage circuits.	++	Very novel
A.FD.S17	+	Pin and valve combination can be relatively small	+	No power consumption	o	Very little control possible in terms of fuel mass injected	o	Although pin and valve combination can be relively easy to manufacture, it requires additional active element to initiate startup.	-	Requires additional active element to initiate startup that should be integrated	o	Relatively novel application, but present in conventional valves (i.e. bicycle tire valve)

Table B.4: Concept comparison for the fuel delivery system

Number		Mass		Efficiency		Reliability		Manufacturability		Complexity		Academic relevance	
A.IG.S1	+	Lightweight heating element needed	–	Relatively high power consumption	+	Ignition temperature can be achieved in a controlled manner, although deposition of combustion products possible	o	Requires microfabrication steps like micro laser depletion or photo-lithography to creating heating element	-	Electronic circuit should deliver enough power, sufficient temperature control is needed, heat transfer between element and gas as well as scavenging should be examined	o	Relatively mature technology, although miniturization is not well-covered
A.IG.S7	+	Lightweight capacative circuit and spark electrodes possible	-	Moderate power consumption, lower than glow plug	+	Ignition temperature can be achieved in a controlled manner, although deposition of combustion products possible	o	Requires precise manufacturing and spacing of electrodes	-	Electronic circuit should deliver enough voltage, electrode design is required, scavenging should be examined	o	Relatively mature technology, although miniturization is not well-covered
A.IG.S8	o	No addition ignition mechanism, however increased pressure leads to heavier chamber parts	++	No power consumption	o	Ignition temperature should be reached. Premature combustion can be issue.	+	Does not require difficult manufacturing	o	Ignition temperature requirement imposes additional pressure and heat transfer requirements on chamber	+	Less covered in literature than active ignition. Miniturization is not well covered.
A.IG.S12	+	Lightweight catalyst element needed	++	No power consumption	++	Passive nature increases reliability	+	Does not require difficult manufacturing, although catalyst production method is not trivial	++	Only catalyst needed	++	Field is relatively unexplored, few existing chemical engines

Table B.5: Concept comparison for the ignition mechanism

B.4. TROUBLESHOOTING PROCEDURE OF INJECTION MODULE

B.4.1. FUNCTIONAL EXPERIMENT

To investigate the full transport functioning of the device, a first functional experiment was conducted to see if droplet motion could be initiated. A 7 nL droplet DI water with 3 g/L NaCl was placed on the first electrode of the substrate by a pipette. Subsequently, the electrodes were manually actuated one-by-one to investigate if droplet motion could be initiated. No droplet motion or contact angle change was observed. The droplet was displaced by a wooden skewer to see if other electrodes were functioning, but similar result was observed. Moreover, it was tried to ground the droplet using a separate grounding cable inserted into the droplet. Again, no contact angle change was observed. All aforementioned tests were carried out up until an actuation voltage of 300V, to eliminate the probability of dielectric film thickness being too large for significant contact angle change. Although dielectric breakdown is expected for this voltage, it was not observed.
It is important to mention that this first test involves testing multiple device functions at once, essential skipping singular component testing, which was done due to time limitations. The reasons why correct device functioning was not observed cannot be independently verified. Therefore, the following sections describe the subexperiments that were carried out to independently isolate potential failure causes.

B.4.2. VOLTAGE SUPPLY TEST

The first potential failure source could be a faulty voltage supply to the electrodes. Voltage-measurement of PCB contact pads indicated successful voltage supply on the PCB. Subsequently, it was investigated if the conductive film between the PCB and gold contact pads was actually making a conductive connection. A test-slide without dielectric and hydrophopic layer and continuous gold-coating was used to verify the conductive connection between the gold surface and each of the PCB contact pads. After clamping the PCB boards on the glass slide with continuous gold surface, resistance measurement concluded no conductive connection was present between the different PCB tabs. This indicates that the conductive film connection did not make proper contact. This could be caused due to the fact that the PCB clamping surface is slightly uneven since solder dots are sticking out above the PCB surface. Also, damages and cracks in the gold film could have broken the circuit. The gold film is highly fragile and is being removed upon scratching contact solid objects immediately. A micro relative sliding movement between the conductive adhesive and the gold film resulted in partial gold film damage, scratching lines and loose gold flakes already, indicating improper adhesion.
Electrode manufacturing using gold sputtering on glass and laser depletion is advantageous for manufacturing time as it has the ability to perform prototype iterations within days instead of weeks. However, the use of this method has detrimental robustness issues. This is especially true when combined with an conductive adhesive film for electrical connection. Glass adhesion and thereby gold-film robustness could be significantly improved by using pretreatment methods as plasma-cleaning or deposition of gradient bonding layers [29], which is strongly recommended for future prototypes. A suggestion for a more robust electrical connection is simply inserting the side of the glass slide in a DIMM connect or using wire bonding to make the electrical connection.

B.4.3. ITO GLASS TESTS

ITO GLASS TEST A

To eliminate the failures caused by gold film fragility, a prefabricated ITO coated glass was used in a subsequent design iteration. The electrode design was significantly simplified into rectangular electrode strips, visible in Figure 4.18.

The electrodes were patterned by the same fabrication method, however visual inspection of the insulation lines is difficult due to the transparent nature of the ITO coating. Resistance measurement indicated that no conductive connection was present between the neighbouring electrodes. The dielectric and hydrophobic layer was applied by the previously described method. The voltage supply cables were directly connected to the exposed contact pads, without an intermediate PCB board. The electrical connection was successfully tested by resistance measurement. Subsequently, a first test performed by depositing a 1 μL DI droplet with 3 g/L NaCl on the slide and manually actuating the electrodes one-by-one. However, no contact angle change or droplet movement was initiated. Secondly, all electrodes were actuated up until 130V and the droplet was grounded using a grounding wire. Now bubbles were observed in the droplet and the droplet evaporated with a significant rate. This observation likely indicates electrolysis of the conductive droplet, caused by a short-circuit between electrode and droplet, a phenomenon widely seen in EWOD prototypes [24]. The short

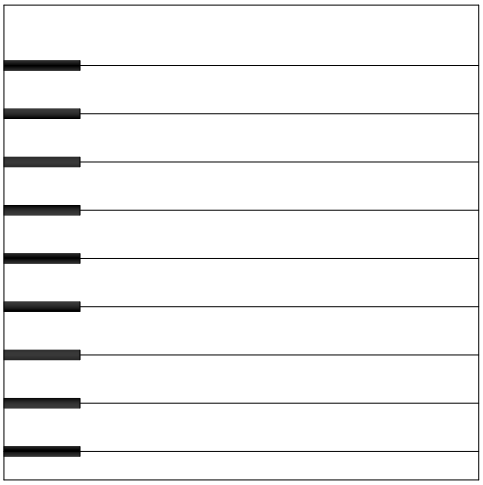

Figure B.5: Electrode pattern of ITO coated glass device

circuit could be caused by dielectric breakdown due to a thinner dielectric layer than the projected thickness of 0.7μm. This could be caused by a significant spatial variation of the dielectric film thickness, due to the relatively poor quality of the spincoating process. Although the electrodes were covered, it could clearly be seen that the slide was not fully covered by the SU-8 film. It is therefore unclear if the desired thickness was achieved at the electrode location. Thickness measurement is tried with an interferometer and microscope, however this was unsuccessful due to the transparent nature of SU-8 and Fluoropel. Another cause for the short-circuit is that other defects could be present in the dielectric film, created by contamination under the film, pinholes or ITO corrosion [82]. Contamination under the film was visually inspected with a microscope. Small particles can be observed, as is visualised in Figure B.6. It is expected that these flakes are generated by the laser-depletion process step. In the next experiment, the substrate will be cleaned more thoroughly with DI water and IPA.

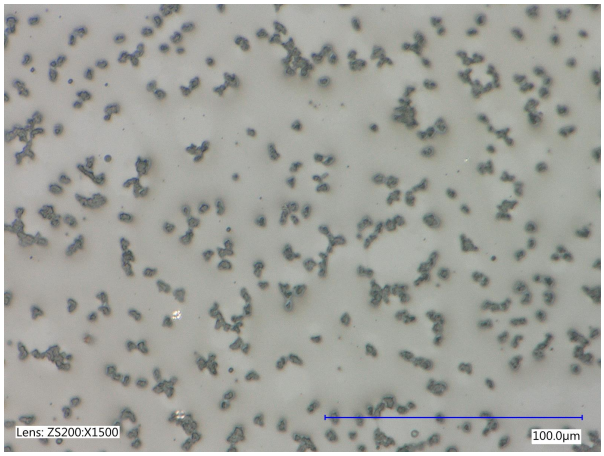

Figure B.6: Particles present in or under the dielectric layer

ITO GLASS TEST B

Another version was manufactured with identical electrode design, but now a higher volume was dispensed on the slide during the spincoating process, to increase the chance of achieving the estimated dielectric film thickness. Also, a lower voltage of 100V was applied in order to prevent potential dielectric breakdown in this case. The dielectric and hydrophobic layer were applied using identical steps as in the other versions. A 3 μL DI water droplet with 3 g/L NaCl was placed at the boundary between two electrodes. Again, no contact angle change or droplet initiation was observed up until a voltage of 100V. The droplet was grounded using a grounding wire, now a significant contact angle change was observed of $\Delta\theta$ of 40 °at 100V and no electrolysis bubbles. The reason that grounding the droplet leads to a contact angle change in contrast to normal-single

plate actuation, is that the voltage drop across the dielectric layer is a factor of two higher [13].

If the droplet was moved across a fully actuated electrode pattern by moving the grounding wire, a varying contact angle was observed. Since voltage drop across the dielectric layer was held constant, it can be discussed that there is a significant spatial variation in the dielectric coating thickness. This could be caused by the masking method of the Kapton tape, that could leave a quadratic thickness profile during the spincoating procedure.
The contact angle change was varying strongly during several subsequent electrode actuation cycles and eventually, no significant contact angle change was observed anymore.
Sliding manipulations of the droplet by the grounding wire over the locations where a droplet was placed before, where a significant contact angle change was observed initially, the droplet appeared to be sticking after letting it slide over this location. Also, tiny surface defects were observed at these sticking locations, as depicted in Figure B.7.

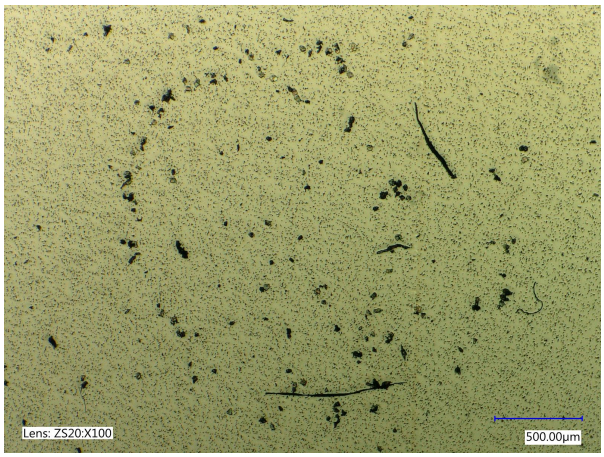

Figure B.7: Damages present in the hydrophobic or dielectric layer

It could be discussed that the hydrophobic layer was locally damaged, exposing the more hydrophilic material underneath, where the droplets effectively attracts to. An obvious cause for this would be dielectric breakdown, however the expected thickness and voltage suggests otherwise and also no electrolysis was observed. It should still be noted that dielectric breakdown is probable.
The apparent hydrophobic layer defects may also be a result of charge trapping. Charge trapping is a problem in fluoropolymer layers previously encountered in literature, which degrades the electrical response of the fluoropolymer films [6, 72]. When a voltage is applied across the drop surface, charges accumulate at the liquid-solid interface. As the voltage is removed, the charges should dissipate and the droplet should spring back to its original shape. However, it is possible that the charges become essentially trapped in the fluoropolymer layer [6]. It is posed that charge trapping occurs when the electric field intensity exceeds the dielectric strength of the fluoropolymer layer, without essentially causing dielectric breakdown of the full composite dielectric layer [6]. Electrolysis was not observed in this test, so full dielectric breakdown is unlikely The charge trapping voltage V_{ct} can be described by Equation B.1 [6]

$$V_{ct} = D_{fp}(t_{fp} + t_{SU8}\frac{\epsilon_{fp}}{\epsilon_{SU8}}) \tag{B.1}$$

where $D_{fp}, t_{fp}, t_{SU8}, \epsilon_{fp}, \epsilon_{SU8}$ is the dielectric strength of the Fluoropel, Fluoropel thickness, SU-8 thickness, dielectric constant of FLuoropel and dielectric constant of SU-8 respectively. Evaluation of Equation B.1 leads to a V_{ct} of 72V. Therefore, it can be posed that charge trapping is likely to occur at the actuated voltage of 100V if dielectric layer had the estimated thickness, damaging the hydrophobic surface and causing the sticking behaviour. Other defects could be still present in the dielectric film, created by dust particles, pinholes or ITO corrosion [82]. Due to the available time left for the research project, it was chosen not to further proceed with the EWOD concept development.

C

APPENDIX C

C.1. BONDING METHOD SELECTION

The following bonding methods were considered for the connection between the bottom bellow-endplate and exhaust spring as well as the connection between the top bellow-endplate and the output mass shaft. Note that to prevent squeezing the adhesive or bonding material out of the bonding area, a spacing distance was considered in some bonding methods.

1. ISOTIP 7459 solder paste (98% tin, 2% silver), bonding areas not separated
2. ISOTIP 7459 solder paste (98% tin, 2% silver), bonding areas separated by 0.1 mm
3. Toray EF8020 adhesive film, bonding areas separated by 0.1 mm
4. Toray EF8020 adhesive film, bonding areas separated by 0.2 mm
5. Toray EF8020 adhesive film, bonding areas separated by 0.3 mm

The different bonding methods were applied at the end (10mm x 10mm) surface of a retangular (10mm x 70 mm x 0.15 mm) stainless steel strip. To create the separation distance, a square-ring (depicted on the right of Figure C.1 was positioned on the bonding area. Another rectangular strip with identical dimensions was pressed onto the bonding area in the jig displayed in Figure C.1. The solder paste was thermally cured for 10 minutes at 240 degrees Celcius in an oven. The adhesive film was thermally cured for 30 minutes at 120 degrees Celcius in an oven. Subsequently, the specimen were tensile tested by clamping strip ends in a universal testing machine and measuring force as a function of deflection until failure.

The force-deflection of the different specimen are depicted in Figure C.2. The specimen that failed with a breakage force over 1000 N, it was the stainless strip that failed in contrast to the adhesive film. Figure C.3 depicts the minimum shear strength of the different bonding methods. It is chosen to implement the Toray EF8020 adhesive film with a 0.1mm separation distance in in the belllow connections.

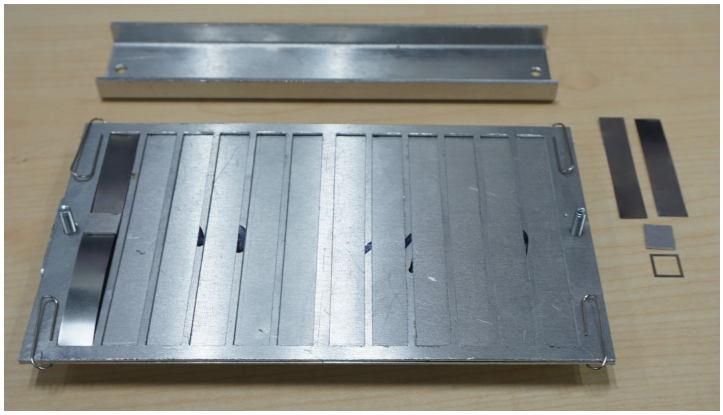

Figure C.1: Bonding jig, including the square-ring spacer on the right and pressing squares.

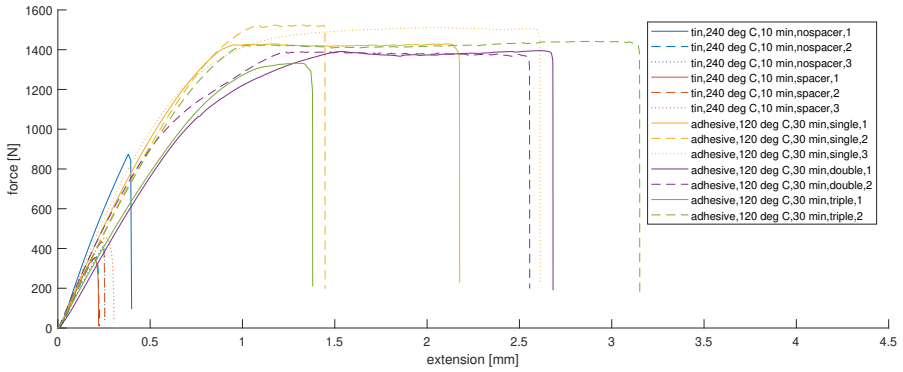

Figure C.2: Force deflection curves of the different specimen

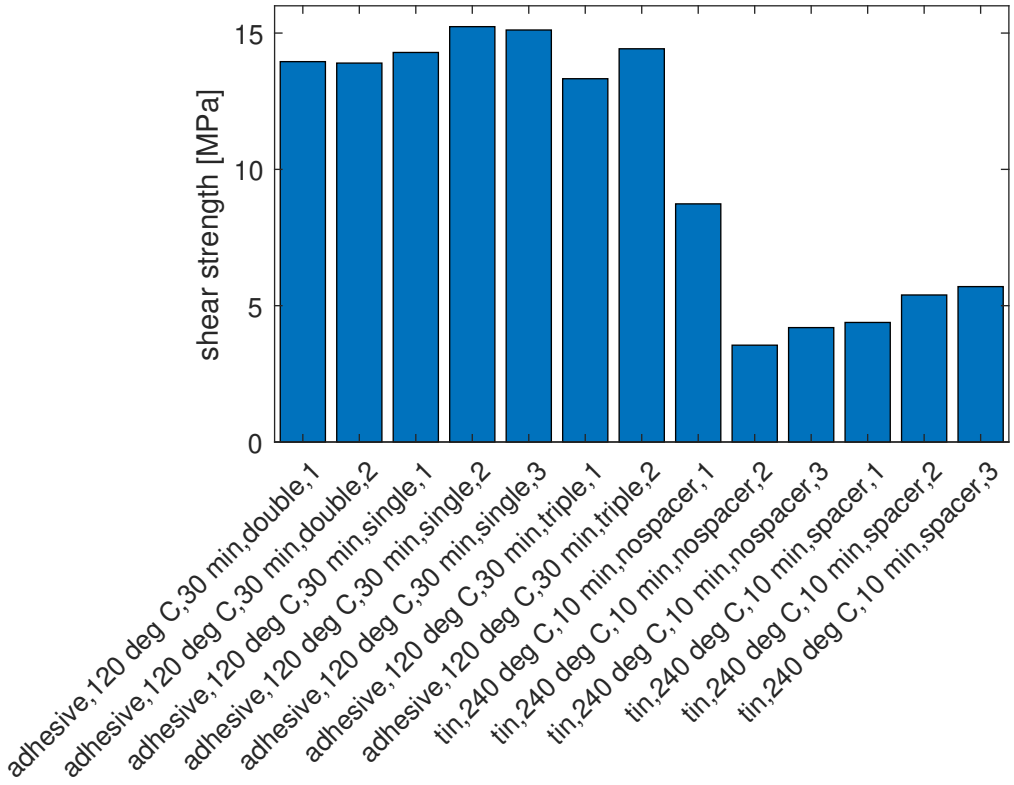

Figure C.3: Shear strength of different bonding methods